AP-2α and AP-2β cooperatively orchestrate homeobox gene expression during branchial arch patterning

Eric Van Otterloo[1], Hong Li[1], Kenneth L Jones[2], Trevor Williams[1,3,4]

[1] Department of Craniofacial Biology, University of Colorado Anschutz Medical Campus, Aurora, CO, 80045, USA

[2] Department of Pediatrics, Section of Hematology, Oncology, and Bone Marrow Transplant, University of Colorado School of Medicine, Aurora, Colorado 80045 USA

[3] Department of Cell and Developmental Biology, University of Colorado Anschutz Medical Campus, Aurora, CO, 80045, USA

[4] Department of Pediatrics, University of Colorado Anschutz Medical Campus, Children's Hospital Colorado, Aurora, CO 80045, USA

Keywords: *TFAP2*, AP-2, neural crest, mandible, maxilla, homeobox, pharyngeal arch, branchial arch, *DLX*

SUMMARY STATEMENT: The AP-2 transcription factors, AP-2α and AP-2ß, have a cooperative and specific role in regulating homeobox gene expression during development of the mouse jaw.

ABSTRACT:

The evolution of a hinged moveable jaw with variable morphology is considered a major factor behind the successful expansion of the vertebrates. *DLX* homeobox transcription factors are critical to establish the positional code that patterns the mandible, maxilla and intervening hinge domain, but how these genes are regulated remains unclear. Herein, we demonstrate that the concerted action of the AP-2α and AP-2β transcription factors within the mouse neural crest is essential for jaw patterning. In the absence of these two genes the hinge domain is lost and there are alterations in the size and patterning of the jaws correlating with dysregulation of homeobox gene expression, with reduced levels of *Emx*, *Msx* and *Dlx* paralogs accompanied by an expansion of *Six1.* Moreover, detailed analysis of morphological features and gene expression changes indicate significant overlap with various compound *Dlx* mutants. Together, these findings reveal that the AP-2 genes have a major function in mammalian neural crest development, influencing patterning of the craniofacial skeleton via the DLX-code, a result that has implications for vertebrate facial evolution as well as for human craniofacial disorders.

INTRODUCTION:

Development of the facial complex in mammals begins as an outgrowth of structural protrusions, the facial prominences, surrounding the nascent oral cavity. These outgrowths include a separate pair of mandibular (MdP) and maxillary (MxP) prominences constituting the first branchial arch (BA1) with a single frontonasal prominence (FNP) superior to these structures (see **Fig. S1**) (Trainor, 2014). The mesenchyme of these prominences is largely composed of neural crest cells (NCCs), which migrate from the dorsal mid/hindbrain and are involved in outgrowth and morphogenesis associated with facial development (Trainor, 2014). Signaling from the adjacent ectoderm, endoderm, and neural tube are key sources of positional identity for the invading NCCs, for example regulating the establishment of dorsal-ventral identity within BA1 (Trainor, 2014). For BA1, this ultimately leads to formation of both maxillary (upper-jaw) and mandibular (lower-jaw) units, with distal cap regions and a hinge domain at the articulation point of the MdP and MxP typifying the bauplan of the vertebrate jaw (Fish et al., 2011) (see **Fig. S1B-E**). Notably, modulation of these signals, or the ability of NCCs to respond to them, can ultimately influence final adult structures emerging from this bauplan. Such plasticity is critical for the array of facial features observed amongst vertebrate species but also provides an opportunity for disruption in a variety of craniofacial disorders.

Numerous studies have shown that homeobox transcription factors (TFs) are key players in the regulation of BA1 patterning. Specifically, nested expression of the *DLX* family of homeobox TF's (*DLX1-6*), is critical to establish axes essential for craniofacial patterning within the jaws (**Fig. S1F, G**) (Cobourne and Sharpe, 2003). Additional homeobox TF's, including *Msx*-family members (Alappat et al., 2003), *Alx*-family members (McGonnell et al., 2011), *Six1* (Tavares et al., 2017), *Emx2* (Compagnucci et al., 2013), *Gsc* (Rivera-Perez et al., 1995; Yamada et al., 1995), and *Barx1* (Barlow et al., 1999; Sperber and Dawid, 2008), have been implicated in associated aspects of BA1 patterning. Thus, a craniofacial gene regulatory network (GRN) is emerging for BA1 composed of numerous homeobox TFs driving NCC

patterning. However, the upstream regulators of homeobox TF expression are less well understood, and are likely key to priming cranial NCCs for the cues they will encounter while invading BA1. Identifying these regulators would provide additional details into autonomous nodes that can be used to influence craniofacial form during normal and abnormal development.

One gene family postulated to be critical throughout NCC development are the AP-2 TFs consisting of five paralogs in mammals: *Tfap2a-e*, encoding the proteins AP-2α – AP-2ε, respectively (Eckert et al., 2005; Green et al., 2015; Simoes-Costa and Bronner, 2015). These proteins all recognize a similar consensus sequence (Eckert et al., 2005) raising the possibility of functional redundancy in regulating target gene expression when multiple family members are expressed simultaneously (Bassett et al., 2012; Hoffman et al., 2007; Knight et al., 2005; Li and Cornell, 2007; Schmidt et al., 2011; Seberg et al., 2017; Van Otterloo et al., 2010; Wang et al., 2008). The potential for coordinated action is particularly pertinent to the early NCCs, where both *Tfap2a* and *Tfap2b* are highly expressed (**Fig. S2A-E**) (Eckert et al., 2005). Currently, *Tfap2a* is the best characterized with respect to NCC development in multiple model organisms (Brewer et al., 2004; Brewer et al., 2002; de Croze et al., 2011; Knight et al., 2003; Luo et al., 2003; O'Brien et al., 2004; Schorle et al., 1996; Shen et al., 1997; Zhang et al., 1996). However, NCC roles for additional paralogs, notably AP-2ß (*Tfap2b*), have also been identified in mouse and non-mammalian species (Knight et al., 2005; Martino et al., 2016; Schmidt et al., 2011; Simoes-Costa and Bronner, 2016). Further evidence suggesting critical roles for AP-2α and AP-2ß in NCCs has been obtained from the analysis of human Branchio-Oculo-Facial (Milunsky et al., 2008) and Char Syndromes (Satoda et al., 2000), respectively, that display defects in NCC derivatives in the face, heart and skin. Finally, NCC enhancers mapped in human and chimp contain an over-representation of AP-2 binding sites and such sites correlate with active histone modifications and elevated gene expression (Rada-Iglesias et al., 2012). Together, these findings raise the possibility that the AP-2 genes have been integral to the evolution of the NC and that modulation of AP-2 regulatory circuits has potentially influenced species-specific

craniofacial traits during evolution (Prescott et al., 2015). Despite strong evidence that AP-2 is critical within the hierarchy of NCC development, single mouse NCC-specific gene knockouts for *Tfap2a* and *Tfap2b* – the most pertinent members expressed in early NCCs – produce only partially penetrant (~44%) cleft secondary palate or eye defects, respectively (Brewer et al., 2004; Martino et al., 2016) – with some animals remaining viable into adulthood. To address this discrepancy, we generated mice lacking both *Tfap2a* and *Tfap2b* within the NCCs. Our results reveal that these two AP-2 TFs act in concert within NCCs in a cell autonomous manner to regulate major aspects of craniofacial development. These data resolve the paradox of the mild phenotypes seen with single conditional mutants, demonstrate the importance of AP-2 in the cranial BA1 NCC GRN, and provide an important framework for analysis of vertebrate evolution and human craniofacial birth defects.

RESULTS:

NCC specific deletion of *Tfap2a* and *Tfap2b* results in exacerbated craniofacial defects

Although three of the five mouse *Tfap2* genes, *Tfap2a*, *Tfap2b* and *Tfap2c*, are expressed at appreciable levels in the cranial NCC, only mRNAs from *Tfap2a* (encoding AP-2α) and *Tfap2b* (encoding AP-2ß) are found at high levels at E8.5 and E9.5 when the NC is emerging from the margins of the neural tube and migrating to the facial prominences (**Fig. S2A-E**). Surprisingly, previous NCC-specific deletion of either AP-2α or AP-2ß alone resulted in relatively limited craniofacial defects (Brewer et al., 2004; Martino et al., 2016), and therefore we considered that they might be functionally redundant. To address this issue, we generated *Tfap2a*/*Tfap2b*-NCC specific conditional double mutants using a new *Tfap2b*-conditional allele (**Fig. S3A-C**), in conjunction with the *Tfap2a*-floxed allele (Brewer et al., 2004). Next, we bred mice heterozygous for *Tfap2a*- (Zhang et al., 1996) and *Tfap2b*-null (**Fig. S3D**) alleles that also contained the *Wnt1:CRE* transgene (Danielian et al., 1998) to mice homozygous for both conditional alleles, to target *Tfap2a*/*Tfap2b* in pre-migratory NCC's. The expected offspring from

these matings included the desired double conditional mutants, *Wnt1:CRE; Tfap2*$^{null/flox}$*; Tfap2b*$^{null/flox}$, that we term DCMs for the remainder of this study. In addition, other allelic combinations were generated with different *Tfap2a* and *Tfap2b* gene dosages (**Table S1A**). These included mice that have lost both *Tfap2a* alleles in the NCC, but retain one functional allele of *Tfap2b* (single conditional mutant AP-2α; abbreviated SCM-A), or those missing both *Tfap2b* alleles, but possessing one functional copy of *Tfap2a* (single conditional mutant AP-2β: abbreviated SCM-B). The availability of the DCM, SCM-A, SCM-B and double-conditional heterozygous (DCH) mice enabled us to compare how various *Tfap2a*/*Tfap2b* allelic combinations impacted development. Western blot analysis revealed, that compared to controls, SCM-A and SCM-B embryos showed a modest reduction in AP-2 protein levels whereas DCMs displayed a complete loss in the presence of a CRE recombinase transgene, allowing genetic dissection of their redundant function in the NC **(Fig S2F, G**).

We next addressed the developmental consequences of NCC-specific deletion of *Tfap2a* and *Tfap2b* on gross craniofacial development by examining embryos at E18.5 (**Fig. 1A-H**). Three phenotypic classes were identified, each corresponding to particular genotypes: 1) embryos with relatively normal craniofacial structures that were either control, DCH, or SCM-B's (**Fig. 1A, B, E, F,** and not shown); 2) embryos with a slightly malformed nasal-bridge, slight micrognathia, and a cleft secondary palate that were SCM-A's (**Fig. 1C, D**); and 3) embryos with a complete midface cleft, shortened and cleft mandible, low set ears with microtia, microglossia, and a cleft secondary palate that were DCM's (**Fig. 1G, H**). Note that in SCM-A's, the cleft secondary palate was 100% penetrant, in contrast to the limited penetrance (44%) of this phenotype in *Tfap2a-Wnt1:CRE* mutants (Brewer et al., 2004). Also, a small portion (~22%) of SCM-B's developed cleft secondary palate (**Table S1A**), a feature not yet observed in *Tfap2b-Wnt1:CRE* mutants (Martino et al., 2016). The increased incidence of clefting in SCM-A and SCM-B strains compared with the corresponding single knockouts presumably reflects the

detrimental consequence from loss of one additional *Tfap2* allele. Collectively, several conclusions can be derived from the analysis of gross morphology. First, AP-2α and AP-2ß cooperatively regulate craniofacial development cell autonomously in NCC's. Second, AP-2α may play a more prominent role than AP-2ß in this process. Third, there is a phenotypic spectrum, dependent on the number of functional *Tfap2a/Tfap2b* alleles present in the NCC – implying dosage sensitivity to AP-2 levels during craniofacial development.

***Tfap2a* and *Tfap2b* are largely dispensable for early NCC development.**

Given the cell autonomous role for AP-2α and AP-2β within cranial NCC's, and the emphasis placed on AP-2α as a 'master regulator' of NCCs (Green et al., 2015; Hong et al., 2014; Rada-Iglesias et al., 2012; Rada-Iglesias et al., 2013; Simoes-Costa and Bronner, 2015; Trainor, 2014), we next examined NCC developmental progression in SCM-A's, SCM-B's, and DCM's, as compared to controls. To assess initial specification, emigration, and migration of NCC's into the craniofacial complex, we conducted the genetic cross described above but also included the Rosa26 reporter allele in the breeding scheme (Soriano, 1999). In conjunction with the *Wnt1*:CRE transgene (Danielian et al., 1998), this reporter allele allows precise, indelible labeling of NCC's, detected by ß-galactosidase (ß-gal) staining. At E9.0 streams of migratory ß-gal+ NCC's were clearly identifiable in both the first and second BA of control embryos with no obvious differences noted in either SCM or DCM embryos (**Fig. S4A, B** and data not shown). However, by E10.0-E10.5, although similar labeling patterns were detected between controls (**Fig. 2A, Fig. S4C**) SCM-A's (**Fig. 2B**), SCM-B's (**Fig. 2C**), and DCM's (**Fig. 2D, Fig. S4D**), differences in the size of the BAs were becoming apparent in SCM-A's and DCM's (**Fig. 2B' and D', Fig. S4C, D** and not shown). We then examined whether differences in cell proliferation and/or cell death could account for the observed morphological changes in the DCMs using α-phospho-Histone H3 (pH3) and α-cleaved caspase 3 (CC3) immunofluorescence, respectively. Grossly, cell proliferation was not dramatically altered in mutant versus control embryos at

E10.5 in BA1 (**Fig. S4E, F**), nor within the anterior dorsal neural tube at E8.5 (data not shown). However, analyses of cell death in adjacent sections identified localized groups of cells that were CC3+ in DCM embryos. Such cells were largely observed around the intersecting hinge domain of the developing upper- and lower-jaw in DCM embryos (**Fig. 2E, F**) consistent with the observed BA1 hypoplasia. These latter findings indicate that AP-2α/ß are critical for preventing the death of a small subset of BA1 NCCs, but do not appear to have a global role in NCC survival.

We next examined specification and differentiation of cranial NCC-derivatives, including the peripheral nervous system (PNS), odontoblasts, bone and cartilage. With respect to the PNS, we employed anti-neurofilament immunostaining (Dodd et al., 1988) at E10.5 to visualize the cranial ganglia and associated cranial nerves. These studies demonstrated that the gross development of the cranial ganglia, including the trigeminal ganglia that are partially derived from the cranial NC (Begbie and Graham, 2001; Hamburger, 1961), occurred similarly in DCM's as compared to controls (**Fig. 2G, H**). Although we did note subtle alterations in the distal nerve projections at E10.5 and slightly hypoplastic trigeminal ganglion by E17.5 (**Fig. S4G, H**) – we postulate that these differences were secondary to morphological changes in the face of DCM embryos. Furthermore, comparative H&E analysis of the mandible at E17.5 revealed that DCMs and their wild-type counterparts were similar in the histological appearance of various NC-derived skeletal elements including the lower incisor (**Fig. 2I, J**,), the dentary bone and Meckel's cartilage (**Fig. 2K, L**).

In sum, the cranial NCC properties of specification, migration, proliferation, and differentiation were relatively normal in the absence of AP-2α and AP-2β except for a limited increase in apoptosis of post-migratory NC within the hinge domain. Except for this small domain of apoptosis, our studies nonetheless reveal that cranial NCCs from DCM mutants can differentiate into major derivatives including cranial ganglia, odontoblasts, bone, and cartilage. The finding that many facets of NCC biology can still occur in DCMs is surprising considering

the substantial role AP-2 paralogs play in NCC specification in non-mammalian species (de Croze et al., 2011; Hoffman et al., 2007; Hong et al., 2014; Li and Cornell, 2007; Luo et al., 2003). Nevertheless, craniofacial development is severely disrupted in the DCMs (**Fig. 1**), suggesting that the critical function of these AP-2 TFs is to cooperatively control GRNs within the NCCs involved in morphogenesis, growth and patterning of craniofacial structures.

RNA expression profiling identifies a critical role for AP-2 in regulating homeobox gene expression.

Previous studies have derived a series of interconnected GRNs that are necessary for the appropriate formation and patterning of the vertebrate mandible (Chai and Maxson, 2006; Clouthier et al., 2010; Parada and Chai, 2015). Therefore, given the cleft and hypoplastic mandible, we focused our remaining studies on how the combined function of AP-2α and AP-2β impacted the GRNs required for development of this BA1 derivative. Specifically, we conducted RNA profiling (RNA-seq) of the MdP in control versus DCM embryos at E10.5, a period when significant patterning is occurring and morphological changes are becoming more apparent in DCM embryos (see **Fig. 2D**). Triplicate biological replicates of individual MdPs were isolated from 3 control and 3 DCM embryos (**Fig. 3A**). Following sequencing, two separate bioinformatic pipelines were implemented to identify differentially expressed genes (**Fig. S5**). The utilization of two pipelines was employed to reduce false-positives and false-negatives inherent to different bioinformatic approaches (Fonseca et al., 2014). These analyses resulted in either 279 (Class I) or 673 (Class II) genes showing 1.25 fold or greater differential expression between control and DCM MdP samples (**Fig. 3B, Table S2**). Overlapping these two datasets identified 182 'high-confidence' differentially expressed genes (Class III; 89 down, 93 up) in DCMs compared to controls (**Fig 3C, Fig. S6, and Table S2**), and this smaller dataset showed the most robust correlation coefficient between fold-change values compared with the individual pipelines (**Fig. S5**).

We next used these gene lists to perform several bioinformatic analyses to assess the types of genes enriched and their relationship to known AP-2 targets and GRNs. First, we used both functional annotation clustering (FAC) (Huang da et al., 2009a, b) as well as gene set enrichment analyses (GSEA) (Mootha et al., 2003; Subramanian et al., 2005) to initiate a systems level analysis and extract over-represented molecular pathways from our datasets of altered gene expression. Utilizing the 182 Class III gene set, FAC identified the number one and two overrepresented clusters to contain the terms '*homeobox transcription factors'* (**Fig. 3D**, cluster 1) and *'transcription'* (**Fig. 3D,** cluster 2), respectively. These two terms were also highly enriched when the analysis was run using the larger Class I and II genesets (**Fig. 3D**), and were also significantly enriched in all three gene-sets using an alternative clustering software package [Enrichr (Chen et al., 2013; Kuleshov et al., 2016), data not shown]. Interestingly, all six *Dlx* genes – central to BA1 patterning – were present in the Class III gene-set and all six were down-regulated in the DCMs (**Fig. 3C, Fig. S6, Table S2**). Notably, *Dlx* genes occur as bigene clusters in the mouse genome and these loci also produce opposite strand transcripts from *Dlx1*, *Dlx4*, and *Dlx6*. These *Dlx1as*, *Dlx4os*, and *Dlx6os1* transcripts were also represented in the Class III dataset and down-regulated similarly to their adjacent *Dlx* genes. Therefore, of all the genes that were expressed at a significantly lower level in the DCMs, 10% mapped to the three *Dlx* gene clusters. Also in relation to the DLX-GRN, we observed modulation of genes associated with the activity of the homeobox TF *Six1*, which is notable since SIX1 has recently been shown to antagonize *Dlx* expression and regulate development of the intermediate 'hinge' region (Tavares et al., 2017). Thus, in Class III gene-sets from the DCMs we recorded increased expression of *Six1*, its partner *Eya1*, and potential cofactors *Sox2*, and *Tlx1*, but reduction in levels of *Aes*, a co-factor that can act to repress SIX1 function (Ahmed et al., 2012; Bajoghli et al., 2005; Riddiford and Schlosser, 2016) (**Fig. S6** and **Table S2**).

Next, using the entire gene expression dataset, we implemented GSEA with a variety of defined 'gene-sets' (**Table S3**) – based on *a priori* inferences about our dataset – along with a Q-value ranked list of most altered genes in DCM's versus controls. Supporting FAC analysis, homeobox TFs were again found to be significantly enriched within our most altered transcripts (**Fig. 3E**, Homeobox TFs). In addition, utilizing a previously published microarray of altered gene expression in the MdP of *Dlx5*$^{-/-}$ *Dlx6*$^{-/-}$ double-mutants (Jeong et al., 2008), we found significant enrichment of a similar set of genes to that discovered in DCM's vs controls (**Fig. 3E**, *Dlx5*$^{-/-}$/*6*$^{-/-}$). Importantly, no such enrichment was observed with randomly generated gene-sets, including ones based on known expression in BA1 (**Fig. 3E**, Random). Thus, both FAC and GSEA identified misregulation of key homeobox TFs, especially *Dlx*-family members, within the MdP of DCM embryos – placing AP-2α and AP-2ß at a key node within the GRN patterning BA1 NCCs.

We further examined the intersection of AP-2 protein binding, enhancer activity, and NCC specification by using our list of genes misregulated in the DCM mandible to mine recently published datasets relating to NCC chromatin and transcriptional signatures. First, we examined information on chromatin accessibility in migrating mouse NCCs (Minoux et al., 2017) and determined that *cis*-regulatory elements for the majority of the 182 genes we had identified were marked with either active (H3K4me2) or poised (H3K4me2/H3K27me3) chromatin marks in E10.5 mandibular NCC populations (**Fig. 3F**). Second, we analyzed a dataset derived from human induced NCCs (Rada-Iglesias et al., 2012) that examined the overlap between enhancer chromatin marks and the presence of AP-2 binding sites. Here, again, we found that a majority (~78%, 142 of 182 genes) of the gene-list we had generated had an associated AP-2 binding peak, with a large subset (~77%, 110 of 142 peaks) of these found within active or poised enhancer marks (**Fig. 3G**). Two additional transcriptional regulators, NR2F1 and NR2F2, that co-occupied a subset of these human NCC enhancers with AP-2α (Rada-Iglesias et al., 2012), were also significantly down-regulated in our 182 gene-set. Since previous studies have

demonstrated that knockdown of *Nr2f1* in NCCs decreases both TFAP2A and NR2F2 levels, (Rada-Iglesias et al., 2012) these findings suggest that the AP-2 and NR2F protein families may act in a regulatory circuit to mark active NCC enhancers. Taken together, examination of the gene expression differences between control and DCM mouse mandibles, in combination with mining of relevant enhancer datasets, reinforces the contention that the AP-2 TFs form a critical aspect of the GRN required for cranial NCC development.

Tfap2a/*Tfap2b*-*Wnt1*:CRE gene expression alterations reflect disruption of a DLX regulatory network

We extended the gene expression analysis by conducting whole-mount *in situ* hybridization on control and DCM embryos focusing on both down-regulated (*Dlx1*, *Dlx3*, *Dlx6*, *Emx2*, *Hand1*) and up-regulated (*Six1*, *Fgf8*) genes, many of which are part of a positional GRN that patterns the jaws. First, examining the 'DLX-code', we assessed expression of one paralog from each *cis* first-order linked pair (*Dlx1/2*, *Dlx3/4*, and *Dlx5/6*). These bi-genic *Dlx* clusters are normally expressed in a nested fashion in the E10.5 mesenchyme (**Fig. 4A, E, I and Fig. S1F, G**). *Dlx1* expression is found throughout the paired jaws as well as where they intersect at the hinge region (**Fig. 4A, C**). *Dlx6* expression is restricted to the hinge region and the MdP (**Fig. 4E, G**). Finally, *Dlx3* expression is even more restricted to aboral regions of the distal-portion of the MdP (**Fig. 4I, K**). In contrast, at E10.5 in DCM's, *Dlx1* expression was significantly reduced throughout both the MdP and MxP, including the hinge domain (**Fig. 4B, D**). *Dlx6* expression in DCM's was also drastically reduced throughout most of the MdP and the adjacent hinge-region, although limited expression was detected at more distal locations (**Fig. 4F, H**). Finally, *Dlx3* – a target of DLX5/6 activity –- was also reduced, with expression nearly absent throughout the MdP (**Fig. 4J, L**). Note that regions of *Dlx* expression in BA2 mesenchyme, or for *Dlx3* in the BA1 ectodermal domain, were less affected. Consistent with alteration to the DLX-code in the NCC-component of BA1, as well as the agreement between the GSEA profiles of DCM and

Dlx5$^{-/-}$*Dlx6*$^{-/-}$ datasets, additional downstream targets of DLX-activity (Depew et al., 2002; Jeong et al., 2008) were reduced in the MdP of DCM's as compared to controls [e.g. *Alx3*, *Alx4*, *Cited1*, *Col8a2*, *Dlx4*, *Gbx2*, *Hand1*, and *Hand2,* see **Table S2** and (Jeong et al., 2008)]. For example, *Hand1*, expressed at the distal midline of the converging MdPs in controls at E9.5 and E10.5 (**Fig. 4M, O**), lacked this expression domain completely in DCMs (**Fig. 4N, P**). Moreover, expression of the homeobox TF *Emx2*, which was specifically detected in the hinge region in controls (**Fig. 4Q**), was abolished in the DCMs (**Fig. 4R**) while expression within the telencephalon and in BA2 remained relatively intact. In contrast to the loss of *Emx2* signal and the down-regulation of *Dlx* transcripts, the expression of *Six1* expanded in the DCMs throughout BA1 including the hinge domain (compare control in **Fig. 4S to panel 4T**). In addition, *Fgf8*, a signaling molecule normally expressed in more oral regions of the MdP (**Fig. 4U**) was expanded aborally in DCM's (**Fig. 4V**), again indicating significant changes in the GRN underlying jaw patterning.

Next, to address whether these gene expression changes also occurred earlier during NCC migration into BA1, we conducted quantitative real-time PCR (qRT-PCR) on E9.5 BA1 RNA of control and DCM embryos (**Fig. 4W**). These experiments revealed that although some genes (e.g. *Rspo2*) that showed altered expression in E10.5 DCMs were unchanged compared to controls at E9.5, other critical regulators including *Six1 and Dlx*-family members were still significantly up-regulated or down-regulated, respectively at this earlier timepoint (**Fig. 4W**). Note that these early changes in the BA1 GRN presage the increase in cell death noted in the DCM hinge region at E10.5 that correlates with the loss of the *Emx2* expression domain. In summary, RNA-seq, *in situ* hybridization, and qRT-PCR, all highlight an important function of AP-2α/ß-activity in regulating expression of multiple genes that provide positional information to the developing jaws. Importantly, this patterning role for AP-2α/ß is likely operational at the initial stages of establishing the proximodistal axis.

***Tfap2a*/*Tfap2b*-*Wnt1*:CRE and *Dlx* loss-of-function mutant skeletons exhibit comparable phenotypic defects**

We next performed a detailed analysis of the *Tfap2a/Tfap2b-Wnt1*:CRE skeletons. The mammalian cranial skeleton has viscero/splanchnocranial, neurocranial, and chondrocranial components. While the former, comprising the bones of the facial skeleton are NCC-derived, the neurocranial and chondrocranial components are derived from both NCC (largely anterior) and mesoderm (largely posterior) (Couly et al., 1993; Gross and Hanken, 2008; Jiang et al., 2002; Le Douarin and Kalcheim, 1999; McBratney-Owen et al., 2008). Gross examination of E18.5 skeletons revealed that, as with the external morphology, mutant phenotypes ranged from mild in SCM-B, intermediate in SCM-A, to severe in DCMs (**Figs 5 and S7**). SCM-B skeletons (**Fig S7**) were largely indistinguishable from controls (**Fig 5A, D**), whereas SCM-A embryos had noticeable shortening of the premaxilla and mandible, as well as defects in the palatine bones consistent with cleft palate (**Fig. 5B, E**). DCM embryos had major defects throughout the NCC-derived skeleton, including the mandible, maxilla, and premaxilla (**Fig. 5C, F**). In contrast, more posterior, mesoderm-derived elements in the skull, such as the basioccipital and exoccipital bones, developed normally in all mutant embryos (**Fig. 5A-F**). Overall, these observations are consistent with a redundant and cell-autonomous role for AP-2α/AP-2ß in craniofacial skeletal development from the NC.

Strikingly, the analysis of the SCM-A and DCM craniofacial skeletons (**Fig. 5, 6**) also revealed remarkable similarity to defects previously reported in mice with certain *Dlx* mutant combinations (Depew et al., 2005). We describe the most notable phenotypic overlaps below, concentrating on the SCM-A and DCM animals, and summarize our comprehensive findings in Supplementary Figure 8. We first examined the upper- and lower-jaw in greater detail, including the maxilla and mandible, as well as bones of the zygomatic arch (ZGA), which are partly

derived from BA1 regions associated with the hinge domain (**Fig. 5G-Q, Table S1B**). In general, *Dlx1/2* have important functions with respect to the upper-jaw/ZGA, *Dlx5/6* are more critical for lower-jaw development, whereas loss of unlinked *Dlx* paralogs (e.g. *Dlx2* and *Dlx5*) affect structures at the intersection of the upper- and lower-jaw (Depew et al., 2005; Jeong et al., 2008). The ZGA normally consists of the zygomatic process of the maxilla, the jugal, and the zygomatic process of the squamosal (**Fig 5G**). The latter process was often absent in SCM-A skeletons (asterisk in **Fig. 5H, K**) while DCM embryos had loss or transformation of the squamosal and jugal as well as a highly truncated, thickened zygomatic process of the maxilla (**Fig. 5I, L**). With respect to the lower-jaw, the most severe defects were observed in the proximal domain (**Fig. 5M-Q**). SCM-A skeletons displayed hypoplastic development of the coronoid, angular, and condylar processes (**Fig. 5N**) – elements exquisitely sensitive to reduced *Dlx* dosage (Depew et al., 2005; Jeong et al., 2008). DCM mandibles had complete ablation of these proximal processes and/or fusion with components of the 'hinge' and upper-jaw (syngnathia) (**Fig. 5O, O', Fig. S9A-C**). Fusions included loss of the primary and secondary jaw joint articulations that varied amongst and within (left to right) DCM skeletons. Thus, some DCM embryos showed a nearly complete loss of patterning identity for the structures involved (**Fig. 5O'**), whereas others had apparent fusions between squamosal, maxillary and mandibular elements (**Fig. 5O, Fig. S9B, C**). DCM mandibles also showed defects along the mediolateral axis, with ectopic ossifications sometimes observed projecting orally from the mis-patterned mandible (**Fig. 5P, Q**). Jaw regions more distal to the hinge, such as the frontal process, the foramen of the maxilla (**Fig. 5K, L**) and lower incisors of the mandible, were less affected (**Fig. 5M-O**). Thus a modest shortening of the distal mandible was apparent in SCM-A (**Fig. 5N**) and this defect was slightly more severe in DCM skeletons (**Fig. 5O, O'**).

Tfap2 and *Dlx* mutants show overlap of cranial base and cranial sidewall defects

We next examined additional skeletal elements derived from the BA1 hinge-associated regions that form the NC-derived chondrocranium and neurocranium (i.e. cranial base and cranial sidewalls)(**Fig. 6**). These regions are susceptible to ablations and ectopias in *Dlx* LOF mutants (Depew et al., 2005; Qiu et al., 1997; Qiu et al., 1995). We first studied E15.5 cartilage preparations to determine how chondrocranial elements, such as Meckel's cartilage, the malleus and the ala temporalis were affected by *Tfap2* mutations (**Fig. 6A-F, Fig. S10**). As compared to controls, SCM-A embryos displayed a shorter Meckel's cartilage that failed to make a continuous connection at the proximal end with the malleus (**Fig. S10B, E**). Defects were more severe in DCM embryos with Meckel's cartilage about ½ it's normal length, not fused at the midline, often deviating in its projection, and failing to connect to a definitive malleus (**Fig. 6C, F, Fig. S10C, F**). The ala temporalis, whose development is sensitive to *Dlx*-dosage, is a derived palatoquadrate element that together with the lamina obturans eventually forms the alisphenoid bone (Cerny et al., 2004; Depew et al., 2002). In SCM-A embryos this cartilage was malformed and lacked the foramen (**Fig. 6E**). In DCM embryos, the ala temporalis failed to form, replaced by rudimentary cartilage elements that appeared to articulate with – or be non-continuous pieces of – Meckel's cartilage (**Fig. 6F**). Consistent with these earlier cartilage defects, E18.5 SCM-A and DCM skeletal preparations displayed a markedly affected alisphenoid bone (**Fig. 6G-I**). Thus, the alisphenoid bone was smaller in the SCM-A embryos than in controls and lacked the normal foramina (**Fig. 6G, H**). Interestingly, however, in a significant fraction of these SCM-A mice (~40%, **Table S1B**) the adjacent squamosal bone had developed foramina, a feature absent from controls. In DCMs, the alisphenoid was severely misshapen and hypoplastic, and the squamosal bones were missing or severely transformed (**Fig. 6I, also see Fig. 5I, O**).

Dlx mutants exhibit ectopic skeletal struts and ectopic lateral cartilage/bony elements associated with the cranial base (Depew et al., 2005; Qiu et al., 1997; Qiu et al., 1995). Examination of the E15.5 DCM chondrocranium also revealed that these had ectopic cartilage struts attaching to the cranial base, accompanied by loss of the alicochlear commissure (**Fig. 6F**). Although such ectopic struts were not seen in the E15.5 SCM-A preparations, by E18.5 they were present in both SCM-A and DCM skeletons (**Fig. 6K, L, Fig. S9D-G**). Like the reported ectopias in particular *Dlx* LOF mutants (Depew et al., 1999; Depew et al., 2005; Qiu et al., 1997; Qiu et al., 1995), these struts varied in appearance between SCM-A and DCMs but were never observed in controls (**Fig. 6J**). Specifically, SCM-A embryos generally displayed a single, ossified strut extending laterally from the basisphenoid and often fusing with the gonial (**Fig. 6K**). In contrast, DCM skeletons had multiple and more irregular ectopic struts extending from the cranial base, including some with apparent intermittent cartilaginous 'joints' (**Fig. 6L, Fig. S9D-G**). In addition, unidentifiable cartilage and bony elements of variable morphology, reminiscent of the ectopic 'palatoquadrate-like' structure observed in *Dlx*-mutants (Depew et al., 2005), were noted at the lateral aspects of DCM skulls (yellow arrowheads in **Fig. 5I, also see Fig. S9H-J**).

Additional defects in derivatives of BA1 and more caudal BA's, such as the bones and cartilages of the ear, hyoid, and thyroid, again, mirrored those seen in *Dlx* mutants (**Fig. 6M-T**). In regard to the ear, these defects were most severe in DCMs, with loss of the gonial and tympanic bones (**Fig. 6I, L, N**), disrupted projection of the styloid process (**Fig. 6N**), and loss or transformation of the cartilage primordia of the middle ear bones (**Fig. 6N**). A range of severity was also apparent with respect to the hyoid and its association with the cranial base (**Fig. 6O-T**). Unlike control mice (**Fig. 6O, R**) both SCM-A and DCM embryos exhibited cleft or 'pinched' hyoids that were often fused to the thyroid cartilage as well as displaying abnormal pterygoids that were positioned more rostrally (**Fig. 6P, Q, S, T**). Moreover, in DCMs, the abnormal hyoid-thyroid cartilage was also fused to both the pterygoids and the basisphenoid (**Fig. 6Q, T**).

Taken together, these findings indicate that both the *Tfap2* and *Dlx* gene families show a dosage effect on the craniofacial skeleton dependent on the number and type of mutant alleles present. The loss of AP-2α and AP-2ß in the NC does not recapitulate the phenotype of the more extreme *Dlx* LOF allelic combinations (e.g. *Dlx5*$^{-/-}$ *Dlx6*$^{-/-}$), but instead mimicked intermediate *Dlx* mutant phenotypes consistent with the observed ~50% reduction in *Dlx* gene expression seen in DCMs (**Fig. 3**). Further, the similarity in skeletal defects between the *Dlx* and *Tfap2* mutants extended to certain external features including low-set ears, microtia and microglossia (**Fig. 1**). Interestingly, for certain *Dlx* LOF mutant combinations, mandibular clefting was often associated with the homeotic transformation of lower-jaw structures into more 'upper-jaw like' structures – including the emergence of ectopic vibrissae on the lower-jaw (Beverdam et al., 2002; Depew et al., 2002; Depew et al., 2005). In this respect, the presence of structures with the superficial appearance of rows of ectopic vibrissae on the lower-jaw of E14.5 DCM embryos is suggestive of a possible homeotic transformation (**Fig. S11A-C**). Similarly, the presence of foramina in the SCM-A squamosal bone may indicate a partial transformation towards the normal morphology of the adjacent alisphenoid bone (**Fig. 6H**). However, it was not

possible to assess this feature in DCMs as these bones are missing or severely transformed (**Fig. 6I**). Overall, though, in agreement with the molecular analysis, morphological features in DCMs are consistent with altered *Dlx*-signaling resulting in a major disruption to the BA1-MxP/MdP 'hinge-associated' structures. Moreover, these observations indicate that regulation of *Dlx* gene expression represents a major function of AP-2α/ß in the BA1 NCCs.

DISCUSSION

AP-2 function in the cranial neural crest

Here we have shown that AP-2α and AP-2ß function cooperatively, and cell autonomously, within the cranial NCCs to orchestrate craniofacial development (see **Fig. 7**). Previous studies have shown that loss of each gene alone in the NCC results in limited defects (Brewer et al., 2004; Martino et al., 2016). Here we demonstrate that pathology worsens as an additional allele is deleted from the remaining paralog, with loss of *Tfap2a* alleles showing greater effects than removal of *Tfap2b* alleles. Ultimately, deletion of both paralogs simultaneously using *Wnt1:CRE* results in major craniofacial defects impacting the BAs and the midface. These findings are consistent with the two AP-2 paralogs exerting cooperative and redundant roles in face development, particularly impacting late cranial NCC development. Such findings help resolve the apparent paradox that each individual AP-2 paralog has a limited role in mammalian NCC development (Auman et al., 2002; Brewer et al., 2004; Martino et al., 2016), whereas in other gnathostomes AP-2 is postulated to act as a conserved master-regulator of the NCC lineage (Green et al., 2015; Hong et al., 2014; Rada-Iglesias et al., 2012; Rada-Iglesias et al., 2013; Simoes-Costa and Bronner, 2015; Trainor, 2014). These findings also have substantial bearing on the interpretation of results derived from the study of gene expression in human and chimp NCC-derivatives. Genome-wide analysis of active enhancers in such NCC lines demonstrated an over-representation of AP-2 binding site sequences, and further indicated

using ChIP that AP-2 proteins were detected at many of these sites. Additionally, nucleotide changes within AP-2 binding sites between human and chimp genomes often reduced AP-2 binding, with concomitant loss of H3K27ac levels, and reduced gene expression levels. Overall, these primate studies suggested that the AP-2 proteins were central to NCC enhancer function and that changes in AP-2 binding may drive craniofacial morphology differences between species (Prescott et al., 2015; Rada-Iglesias et al., 2012). Although these studies focus mainly on AP-2α, it is now clear that AP-2 function in NCC development should be considered in the context of all expressed paralogs. For example, although the over-representation of AP-2 binding at human NCC enhancers was attributed to AP-2α, AP-2ß shares an identical DNA binding motif (Mohibullah et al., 1999; Williams and Tjian, 1991a, b; Zhao et al., 2001) and many antibodies used for ChIP-Seq detect not only AP-2α, but also other AP-2 proteins. Thus, these sites – and associated chromatin features and attributed influences on primate craniofacial morphology – likely represent coordinated AP-2α/AP-2ß targets. Indeed, RNAseq analysis of these human NCC cultures identified both *TFAP2A* and *TFAP2B* to be highly enriched relative to the embryonic stem cells and neurospheres from which they were derived (Rada-Iglesias et al., 2012), while *TFAP2C* – *TFAP2E* were either expressed at low levels or not at all, in a pattern highly reminiscent of the E8.5 mouse NCCs (Minoux et al., 2017). Thus, at least *in vitro* for human and *in vivo* for mouse, NCCs share common AP-2 paralog expression. Furthermore, the presence of AP-2α/AP-2ß appears to be required for important aspects of NCC GRN expression in both mouse and primates. Such findings are important in the context of dominantly-inherited human Branchio-Oculo-Facial and Char Syndromes since mutations in one allele of *TFAP2A* or *TFAP2B*, respectively, could interfere with global AP-2 function in the NCCs via a dominant negative mechanism of action (Li et al., 2013; Milunsky et al., 2008; Satoda et al., 2000).

The conclusion that combinations of AP-2 genes, notably AP-2α and AP-2ß, are important in NCC development is also supported by the concerted action of these genes in the generation of trunk NCC derivatives including the enteric nervous system and melanocytes (Seberg et al., 2017). Given these observations, it will be important to determine if these two AP-2 TFs are also critical in other NCC populations that contribute to tissues such as the heart and adrenal gland. A deeper understanding of AP-2α/ß's molecular function in these additional NCC derivatives will establish whether regulation of key developmental genes – including homeobox TFs – is a conserved function of AP-2 in the NC or if this mechanism is unique to the NCCs of BA1. Similarly, identifying whether AP-2α/ß regulate survival of a subpopulation of post-migratory cells, in this case approximating to the hinge domain, in additional derivatives outside the craniofacial region will be an important facet of further understanding AP-2's cellular functions.

AP-2 function during NCC specification

Despite major NCC-derivative defects in the head and trunk of DCM embryos, early NCC specification in this mouse model appears unaffected. This is interesting since loss of AP-2 paralogs (singly or redundantly) in non-mammalian vertebrates including Xenopus and zebrafish disrupts NCC specification (de Croze et al., 2011; Hoffman et al., 2007; Hong et al., 2014; Li and Cornell, 2007; Luo et al., 2003). Several possibilities exist for why NCC specification is largely intact in DCM embryos. First, the *Wnt1*:CRE driver may mediate gene deletion post-NCC specification. However, we do not favor this model since preliminary data show that *Sox2-CRE* generated DCMs, which lose both AP-2 genes in the early epiblast prior to NCC specification, still undergo NCC development (EVO, unpublished observations). Second, additional paralogs, particularly *Tfap2c* may also function redundantly with *Tfap2a/Tfap2b* in early stages of NCC specification such that loss of all three paralogs would be required to

disrupt NCC formation. Third, AP-2 paralogs may not only act autonomously within the NCCs but also non-cell autonomously, particularly through their expression in the embryonic ectoderm, with both modes impacting overall NCC formation and function (Knight et al., 2005; Meulemans and Bronner-Fraser, 2002). Finally, AP-2 proteins may have distinct roles in mammalian versus non-mammalian NCC development – a feature that has previously been posited for additional gene families in the mouse (Barriga et al., 2015). Future experiments will be necessary to distinguish between these models.

Potential models of AP-2α/ß activity within BA1 NCCs

Mice with NCC-specific loss of *Tfap2a*/*Tfap2b* expression add to a small group of models that present with hinge defects including syngnathia. Prominent amongst these are loss of function mutations in *Dlx* gene family that normally function to subdivide BA1 into upper- and lower-jaw identities (Acampora et al., 1999; Beverdam et al., 2002; Depew et al., 1999; Depew et al., 2002; Depew et al., 2005; Jeong et al., 2012; Jeong et al., 2008; Qiu et al., 1997; Qiu et al., 1995). Manipulation of the endothelin (EDN) signaling pathway also impacts the development of the upper and lower jaws, with the *Dlx* genes acting as critical targets (Clouthier et al., 2010). Recent studies have further shown that reduced expression of *Fgf8* or *Foxc1* can cause this pathology (Inman et al., 2013), as can overexpression of BMP4 in NCCs (He et al., 2014). However, both *Fgf8* and *Foxc1* are up-regulated in the DCM samples, and changes in the expression of BMP pathway genes associated with facial development are not significantly altered in the DCM model (**Table S2** and **Fig. S12**). Instead, molecular profiling of the MdP indicated that loss of AP-2α/ß-activity resulted in alterations of multiple transcriptional regulators – including the entire *Dlx* gene family. Notably, this reduction in *Dlx* expression occurred without changes in the mRNA levels of EDN pathway components (e.g. *Edn1*, *Ece*, *Plc*, *Ednra*, *Mef2c*, Table S2). Such findings imply that AP-2 functions to regulate *Dlx* expression through a node independent or downstream of EDN-signaling in the NC.

How then might AP-2α/ß cooperatively regulate craniofacial patterning autonomously within the NCCs to drive proper hinge formation, ultimately facilitating upper- and lower-jaw registration? One possibility is that AP-2 regulates the survival of a small population of cells within BA1, such that NCC-specific loss of *Tfap2a/Tfap2b* induces apoptosis at the intersection of the MdP and MxP. Loss of these BA1 hinge domain cells, which would normally express *Emx2*, would then subsequently result in syngnathia development. At the same time, the considerable overlap between AP-2 and DLX LOF phenotypes suggests that there is also a more global impact on the expression of homeobox TFs that extends beyond the limited cell death observed in DCMs. This conclusion is also supported by the reduction of *Dlx* expression observed in DCMs as well as the overlap between DCM and *Dlx5*$^{-/-}$*Dlx6*$^{-/-}$ MdP mRNA expression profiles. Theoretically, such additional regulatory mechanisms can be split into direct (**Fig. 7D**) or indirect (**Fig. 7E**) modes of action. First, for the direct scenario, AP-2α and/or AP-2ß would bind directly to critical *cis*-elements associated with relevant genes to either activate or repress transcription within this BA1 GRN. In support of this direct model, homologs of at least 142 of the 182 altered genes in DCMs have an associated AP-2 bound region in the human *in vitro* derived NCCs, the majority of which (77%) are also associated with active or poised histone marks (Rada-Iglesias et al., 2012). The involvement of AP-2 with these *cis*-acting sequences maybe critical for NCCs to respond appropriately to external signals as they enter the facial prominences (Minoux et al., 2017). Various indirect models can also be proposed in which AP-2α/ß may modulate the transcript levels of an intermediary TF or a chromatin effector, or alternatively act post-transcriptionally to alter the properties of a protein complex required for gene expression (**Fig. 7E 'Z'**). Ultimately, both direct and indirect mechanisms are likely involved to coordinate the GRNs responsible for BA1 development. Teasing apart these potential mechanistic roles of AP-2α/ß will be a major priority in further understanding their function in normal craniofacial development as well as how their aberrant expression results in human birth defects.

ACKNOWLEDGEMENTS

We would like to thank Dr. Timothy Nottoli (Yale University) for targeted ES-cell injections in generation of *Tfap2b* mice, Drs. Sonia Leach and Joan Hooper (University of Colorado – Denver) for additional bioinformatic support, Irene Choi and Dr. Rebecca Green (University of Calgary) for assistance with the mouse lines, the DSHB at the University of Iowa for antibodies used in these studies, the Facebase consortium, and the University of Colorado – Denver Microarray and Genomics Core for RNA-sequencing. In addition, we would like to thank the many members of the Department of Craniofacial Biology at the University of Colorado – Denver who provided critical review of initial drafts of this manuscript, particularly Drs. Katherine Fantauzzo, Kristin Artinger, and Andre Tavares.

COMPETING INTERESTS: No competing interests declared

FUNDING: EVO: F32DE023709, 1K99DE026823; TW: 2R01 DE12728, 1U01DE024429

DATA AVAILABILITY: All raw sequencing data will be deposited at the Gene Expression Omnibus (GEO) maintained by the National Center for Biotechnology Information (NCBI).

MATERIALS AND METHODS

Mice: As previously stated (Van Otterloo et al., 2016) this study was carried out in strict accordance with the recommendations in the Guide for the Care and Use of Laboratory Animals of the National Institutes of Health. The protocol was approved by the Institutional Animal Care and Use Committee of the University of Colorado, Denver. Noon on the day that a copulatory plug was present was denoted as embryonic day 0.5. For the majority of experiments littermate embryos were used when comparing between genotypes. Yolk sacs or tail clips were used for genotyping. DNA for PCR was extracted using DirectPCR Lysis Reagent (Viagen Biotech. Inc, Los Angeles, CA) plus 10 µg/ml Proteinase K (Roche, Basel, Switzerland), incubated overnight at 65°C, followed by heat inactivation at 85°C for 45 minutes (mins). Samples were then used directly for PCR-based genotyping using primers (**Table S4**) at a final concentration of 200 nM using the Qiagen DNA polymerase kit, including the optional Q Buffer solution (Qiagen, Valencia, CA).

Sox2:CRE (Hayashi et al., 2002), *Wnt1*:CRE (Danielian et al., 1998), and *Gt(ROSA)26Sor*^{tm1Sor}*/J* [*Rosa26 reporter*/R26r/; (Soriano, 1999)] mice were obtained from the Jackson Laboratory (Bar Harbor, ME). The *Tfap2a* alleles used in this study were previously described, including the *Tfap2a*-null (Zhang et al., 1996), *Tfap2a*^{tm2Will}*/J* [*Tfap2a* floxed conditional; (Brewer et al., 2004)], and *Tfap2a*^{tm1Hsv}*/J* [*Tfap2a-lacZ* knock-in; (Brewer et al., 2002)] alleles. Once established, lines were maintained on a Black Swiss (strain code 492, Charles River, Wilmington, MA) background.

To generate the *Tfap2b* alleles utilized in this study, a P1 genomic clone from 129 DNA corresponding to the *Tfap2b* locus was isolated by library screening and subsequently an ~1.65 kilobases (kb) *BamHI* fragment containing exon 5 and flanking sequences was isolated. This clone was extended by 70 nucleotides (nts) at the 5' end using a PCR based strategy to introduce an *NheI* site ~340 basepairs (bps) upstream of exon 5, and by ~6kb at the 3' end by the addition of a *BamHI – HindIII* fragment from the P1 clone that extends across exon 6 and

into exon 7. An *Acc65I* site 70nts upstream of exon 6 was repaired with T4 DNA polymerase and used to introduce a *LoxP FRT neo FRT* cassette derived from a modified version of plasmid PK11 (Lewandoski et al., 1997) containing a *LoxP* at the 5' end rather than at the 3' end. A second *LoxP* site was introduced at a *PshAI* site ~50nts downstream of exon 6, such that an ~260bp fragment containing exon 6, which encodes a vital part of the DNA binding and dimerization of AP-2ß, is flanked by *LoxP* sites. Two copies of the thymidine kinase selection cassette were then introduced downstream of the *HindIII* site generating a targeting vector that was verified by sequence analysis (**Fig. S3**). The construct was then linearized with *NheI* prior to electroporation into 129S1/SV W9.5 ES cells. Clones showing appropriate recombination at both the 5' and 3' end were identified using long range PCR and Southern blotting using primer sequences or probes outside the region of homology. Three positive clones were identified and these were karyotyped. Subsequently, a euploid ES clone was used to generate chimeras, and these were bred with Black Swiss mice to obtain germline transmission of the *Tfap2b-neo* allele. Next, the *neo* cassette was removed by breeding to *(ACTFLPe)9205Dym/J* (Jackson Labs) to generate the *Tfap2b-flox* allele (**Fig. S3).** The *Tfap2b*-null allele was then generated by breeding with *Tmem163*$^{Tg(ACTB\text{-}cre)2Mrt}$*/J* mice (Jackson Labs). Successful modification of offspring was confirmed by PCR analysis and mice containing these alleles have been maintained for multiple generations on a Black Swiss background.

The following genetic scheme was generally implemented to generate embryos for experiments. The male adult, which was *Tfap2a*$^{null/wt;}$*Tfap2b*$^{null/wt}$*;CRE*+ (*Wnt1*:CRE for example) was crossed with a female that was, *Tfap2a*$^{flox/flox}$*;Tfap2b*$^{flox/flox}$ (and *R26r* homozygous for appropriate experiments). This cross would generate SCM-A, SCM-B, and DCM each at an ~1:8 ratio (12.5%), with the remainder being various combinations of alleles serving as controls. Note, SCM embryos would be either, *Tfap2a*$^{null/flox}$*;Tfap2b*$^{wt/flox}$*;CRE*+ (SCM-A) or *Tfap2a*$^{wt/flox}$*;Tfap2b*$^{null/flox}$*;CRE*+ (SCM-B) and DCM embryos would be *Tfap2a*$^{null/flox}$*;Tfap2b*$^{null/flox}$*;CRE*+. By virtue of this breeding scheme, all SCMs would be

conditionally heterozygous for the alternate paralog, as described in results. The exception to the males listed above included experiments utilizing the *Tfap2a-lacZ* knock-in (KI) allele (Brewer et al., 2002), in which case males used for breeding were *Tfap2a*$^{KI/wt}$*;Tfap2b*$^{null/wt}$*;CRE*+.

Western blot analysis: For Western blot analysis, E12.5 whole heads (*Sox2*:CRE experiments) or E10.5 craniofacial prominences (*Wnt1*:CRE experiments) were lysed, on ice, in RIPA buffer containing protease inhibitors (ThermoScientific™ Protease Inhibitor Cocktail, ThermoScientific, Waltham, MA). Briefly, as described previously (Van Otterloo et al., 2016), tissue was first minced with a disposable pestle followed by further disruption using a tissue homogenizer (Pro200 homogenizer, PRO Scientific Inc, Oxford, CT). Following homogenization, samples were allowed to lyse on ice for ~30 mins. After lysis, 6x Laemmli Buffer (plus ß-mercaptoethanol) was added to a 1x final concentration and samples stored at -80°C until use. On the day of use, samples were boiled at ~100°C for 10 mins, spun at 13,000 rpm for 10 mins, and then ~ 20 µL of lysate loaded per lane on a 12% stacking SDS polyacrylamide gel and separated at 100V. Once samples were resolved, they were transferred onto a nitrocellulose membrane overnight at 4°C and 40mA. Following transfer, membranes were blocked one hour (hr) with 3% powdered milk in TBST (TBSTM), and then incubated with the primary antibody, diluted in TBSTM, overnight at 4°C (rabbit anti-TFAP2 polyclonal, H-87/sc-8976, 1:1000, Santa Cruz Biotechnology, Inc., Dallas, TX). Following primary antibody incubation, membranes were washed 4 x 20 min with TBSTM and then incubated with an infrared (IR)-labeled (goat-anti-rabbit) secondary antibody for 1 hr (1:20,000 in TBST, LI-COR Biosciences, Lincoln, NE). The membrane was then washed 4 x 20 min with TBSTM, 5 min with PBS, and then imaged on a LI-COR Odyssey imager. Serving as a loading control, post-imaging, the membrane was again blocked with TBSTM, 4 x 20 min, and an additional primary antibody was added to the membrane (anti-GAPDH, mouse monoclonal G8795, Sigma-Aldrich, St. Louis, MO, or rabbit anti-ACTIN polyclonal, H-196, 1:1000, Santa Cruz Biotechnology, Inc., Dallas, TX) and a similar

washing, secondary, and imaging procedure carried out, using the appropriate species-specific secondary antibody.

Skeletal analysis

Bone and cartilage staining: Embryos were collected at appropriate time points and processed as previously described (Van Otterloo et al., 2016).

Cartilage staining: Embryos were collected at appropriate time points and processed as previously described (Van Otterloo et al., 2016).

ß-galactosidase staining: ß-galactosidase (ß-gal) staining of whole embryos was carried out as previously described (Seberg et al., 2017). Briefly, dissected samples were fixed for 30 min in 0.2% glutaraldehyde (in PBS) at room temperature. Following fixation, embryos were washed 3 x 30 min with a 'lacZ' rinse buffer [see (Seberg et al., 2017)] at room temperature. Following washes, embryos were developed in a 'lacZ staining' solution ('lacZ' rinse solution plus 1 mg/ml X-Gal, Invitrogen/Life Technologies, Carlsbad, CA) in the dark at 37°C until desirable ß-gal signal was produced (~1-2 hrs for *R26r* x *Wnt1*:CRE experiments). Post-staining, embryos were briefly rinsed multiple times in PBS and then post-fixed in 4% paraformaldehyde overnight at 4°C, while protected from light.

***In situ* hybridization/Immunohistochemistry/Immunofluorescence/H&E staining** Whole-mount immunohistochemistry was carried out essentially as described (Pabst et al., 2003), replacing 10% horse serum with 5% milk as a blocking reagent. The anti-neurofilament antibody (Dodd et al., 1988) was used at a 1:100 dilution (IgG clone 2H3, obtained from the Developmental Studies Hybridoma Bank, created by the NICHD of the NIH and maintained at The University of Iowa, Department of Biology, Iowa City, IA).

Hematoxylin and Eosin (H&E) staining was carried out as previously described (Cardiff et al., 2014; Van Otterloo et al., 2016).

In situ hybridization was carried out as previously described (Simmons et al., 2014; Van Otterloo et al., 2016).

Cell proliferation and cell death analysis: For analysis of cell proliferation and cell death, embryos were collected at various developmental time-points and fixed over-night in 4% PFA at 4°C. Following fixation, tissue was dehydrated in a graded series of ethanol and xylene and subsequently embedded in paraffin. After embedding, samples were sectioned with a Leica RM 2235 microtome at 10-12 µm, onto charged glass slides. After drying, sections were processed for immunofluorescence. Briefly, paraffin was washed from tissue sections with 3 x 10 minute washes in xylene, followed by rehydration in a graded series of EtOH and water. Following rehydration, samples were washed in PBS for 5 mins at room temperature. Subsequently, an antigen retrieval procedure was carried out, which involved placing samples in 10 µM citric acid (pH 6.0) and boiling samples in a Cuisine Art electric pressure cooker, on high for 5 mins. Following antigen retrieval, tissue was washed 1x in TBST, followed by blocking for 1 hr in TBSTM. Sections were then incubated over-night in primary antibody, diluted 1:250 in TBSTM at 4°C in a humidified chamber. Primary antibodies included anti-p-Histone H3 (sc-8656-R, Santa Cruz Biotechnology, rabbit polyclonal) or anti-Cleaved Caspase 3 (5A1E, Cell Signaling Technology, rabbit monoclonal), for cell proliferation or death, respectively. Following primary antibody incubation, samples were washed 2 x 10 mins in TBST at room temperature, followed by a 30 minute wash in TBSTM. Samples were then incubated 1 hr with a secondary antibody (Goat anti-Rabbit IgG, Alexa Flour 488 conjugate, ThermoFisher Scientific/Invitrogen, catalog number R37116) and DRAQ5 (abcam, ab108410) nuclear stain, diluted 1:250 and 1:5,000,

respectively, in TBSTM. Processed samples were imaged on a Leica TCS SP5 II confocal microscope and individual images taken for visualization.

RNA expression profiling:

RNAseq: For the MdP RNA-seq, E10.5 DCM and litter-matched control embryos were dissected in ice-cold PBS. Subsequently, the mandibular prominences were carefully dissected from each embryo and stored in RNAlater (Ambion/Life Technologies) until later use. Following genotyping, RNA was extracted, essentially as previously described (Van Otterloo et al., 2016), from paired (i.e. left and right) mandibular prominences (3 control and 3 DCM embryos – 3 biological replicates) using the microRNA Purification Kit (Norgen Biotek Corp., Thorold, ON), following manufacturer's protocol. Following elution, mRNA was further purified using the Qiagen RNAeasy Kit (Qiagen, Valencia, CA), according to manufacturer's protocol. Quality of extracted mRNA was assessed using DNA Analysis ScreenTape (Agilent Technologies, Santa Clara, CA) to ensure that it was of sufficient quality for library production. Following validation of extracted mRNA, cDNA libraries were generated using the Illumina TruSeq Stranded mRNA Sample Prep Kit (Illumina, San Diego, CA). Following library generation and subsequent quality control assessment, cDNA was sequenced using the Illumina HiSeq2500 platform and single-end reads (1x150).

Data analysis (Bioinformatic pipelines):

1) *Pipeline 1*: For an initial 'pipeline' to identify mRNA-based gene expression changes between control and DCM mandibular prominences, derived fastq sequences were analyzed by applying a custom computational workflow (Baird et al., 2014; Bradford et al., 2015; Henderson et al., 2015; Maycotte et al., 2015) consisting of the open-source gSNAP (Wu and Nacu, 2010), Cufflinks (Trapnell et al., 2010), and R for sequence alignment and ascertainment of differential gene expression. In short, reads generated were mapped to the mouse genome (Mm10) by

gSNAP, expression (FPKM) derived by Cufflinks, and differential expression analyzed with ANOVA in R.

2) *Pipeline 2*: For a secondary 'pipeline' to further refine mRNA-based gene expression changes between control and DCM mandibular prominences, fastq sequence reads were first trimmed using the Java software package Trim Galore! (Babraham Bioinformatics, Babraham Institute) and subsequently mapped to the Mm10 genome using the HISAT2 software package (Pertea et al., 2016) (both with default settings). Following mapping, RNA expression levels were generated using StringTie (Pertea et al., 2016) and differential expression computed between genotypes using CuffDiff2 (Trapnell et al., 2013), with a significance cut-off value of $Q < 0.05$ (FDR corrected P-value).

Hierarchical clustering: Genes identified as significantly altered in their expression values that were present in both bioinformatic pipelines (Class III, '182 geneset') were used for clustering analysis based on their expression values calculated with pipeline 1 or pipeline 2. Hierarchical clustering and heatmap generation based on these gene expression changes were produced using the pheatmap R-package (written by Raivo Kolde, https://cran.r-project.org/package=pheatmap).

Pathway enrichment analysis: For functional annotation clustering of significantly upregulated and downregulated genes, the recently updated DAVID (v6.8) platform (Dennis et al., 2003), with default parameters, was used. Following functional annotation clustering, "annotation clusters" above a 2-fold enrichment threshold were considered. Gene-lists from both bioinformatic pipelines 1 and 2 were utilized, along with the overlapping 182 gene-set. In addition to DAVID, the online pathway analysis suite, Enrichr (Chen et al., 2013; Kuleshov et al., 2016) (http://amp.pharm.mssm.edu/Enrichr/), was utilized with the available gene-lists generated.

Gene set enrichment analysis: For gene set enrichment analysis (GSEA), the GSEA application

(Subramanian et al., 2005) was downloaded and implemented from the Broad Institute website (http://software.broadinstitute.org/gsea/index.jsp). First, using gene expression and Q-values calculated from bioinformatic pipeline 1, a ranked gene dataset file was generated (.rnk file). Subsequently, a curated dataset that included multiple gene-lists was generated (**Table S3**). Lists included, genes up-regulated, down-regulated, or both, in the MdP of *Dlx5*$^{-/-}$*Dlx6*$^{-/-}$ mutants (Jeong et al., 2008) as well as a curated list of homeobox transcription factors (Holland et al., 2007). The 'Dlx-associated' lists were calculated by reanalyzing data deposited to the (GEO) repository (dataset GSE4774) utilizing the GEO2R software package (Davis and Meltzer, 2007) and retaining genes that showed a > 1.5-fold change between control and *Dlx5*$^{-/-}$*Dlx6*$^{-/-}$ mutant samples and a p-value < 0.002.

Previously generated datasets utilized in study:

RNA-seq datasets used for analyzing *Tfap2* mRNA paralog expression: *E8.5 pre-migratory cranial NCCs* – Pre-processed RNAseq datasets (Minoux et al., 2017) were downloaded from the GEO repository (dataset GSE89434, file GSE89434_Minoux_RNAseq_gene_counts.csv), and average normalized mRNA expression values calculated from the 3 biological replicate values listed. *E10.5-E12.5 cranial NCCs* – Facial prominences (MdP, MxP, and FNP) were micro-dissected from E10.5, E11.5 and E12.5 embryos – generated from in-crossing C57BL/6J wild-type adults – and superficial ectodermal layers separated from underlying mesenchyme, as described (Li and Williams, 2013). mRNA was extracted from each individual tissue source, cDNA generated, and sequenced following procedures listed above. mRNA expression levels were calculated, as described above, for 'Pipeline 1'. A more detailed and comprehensive analysis of the generation and analysis of the E10.5-E12.5 datasets will be presented elsewhere (Li H and Williams T, manuscript in prep.) and these datasets have been uploaded and are currently in queue for public availability at the Facebase Consortium (https://www.facebase.org/).

To generate expression percentiles for the various RNAseq datasets, a normalized ranked gene list was calculated for each. Briefly, after calculation of RNA expression values, the entire dataset was sorted based on expression levels and each gene ascribed a ranking within the dataset (i.e. rank of 1, being the gene with the highest mRNA expression, rank of 2, next highest…through, rank of n). Note, mRNA's with an RPKM of 0 would all correspond to an equal, and lowest, ranking within the dataset. Next, to normalize between RNAseq experiments, the rank value of each gene was then divided by the total number of genes within the dataset, generating a 'normalized-rank value'. Data was subsequently plotted inversely (so that the most highly expressed genes were near the top of the Y-axis), and location of *Tfap2* paralogs within the normalized ranked list highlighted.

E10.5 mouse cranial NCC histone ChIP-Seq: E10.5 MdP histone datasets were obtained from the GEO repository (dataset GSE89435). Raw fastq sequencing reads for H3K4me2, H3K27me3, and input were downloaded and reprocessed, essentially as described (Minoux et al., 2017). Briefly, raw reads were mapped to the mouse GRCm38/mm10 reference genome using the *QuasR* Bioconductor package (Gaidatzis et al., 2015), implementing the *qAlign* function. Subsequently, the *qCount* function was utilized to assess the number of reads per promoter region (transcription start site, ± 1 kb). ChIP enrichments were calculated using the formula described (Minoux et al., 2017), and resulting data graphed in Microsoft Excel 2016 (Microsoft Corporation, Redmond, WA). Subsequent to generating a scatterplot of H3K4me2-H3K27me3 enrichments, the 182 Class III gene-set, was mapped on top of these data points in Excel.

In vitro Human NCC TFAP2A and histone ChIP-Seq: To identify genes associated with TFAP2 ChIP-Seq data points, the previously published, pre-processed, ChIP-Seq datasets (Rada-

Iglesias et al., 2012) were downloaded from the GEO repository (dataset GSE28876, files NCC_TFAP2A, NCC_H3K4me3, and NCC_H3K27ac) in .bed file format. Subsequently, datasets were uploaded to the University of California Santa Cruz Genome Browser (UCSC genome browser) and the Table Browser function (https://genome.ucsc.edu/goldenpath/help/hgTablesHelp.html) utilized to transfer data to the online GREAT algorithm, version 3.0.0 (http://bejerano.stanford.edu/great/public/html/index.php) (McLean et al., 2010). Using default parameters, GREAT was implemented to generate a list of genes associated with AP-2 ChIP-Seq peaks (i.e. AP-2 binding) or AP-2 ChIP-Seq peaks that occurred within genomic regions containing active histone marks (e.g. H3K4me3 or H3K27ac). Overlapping of TFAP2A ChIP-Seq and histone mark datasets was carried out with the 'intersection' function in Table Browser prior to GREAT analysis. After gene-lists were generated, the VLOOKUP function in Excel was utilized to identify common genes between the 182 significantly altered genes in DCM embryos and the GREAT-generated gene-lists.

cDNA synthesis and real-time PCR: For real-time PCR experiments, embryos were harvested at E9.5 and BA1 dissected off for RNA isolation. Tissue was stored in RNAlater at -20 °C until genotyping was completed on samples. Three biologically independent control and DCM embryos were collected. Following positive identification of genotypes, tissue was equilibrated at 4 °C for one day, RNAlater removed, and RNA extracted from tissue samples using the RNeasy Mini Kit (Qiagen, Germantown, MD). Following RNA isolation and quantification, cDNA was generated using 200 ng/µL of RNA and the SuperScript™ III First-Strand Synthesis Kit (Invitrogen, ThermoFisher Scientific, Waltham, MA), along with the optional on-column DNase digestion. Once cDNA was generated, quantitative real-time PCR analysis was conducted using a Bio-Rad CFX Connect instrument (Bio-Rad, Hercules, CA), Sybr Select Master Mix (Applied Biosystems, ThermoFisher Scientific), and 20 µL reactions (all reactions performed in triplicate). All primers (sequences available upon request) were designed to target exons flanking (when

available) large intronic sequences. Relative mRNA expression levels were quantified using the $^{\Delta\Delta}$Ct method (Dussault and Pouliot, 2006) and an internal relative control (*ß-actin*). Significance (standard student T test) was calculated using a previously published Statistical Analysis Software (SAS) package (Yuan et al., 2006).

REFERENCES

Acampora, D., Merlo, G.R., Paleari, L., Zerega, B., Postiglione, M.P., Mantero, S., Bober, E., Barbieri, O., Simeone, A., Levi, G., 1999. Craniofacial, vestibular and bone defects in mice lacking the Distal-less-related gene Dlx5. Development 126, 3795-3809.

Ahmed, M., Xu, J., Xu, P.X., 2012. EYA1 and SIX1 drive the neuronal developmental program in cooperation with the SWI/SNF chromatin-remodeling complex and SOX2 in the mammalian inner ear. Development 139, 1965-1977.

Alappat, S., Zhang, Z.Y., Chen, Y.P., 2003. Msx homeobox gene family and craniofacial development. Cell Res 13, 429-442.

Auman, H.J., Nottoli, T., Lakiza, O., Winger, Q., Donaldson, S., Williams, T., 2002. Transcription factor AP-2gamma is essential in the extra-embryonic lineages for early postimplantation development. Development 129, 2733-2747.

Baird, N.L., Bowlin, J.L., Cohrs, R.J., Gilden, D., Jones, K.L., 2014. Comparison of varicella-zoster virus RNA sequences in human neurons and fibroblasts. J Virol 88, 5877-5880.

Bajoghli, B., Aghaallaei, N., Czerny, T., 2005. Groucho corepressor proteins regulate otic vesicle outgrowth. Dev Dyn 233, 760-771.

Barlow, A.J., Bogardi, J.P., Ladher, R., Francis-West, P.H., 1999. Expression of chick Barx-1 and its differential regulation by FGF-8 and BMP signaling in the maxillary primordia. Dev Dyn 214, 291-302.

Barriga, E.H., Trainor, P.A., Bronner, M., Mayor, R., 2015. Animal models for studying neural crest development: is the mouse different? Development 142, 1555-1560.

Bassett, E.A., Korol, A., Deschamps, P.A., Buettner, R., Wallace, V.A., Williams, T., West-Mays, J.A., 2012. Overlapping expression patterns and redundant roles for AP-2 transcription factors in the developing mammalian retina. Dev Dyn 241, 814-829.

Begbie, J., Graham, A., 2001. Integration between the epibranchial placodes and the hindbrain. Science 294, 595-598.

Beverdam, A., Merlo, G.R., Paleari, L., Mantero, S., Genova, F., Barbieri, O., Janvier, P., Levi, G., 2002. Jaw transformation with gain of symmetry after Dlx5/Dlx6 inactivation: mirror of the past? Genesis 34, 221-227.

Bradford, A.P., Jones, K., Kechris, K., Chosich, J., Montague, M., Warren, W.C., May, M.C., Al-Safi, Z., Kuokkanen, S., Appt, S.E., Polotsky, A.J., 2015. Joint MiRNA/mRNA expression profiling reveals changes consistent with development of dysfunctional corpus luteum after weight gain. PLoS One 10, e0135163.

Brewer, S., Feng, W., Huang, J., Sullivan, S., Williams, T., 2004. Wnt1-Cre-mediated deletion of AP-2alpha causes multiple neural crest-related defects. Dev Biol 267, 135-152.

Brewer, S., Jiang, X., Donaldson, S., Williams, T., Sucov, H.M., 2002. Requirement for AP-2alpha in cardiac outflow tract morphogenesis. Mech Dev 110, 139-149.

Cardiff, R.D., Miller, C.H., Munn, R.J., 2014. Manual hematoxylin and eosin staining of mouse tissue sections. Cold Spring Harb Protoc 2014, 655-658.

Cerny, R., Lwigale, P., Ericsson, R., Meulemans, D., Epperlein, H.H., Bronner-Fraser, M., 2004. Developmental origins and evolution of jaws: new interpretation of "maxillary" and "mandibular". Dev Biol 276, 225-236.

Chai, Y., Maxson, R.E., Jr., 2006. Recent advances in craniofacial morphogenesis. Dev Dyn 235, 2353-2375.

Chen, E.Y., Tan, C.M., Kou, Y., Duan, Q., Wang, Z., Meirelles, G.V., Clark, N.R., Ma'ayan, A., 2013. Enrichr: interactive and collaborative HTML5 gene list enrichment analysis tool. BMC Bioinformatics 14, 128.

Clouthier, D.E., Garcia, E., Schilling, T.F., 2010. Regulation of facial morphogenesis by endothelin signaling: insights from mice and fish. Am J Med Genet A 152A, 2962-2973.

Cobourne, M.T., Sharpe, P.T., 2003. Tooth and jaw: molecular mechanisms of patterning in the first branchial arch. Arch Oral Biol 48, 1-14.

Compagnucci, C., Debiais-Thibaud, M., Coolen, M., Fish, J., Griffin, J.N., Bertocchini, F., Minoux, M., Rijli, F.M., Borday-Birraux, V., Casane, D., Mazan, S., Depew, M.J., 2013. Pattern and polarity in the development and evolution of the gnathostome jaw: both conservation and heterotopy in the branchial arches of the shark, Scyliorhinus canicula. Dev Biol 377, 428-448.

Couly, G.F., Coltey, P.M., Le Douarin, N.M., 1993. The triple origin of skull in higher vertebrates: a study in quail-chick chimeras. Development 117, 409-429.

Danielian, P.S., Muccino, D., Rowitch, D.H., Michael, S.K., McMahon, A.P., 1998. Modification of gene activity in mouse embryos in utero by a tamoxifen-inducible form of Cre recombinase. Curr Biol 8, 1323-1326.

Davis, S., Meltzer, P.S., 2007. GEOquery: a bridge between the Gene Expression Omnibus (GEO) and BioConductor. Bioinformatics 23, 1846-1847.

de Croze, N., Maczkowiak, F., Monsoro-Burq, A.H., 2011. Reiterative AP2a activity controls sequential steps in the neural crest gene regulatory network. Proc Natl Acad Sci U S A 108, 155-160.

Dennis, G., Jr., Sherman, B.T., Hosack, D.A., Yang, J., Gao, W., Lane, H.C., Lempicki, R.A., 2003. DAVID: Database for Annotation, Visualization, and Integrated Discovery. Genome Biol 4, P3.

Depew, M.J., Liu, J.K., Long, J.E., Presley, R., Meneses, J.J., Pedersen, R.A., Rubenstein, J.L., 1999. Dlx5 regulates regional development of the branchial arches and sensory capsules. Development 126, 3831-3846.

Depew, M.J., Lufkin, T., Rubenstein, J.L., 2002. Specification of jaw subdivisions by Dlx genes. Science 298, 381-385.

Depew, M.J., Simpson, C.A., Morasso, M., Rubenstein, J.L., 2005. Reassessing the Dlx code: the genetic regulation of branchial arch skeletal pattern and development. J Anat 207, 501-561.

Dodd, J., Morton, S.B., Karagogeos, D., Yamamoto, M., Jessell, T.M., 1988. Spatial regulation of axonal glycoprotein expression on subsets of embryonic spinal neurons. Neuron 1, 105-116.

Dussault, A.A., Pouliot, M., 2006. Rapid and simple comparison of messenger RNA levels using real-time PCR. Biol Proced Online 8, 1-10.

Eckert, D., Buhl, S., Weber, S., Jager, R., Schorle, H., 2005. The AP-2 family of transcription factors. Genome Biol 6, 246.

Fish, J.L., Villmoare, B., Kobernick, K., Compagnucci, C., Britanova, O., Tarabykin, V., Depew, M.J., 2011. Satb2, modularity, and the evolvability of the vertebrate jaw. Evol Dev 13, 549-564.

Fonseca, N.A., Marioni, J., Brazma, A., 2014. RNA-Seq gene profiling--a systematic empirical comparison. PLoS One 9, e107026.

Gaidatzis, D., Lerch, A., Hahne, F., Stadler, M.B., 2015. QuasR: quantification and annotation of short reads in R. Bioinformatics 31, 1130-1132.

Green, S.A., Simoes-Costa, M., Bronner, M.E., 2015. Evolution of vertebrates as viewed from the crest. Nature 520, 474-482.

Gross, J.B., Hanken, J., 2008. Review of fate-mapping studies of osteogenic cranial neural crest in vertebrates. Dev Biol 317, 389-400.

Hamburger, V., 1961. Experimental analysis of the dual origin of the trigeminal ganglion in the chick embryo. J Exp Zool 148, 91-123.

Hayashi, S., Lewis, P., Pevny, L., McMahon, A.P., 2002. Efficient gene modulation in mouse epiblast using a Sox2Cre transgenic mouse strain. Mech Dev 119 Suppl 1, S97-S101.

He, F., Hu, X., Xiong, W., Li, L., Lin, L., Shen, B., Yang, L., Gu, S., Zhang, Y., Chen, Y., 2014. Directed Bmp4 expression in neural crest cells generates a genetic model for the rare human bony syngnathia birth defect. Dev Biol 391, 170-181.

Henderson, H.H., Timberlake, K.B., Austin, Z.A., Badani, H., Sanford, B., Tremblay, K., Baird, N.L., Jones, K., Rovnak, J., Frietze, S., Gilden, D., Cohrs, R.J., 2015. Occupancy of RNA Polymerase II Phosphorylated on Serine 5 (RNAP S5P) and RNAP S2P on Varicella-Zoster Virus Genes 9, 51, and 66 Is Independent of Transcript Abundance and Polymerase Location within the Gene. J Virol 90, 1231-1243.

Hoffman, T.L., Javier, A.L., Campeau, S.A., Knight, R.D., Schilling, T.F., 2007. Tfap2 transcription factors in zebrafish neural crest development and ectodermal evolution. J Exp Zool B Mol Dev Evol 308, 679-691.

Holland, P.W., Booth, H.A., Bruford, E.A., 2007. Classification and nomenclature of all human homeobox genes. BMC Biol 5, 47.

Hong, C.S., Devotta, A., Lee, Y.H., Park, B.Y., Saint-Jeannet, J.P., 2014. Transcription factor AP2 epsilon (Tfap2e) regulates neural crest specification in Xenopus. Dev Neurobiol 74, 894-906.

Huang da, W., Sherman, B.T., Lempicki, R.A., 2009a. Bioinformatics enrichment tools: paths toward the comprehensive functional analysis of large gene lists. Nucleic Acids Res 37, 1-13.

Huang da, W., Sherman, B.T., Lempicki, R.A., 2009b. Systematic and integrative analysis of large gene lists using DAVID bioinformatics resources. Nat Protoc 4, 44-57.

Inman, K.E., Purcell, P., Kume, T., Trainor, P.A., 2013. Interaction between Foxc1 and Fgf8 during mammalian jaw patterning and in the pathogenesis of syngnathia. PLoS Genet 9, e1003949.

Jeong, J., Cesario, J., Zhao, Y., Burns, L., Westphal, H., Rubenstein, J.L., 2012. Cleft palate defect of Dlx1/2-/- mutant mice is caused by lack of vertical outgrowth in the posterior palate. Dev Dyn 241, 1757-1769.

Jeong, J., Li, X., McEvilly, R.J., Rosenfeld, M.G., Lufkin, T., Rubenstein, J.L., 2008. Dlx genes pattern mammalian jaw primordium by regulating both lower jaw-specific and upper jaw-specific genetic programs. Development 135, 2905-2916.

Jiang, X., Iseki, S., Maxson, R.E., Sucov, H.M., Morriss-Kay, G.M., 2002. Tissue origins and interactions in the mammalian skull vault. Dev Biol 241, 106-116.

Knight, R.D., Javidan, Y., Zhang, T., Nelson, S., Schilling, T.F., 2005. AP2-dependent signals from the ectoderm regulate craniofacial development in the zebrafish embryo. Development 132, 3127-3138.

Knight, R.D., Nair, S., Nelson, S.S., Afshar, A., Javidan, Y., Geisler, R., Rauch, G.J., Schilling, T.F., 2003. lockjaw encodes a zebrafish tfap2a required for early neural crest development. Development 130, 5755-5768.

Kuleshov, M.V., Jones, M.R., Rouillard, A.D., Fernandez, N.F., Duan, Q., Wang, Z., Koplev, S., Jenkins, S.L., Jagodnik, K.M., Lachmann, A., McDermott, M.G., Monteiro, C.D., Gundersen, G.W., Ma'ayan, A., 2016. Enrichr: a comprehensive gene set enrichment analysis web server 2016 update. Nucleic Acids Res 44, W90-97.

Le Douarin, N., Kalcheim, C., 1999. The neural crest, 2nd ed. Cambridge University Press, Cambridge ; New York.

Lewandoski, M., Meyers, E.N., Martin, G.R., 1997. Analysis of Fgf8 gene function in vertebrate development. Cold Spring Harb Symp Quant Biol 62, 159-168.

Li, H., Sheridan, R., Williams, T., 2013. Analysis of TFAP2A mutations in Branchio-Oculo-Facial Syndrome indicates functional complexity within the AP-2alpha DNA-binding domain. Hum Mol Genet 22, 3195-3206.

Li, H., Williams, T., 2013. Separation of mouse embryonic facial ectoderm and mesenchyme. J Vis Exp.

Li, W., Cornell, R.A., 2007. Redundant activities of Tfap2a and Tfap2c are required for neural crest induction and development of other non-neural ectoderm derivatives in zebrafish embryos. Dev Biol 304, 338-354.

Luo, T., Lee, Y.H., Saint-Jeannet, J.P., Sargent, T.D., 2003. Induction of neural crest in Xenopus by transcription factor AP2alpha. Proc Natl Acad Sci U S A 100, 532-537.

Martino, V.B., Sabljic, T., Deschamps, P., Green, R.M., Akula, M., Peacock, E., Ball, A., Williams, T., West-Mays, J.A., 2016. Conditional deletion of AP-2beta in mouse cranial neural crest results in anterior segment dysgenesis and early-onset glaucoma. Dis Model Mech 9, 849-861.

Maycotte, P., Jones, K.L., Goodall, M.L., Thorburn, J., Thorburn, A., 2015. Autophagy Supports Breast Cancer Stem Cell Maintenance by Regulating IL6 Secretion. Mol Cancer Res 13, 651-658.

McBratney-Owen, B., Iseki, S., Bamforth, S.D., Olsen, B.R., Morriss-Kay, G.M., 2008. Development and tissue origins of the mammalian cranial base. Dev Biol 322, 121-132.

McGonnell, I.M., Graham, A., Richardson, J., Fish, J.L., Depew, M.J., Dee, C.T., Holland, P.W., Takahashi, T., 2011. Evolution of the Alx homeobox gene family: parallel retention and independent loss of the vertebrate Alx3 gene. Evol Dev 13, 343-351.

McLean, C.Y., Bristor, D., Hiller, M., Clarke, S.L., Schaar, B.T., Lowe, C.B., Wenger, A.M., Bejerano, G., 2010. GREAT improves functional interpretation of cis-regulatory regions. Nat Biotechnol 28, 495-501.

Meulemans, D., Bronner-Fraser, M., 2002. Amphioxus and lamprey AP-2 genes: implications for neural crest evolution and migration patterns. Development 129, 4953-4962.

Milunsky, J.M., Maher, T.A., Zhao, G., Roberts, A.E., Stalker, H.J., Zori, R.T., Burch, M.N., Clemens, M., Mulliken, J.B., Smith, R., Lin, A.E., 2008. TFAP2A mutations result in branchio-oculo-facial syndrome. Am J Hum Genet 82, 1171-1177.

Minoux, M., Holwerda, S., Vitobello, A., Kitazawa, T., Kohler, H., Stadler, M.B., Rijli, F.M., 2017. Gene bivalency at Polycomb domains regulates cranial neural crest positional identity. Science 355.

Mohibullah, N., Donner, A., Ippolito, J.A., Williams, T., 1999. SELEX and missing phosphate contact analyses reveal flexibility within the AP-2[alpha] protein: DNA binding complex. Nucleic Acids Res 27, 2760-2769.

Mootha, V.K., Lindgren, C.M., Eriksson, K.F., Subramanian, A., Sihag, S., Lehar, J., Puigserver, P., Carlsson, E., Ridderstrale, M., Laurila, E., Houstis, N., Daly, M.J., Patterson, N., Mesirov, J.P., Golub, T.R., Tamayo, P., Spiegelman, B., Lander, E.S., Hirschhorn, J.N., Altshuler, D.,

Groop, L.C., 2003. PGC-1alpha-responsive genes involved in oxidative phosphorylation are coordinately downregulated in human diabetes. Nat Genet 34, 267-273.

O'Brien, E.K., d'Alencon, C., Bonde, G., Li, W., Schoenebeck, J., Allende, M.L., Gelb, B.D., Yelon, D., Eisen, J.S., Cornell, R.A., 2004. Transcription factor Ap-2alpha is necessary for development of embryonic melanophores, autonomic neurons and pharyngeal skeleton in zebrafish. Dev Biol 265, 246-261.

Pabst, O., Rummelies, J., Winter, B., Arnold, H.H., 2003. Targeted disruption of the homeobox gene Nkx2.9 reveals a role in development of the spinal accessory nerve. Development 130, 1193-1202.

Parada, C., Chai, Y., 2015. Mandible and Tongue Development. Current Topics in Developmental Biology 115, 31-58.

Pertea, M., Kim, D., Pertea, G.M., Leek, J.T., Salzberg, S.L., 2016. Transcript-level expression analysis of RNA-seq experiments with HISAT, StringTie and Ballgown. Nat Protoc 11, 1650-1667.

Prescott, S.L., Srinivasan, R., Marchetto, M.C., Grishina, I., Narvaiza, I., Selleri, L., Gage, F.H., Swigut, T., Wysocka, J., 2015. Enhancer divergence and cis-regulatory evolution in the human and chimp neural crest. Cell 163, 68-83.

Qiu, M., Bulfone, A., Ghattas, I., Meneses, J.J., Christensen, L., Sharpe, P.T., Presley, R., Pedersen, R.A., Rubenstein, J.L., 1997. Role of the Dlx homeobox genes in proximodistal patterning of the branchial arches: mutations of Dlx-1, Dlx-2, and Dlx-1 and -2 alter morphogenesis of proximal skeletal and soft tissue structures derived from the first and second arches. Dev Biol 185, 165-184.

Qiu, M., Bulfone, A., Martinez, S., Meneses, J.J., Shimamura, K., Pedersen, R.A., Rubenstein, J.L., 1995. Null mutation of Dlx-2 results in abnormal morphogenesis of proximal first and second branchial arch derivatives and abnormal differentiation in the forebrain. Genes Dev 9, 2523-2538.

Rada-Iglesias, A., Bajpai, R., Prescott, S., Brugmann, S.A., Swigut, T., Wysocka, J., 2012. Epigenomic annotation of enhancers predicts transcriptional regulators of human neural crest. Cell Stem Cell 11, 633-648.

Rada-Iglesias, A., Prescott, S.L., Wysocka, J., 2013. Human genetic variation within neural crest enhancers: molecular and phenotypic implications. Philos Trans R Soc Lond B Biol Sci 368, 20120360.

Riddiford, N., Schlosser, G., 2016. Dissecting the pre-placodal transcriptome to reveal presumptive direct targets of Six1 and Eya1 in cranial placodes. Elife 5.

Rivera-Perez, J.A., Mallo, M., Gendron-Maguire, M., Gridley, T., Behringer, R.R., 1995. Goosecoid is not an essential component of the mouse gastrula organizer but is required for craniofacial and rib development. Development 121, 3005-3012.

Satoda, M., Zhao, F., Diaz, G.A., Burn, J., Goodship, J., Davidson, H.R., Pierpont, M.E., Gelb, B.D., 2000. Mutations in TFAP2B cause Char syndrome, a familial form of patent ductus arteriosus. Nat Genet 25, 42-46.

Schmidt, M., Huber, L., Majdazari, A., Schutz, G., Williams, T., Rohrer, H., 2011. The transcription factors AP-2beta and AP-2alpha are required for survival of sympathetic progenitors and differentiated sympathetic neurons. Dev Biol 355, 89-100.

Schorle, H., Meier, P., Buchert, M., Jaenisch, R., Mitchell, P.J., 1996. Transcription factor AP-2 essential for cranial closure and craniofacial development. Nature 381, 235-238.

Seberg, H.E., Van Otterloo, E., Loftus, S.K., Liu, H., Bonde, G., Sompallae, R., Gildea, D.E., Santana, J.F., Manak, J.R., Pavan, W.J., Williams, T., Cornell, R.A., 2017. TFAP2 paralogs regulate melanocyte differentiation in parallel with MITF. PLoS Genet 13, e1006636.

Shen, H., Wilke, T., Ashique, A.M., Narvey, M., Zerucha, T., Savino, E., Williams, T., Richman, J.M., 1997. Chicken transcription factor AP-2: cloning, expression and its role in outgrowth of facial prominences and limb buds. Dev Biol 188, 248-266.

Simmons, O., Bolanis, E.M., Wang, J., Conway, S.J., 2014. In situ hybridization (both radioactive and nonradioactive) and spatiotemporal gene expression analysis. Methods Mol Biol 1194, 225-244.

Simoes-Costa, M., Bronner, M.E., 2015. Establishing neural crest identity: a gene regulatory recipe. Development 142, 242-257.

Simoes-Costa, M., Bronner, M.E., 2016. Reprogramming of avian neural crest axial identity and cell fate. Science 352, 1570-1573.

Soriano, P., 1999. Generalized lacZ expression with the ROSA26 Cre reporter strain. Nat Genet 21, 70-71.

Sperber, S.M., Dawid, I.B., 2008. barx1 is necessary for ectomesenchyme proliferation and osteochondroprogenitor condensation in the zebrafish pharyngeal arches. Dev Biol 321, 101-110.

Subramanian, A., Tamayo, P., Mootha, V.K., Mukherjee, S., Ebert, B.L., Gillette, M.A., Paulovich, A., Pomeroy, S.L., Golub, T.R., Lander, E.S., Mesirov, J.P., 2005. Gene set enrichment analysis: a knowledge-based approach for interpreting genome-wide expression profiles. Proc Natl Acad Sci U S A 102, 15545-15550.

Tavares, A.L.P., Cox, T.C., Maxson, R.M., Ford, H.L., Clouthier, D.E., 2017. Negative regulation of endothelin signaling by SIX1 is required for proper maxillary development. Development 144, 2021-2031.

Trainor, P.A., 2014. Neural crest cells evolution, development, and disease. Elsevier/AP, Academic Press is an imprint of Elsevier, Amsterdam ; Boston, pp. xviii, 469 pages.

Trapnell, C., Hendrickson, D.G., Sauvageau, M., Goff, L., Rinn, J.L., Pachter, L., 2013. Differential analysis of gene regulation at transcript resolution with RNA-seq. Nat Biotechnol 31, 46-53.

Trapnell, C., Williams, B.A., Pertea, G., Mortazavi, A., Kwan, G., van Baren, M.J., Salzberg, S.L., Wold, B.J., Pachter, L., 2010. Transcript assembly and quantification by RNA-Seq reveals

unannotated transcripts and isoform switching during cell differentiation. Nat Biotechnol 28, 511-515.

Van Otterloo, E., Feng, W., Jones, K.L., Hynes, N.E., Clouthier, D.E., Niswander, L., Williams, T., 2016. MEMO1 drives cranial endochondral ossification and palatogenesis. Dev Biol 415, 278-295.

Van Otterloo, E., Li, W., Bonde, G., Day, K.M., Hsu, M.Y., Cornell, R.A., 2010. Differentiation of zebrafish melanophores depends on transcription factors AP2 alpha and AP2 epsilon. PLoS Genet 6, e1001122.

Wang, X., Pasolli, H.A., Williams, T., Fuchs, E., 2008. AP-2 factors act in concert with Notch to orchestrate terminal differentiation in skin epidermis. J Cell Biol 183, 37-48.

Williams, T., Tjian, R., 1991a. Analysis of the DNA-binding and activation properties of the human transcription factor AP-2. Genes Dev 5, 670-682.

Williams, T., Tjian, R., 1991b. Characterization of a dimerization motif in AP-2 and its function in heterologous DNA-binding proteins. Science 251, 1067-1071.

Wu, T.D., Nacu, S., 2010. Fast and SNP-tolerant detection of complex variants and splicing in short reads. Bioinformatics 26, 873-881.

Yamada, G., Mansouri, A., Torres, M., Stuart, E.T., Blum, M., Schultz, M., De Robertis, E.M., Gruss, P., 1995. Targeted mutation of the murine goosecoid gene results in craniofacial defects and neonatal death. Development 121, 2917-2922.

Yuan, J.S., Reed, A., Chen, F., Stewart, C.N., Jr., 2006. Statistical analysis of real-time PCR data. BMC Bioinformatics 7, 85.

Zhang, J., Hagopian-Donaldson, S., Serbedzija, G., Elsemore, J., Plehn-Dujowich, D., McMahon, A.P., Flavell, R.A., Williams, T., 1996. Neural tube, skeletal and body wall defects in mice lacking transcription factor AP-2. Nature 381, 238-241.

Zhao, F., Satoda, M., Licht, J.D., Hayashizaki, Y., Gelb, B.D., 2001. Cloning and characterization of a novel mouse AP-2 transcription factor, AP-2delta, with unique DNA binding and transactivation properties. J Biol Chem 276, 40755-40760.

Figures

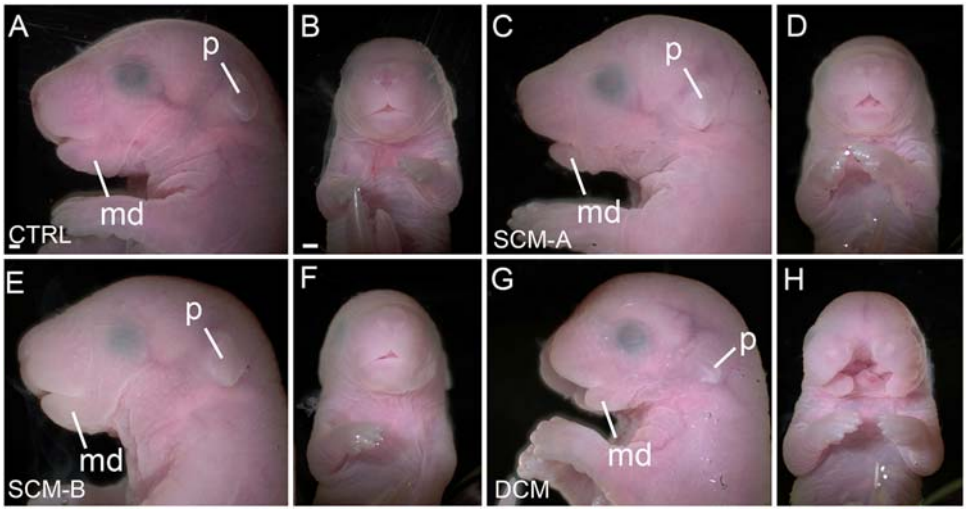

Figure 1 – *Tfap2a*/*Tfap2b* function cooperatively during craniofacial development. Gross morphology at E18.5 for the indicated genotype, in either lateral (**A, C, E, G**) or ventral (**B, D, F, H**) views. Abbreviations: md, mandible; p, pinna. Scale bars = 500μM.

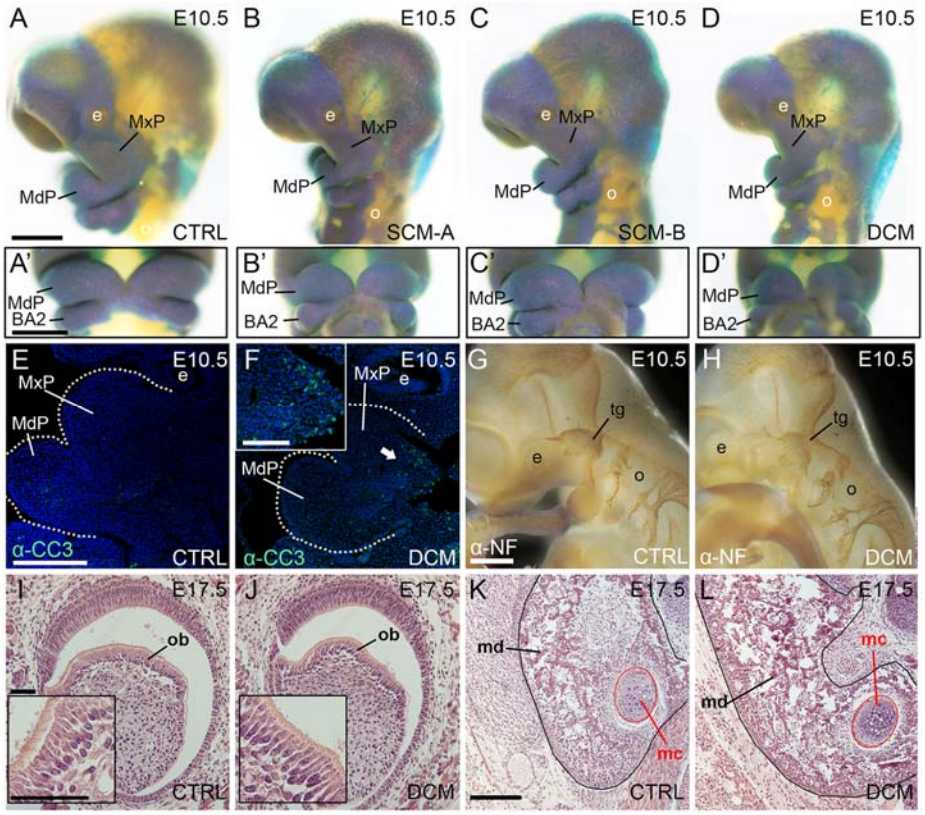

Figure 2 –*Tfap2a*/*Tfap2b*-*Wnt1*:CRE mutants display minor changes in NC development.

(**A-D**) Lateral (A-D) or ventral (A'-D') views of E10.5 *Wnt1:*CRE *R26 reporter*-allele for the indicated genotype with NCC lineages stained blue. (**E, F**) Immunofluorescent images of parasagittal paraffin sections through E10.5 BA1 of control (**E**) or DCM (**F**), labeling apoptotic cells with α-Cleaved Caspase 3 (CC3). Inset in (F) shows higher magnification of CC3 positive region (arrow). (**G, H**) Lateral views at E10.5 for the indicated genotype processed for α-neurofilament (α-NF) immunostaining, revealing cranial ganglia. (**I-L**) H&E stained, transverse sections, from control (**I, K**) or DCM (**J, L**) E17.5 lower-jaws, highlighting development of lower incisor odontoblasts (**I, J**), bone (mandible, md, black outline) and cartilage (Meckel's cartilage, mc, red outline) (**K, L**). Insets in (I, J) show columnar odontoblasts at higher magnification. Abbreviations: BA2, branchial arch 2; e, eye; MdP, mandibular prominence; MxP, maxillary prominence; o, otic vesicle; ob, odontoblasts; tg, trigeminal ganglion. Scale bars = 500μM; except I-L = 250μM; Inset in I = 100μM.

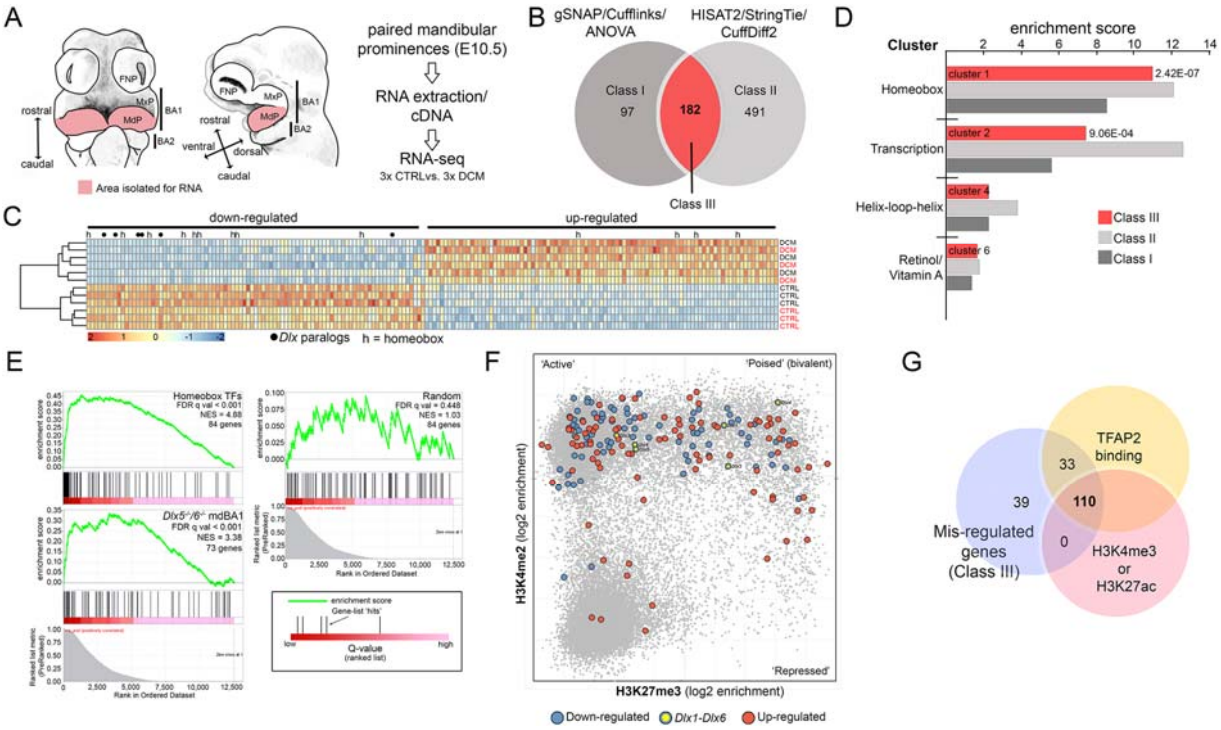

Figure 3 –*Tfap2a*/*Tfap2b*-*Wnt1*:CRE mutants exhibit altered expression of key homeobox genes in BA1. (**A**) Schematic of the RNA-seq procedure with the MdP region used for RNA-seq analysis highlighted (pink). (**B**) Venn diagram summarizing number of differentially expressed genes between DCMs and CTRLS. Class I and II gene-sets correspond to two independent bioinformatic pipelines, whereas Class III are genes identified in both datasets. (**C**) Heatmap of Class III gene-set generated from hierarchical clustering of individual expression values (pipeline 1 and 2, black and red text, respectively) with *Dlx* paralogs (black circles) and homeobox genes (h) highlighted. (**D**) Summary of pathway analysis of Class I - Class III gene-sets. Number to the right of the individual bars corresponds to FDR Q-value. (**E**) Gene set enrichment analysis of RNA-seq dataset utilizing gene-sets derived from: 1) homeobox TFs; 2) Genes significantly altered in the E10.5 *Dlx5/6*-null MdP (mdBA1) (Jeong et al., 2008); 3) Randomly generated dataset of 84 genes with expression in E10.5 BA1. (**F**) Scatterplot regenerated from (Minoux et al., 2017) showing promoter-specific (+/- 1Kb) fold-enrichment of

H3K4me2 (Y-axis) or H3K27me3 (X-axis) in E10.5 mandibular NCCs (grey). Genes from our class III dataset are shown – *Dlx* paralogs (yellow), additional down-regulated (blue), or upregulated (red). The upper left and right quadrants represent histone marks typical of active or poised promoters, respectively. (**G**) Venn diagram summarizing the intersection of the Class III dataset (lilac) with data from human induced NCCs (Rada-Iglesias et al., 2012) for direct AP-2 binding (yellow), and active histone marks (pink).

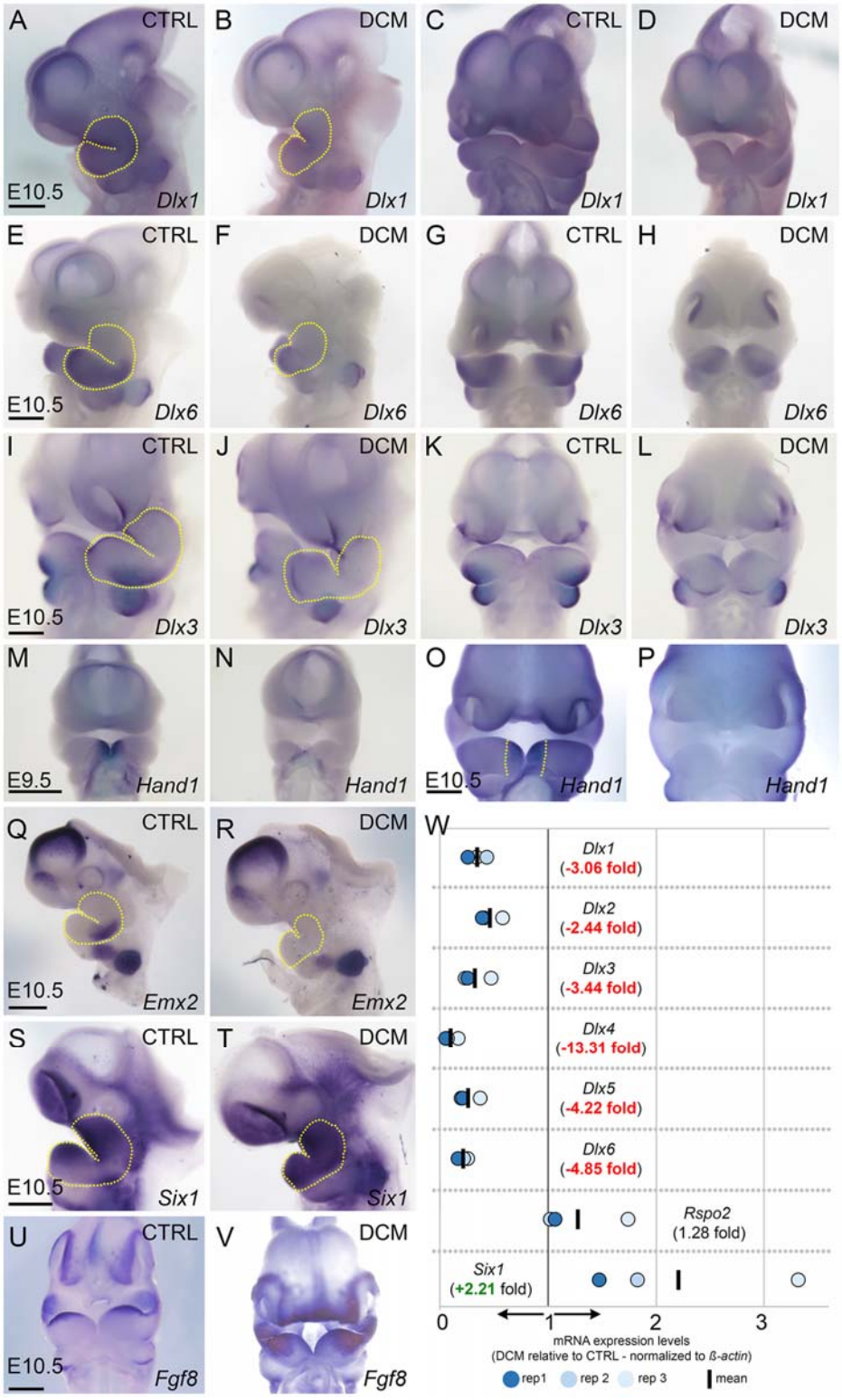

Figure 4 – Spatial and temporal gene expression changes in *Tfap2a*/*Tfap2b*-*Wnt1*:CRE mutants.

(**A-V**) Whole-mount *in situ* hybridization with indicated riboprobes at E10.5 (**A-L, O-V**) or E9.5 (**M, N**) shown in lateral (**A, B, E, F, I, J, Q-T**) or ventral (**C, D, G, H, K-P, U, V**) views. Yellow dashed lines outline BA1 in lateral views or in (**O**) demarcate lateral margins of *Hand1* expression. (**W**) Summary of qRT-PCR data using E9.5 BA1 mRNA comparing control and DCM embryos. X-axis displays relative expression levels (1 = no change). Mean fold change (red), triplicates (blue circles), and the mean (black bar) are shown for each gene. Scale bars = 500μM

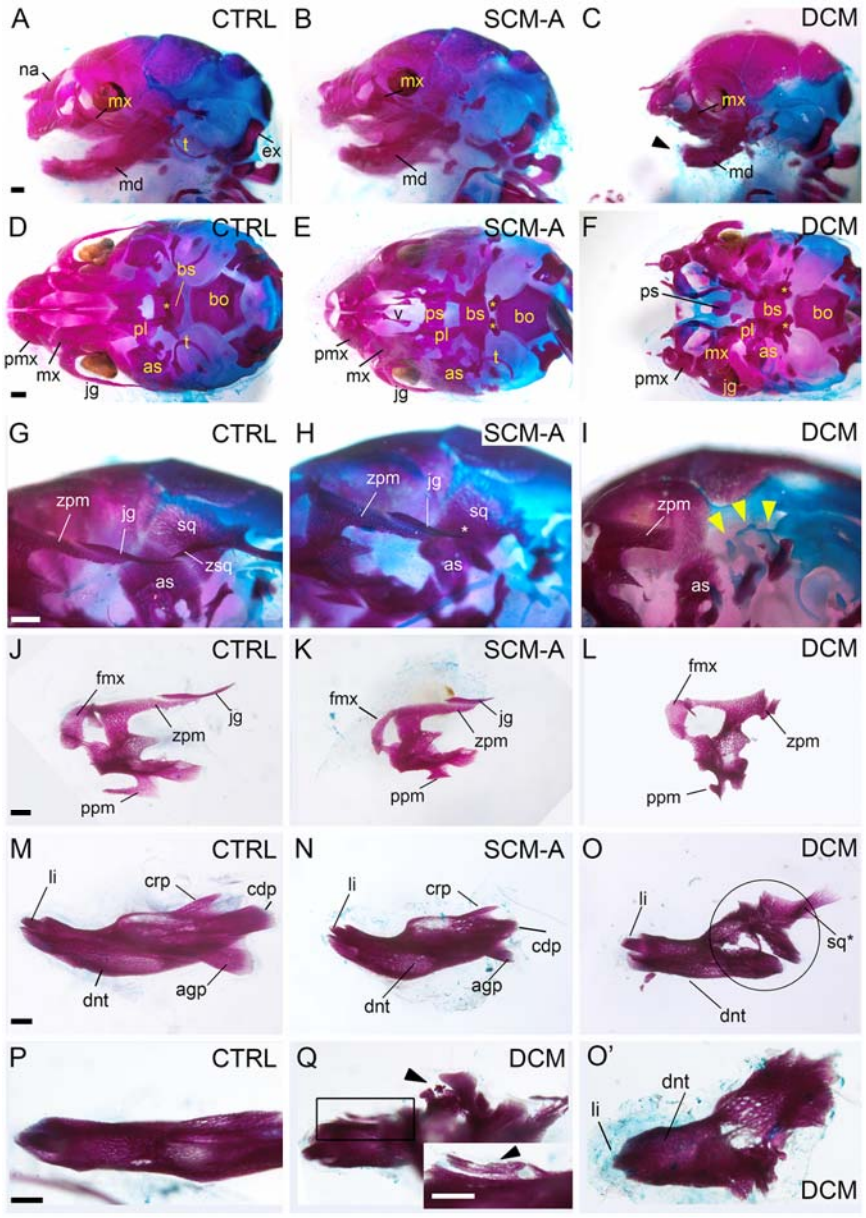

Figure 5 – *Tfap2a*/*Tfap2b*-*Wnt1*:CRE mandible, maxilla, and zygomatic arch defects overlap with *Dlx* loss-of-function mutants. (**A-I**) E18.5 skeletal preparations of the indicated genotypes, anterior to the left. (**A-C**) are lateral views, (**D-F**) are ventral views, and (**G-I**) are lateroventral views of the zygomatic arch. The jaw was removed in (**D-I**) to visualize the underlying skeleton. The truncated mandible (arrowhead, **C**), hyoid (asterisk(s), **D-F**), the missing zygomatic process of the squamosal (asterisk, H), and ectopic/unidentifiable cartilage

and bony elements (arrowheads, **I**) are indicated. (**J-L**) Ventral view of isolated maxillary bone. (**M-O, O'**) Lateral view of isolated dentary bone with circle (O) highlighting ectopic fusion of mandible to 'upper-jaw' elements including a presumed squamosal bone (sq*). (**P, Q**) Dorsal view of isolated mandibles (anterior left, medial up) of control (**P**) or DCM (**Q**). Arrowheads in **Q** highlight ectopic, orally projecting, ossifications in DCM mandibles. The inset in Q is an enlarged view of the boxed region. Abbreviations: agp, angular process; as, alisphenoid; bo, basioccipital; bs, basisphenoid; cdp, condylar process; crp, coronoid process; dnt, dentary; ex, exoccipital; fmx, frontal process of the maxillary; jg, jugal; li, lower incisor; md, mandible; mx, maxillary; na, nasal bone; pl, palatine; pmx, premaxillary; ppm, palatal process of the maxillary; ps, presphenoid; sq, squamosal; t, tympanic; zpm, zygomatic process of the maxillary; zsq, zygomatic process of the squamosal. Scale bars = 500μM.

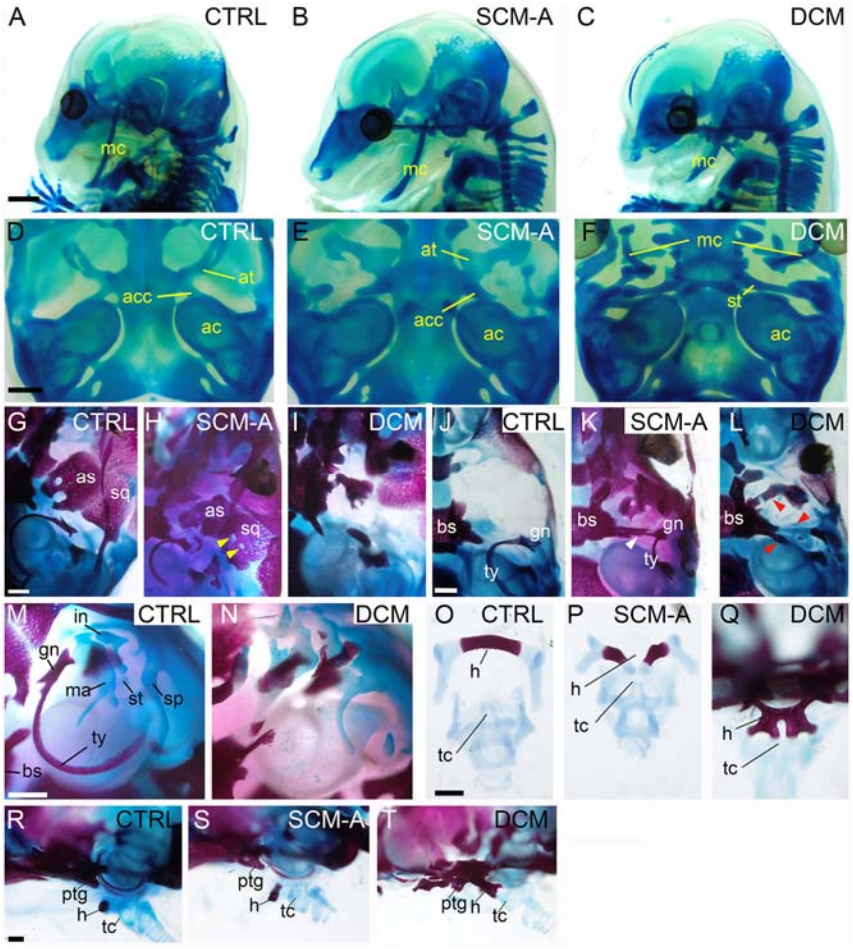

Figure 6 – *Tfap2a*/*Tfap2b*-*Wnt1*:CRE cranial wall and cranial base defects overlap with *Dlx* loss-of-function mutants

E15.5 chondrocranial (**A-F**) or E18.5 skeletal (**G-T**) preparations of the indicated genotypes. (**A-C**) are shown in lateral view, anterior to the left, and (**D-N**) are shown in ventral view, with the anterior medial aspect at the top middle (**D-F**) or top left (**G-N**). Panels (**O-T**) show ventral (**O-Q**) or lateral (**R-T**) views of the hyoid bone and thyroid cartilage, either attached to the cranium (**Q, R-T**) or in isolation (**O, P**). The jaw was removed in (**D-T**) and the alisphenoid and palatal bones in (**J, K**) to visualize the underlying skeleton. Note the alisphenoid and palatal shelves were not removed in (L) as they are already hypoplastic in DCMs. Ectopic foramen in the squamosal bone of SCM-A skeletons (yellow arrowheads, **H**), single ectopic strut in SCM-A skeletons

(white arrowhead, **K**) and multiple ectopic struts in DCM skeletons (red arrowheads, **L**) are shown. Abbreviations: ac, auditory capsule; acc, alicochlear commissure; as, alisphenoid; at, ala temporalis; bs, basisphenoid; gn, gonial; h, hyoid; in, incus; ma, malleus; mc, Meckel's cartilage; ptg, pterygoid; sp, styloid process; sq, squamosal; st, stapes; tc, thyroid cartilage; ty, tympanic. Scale bars = 500μM.

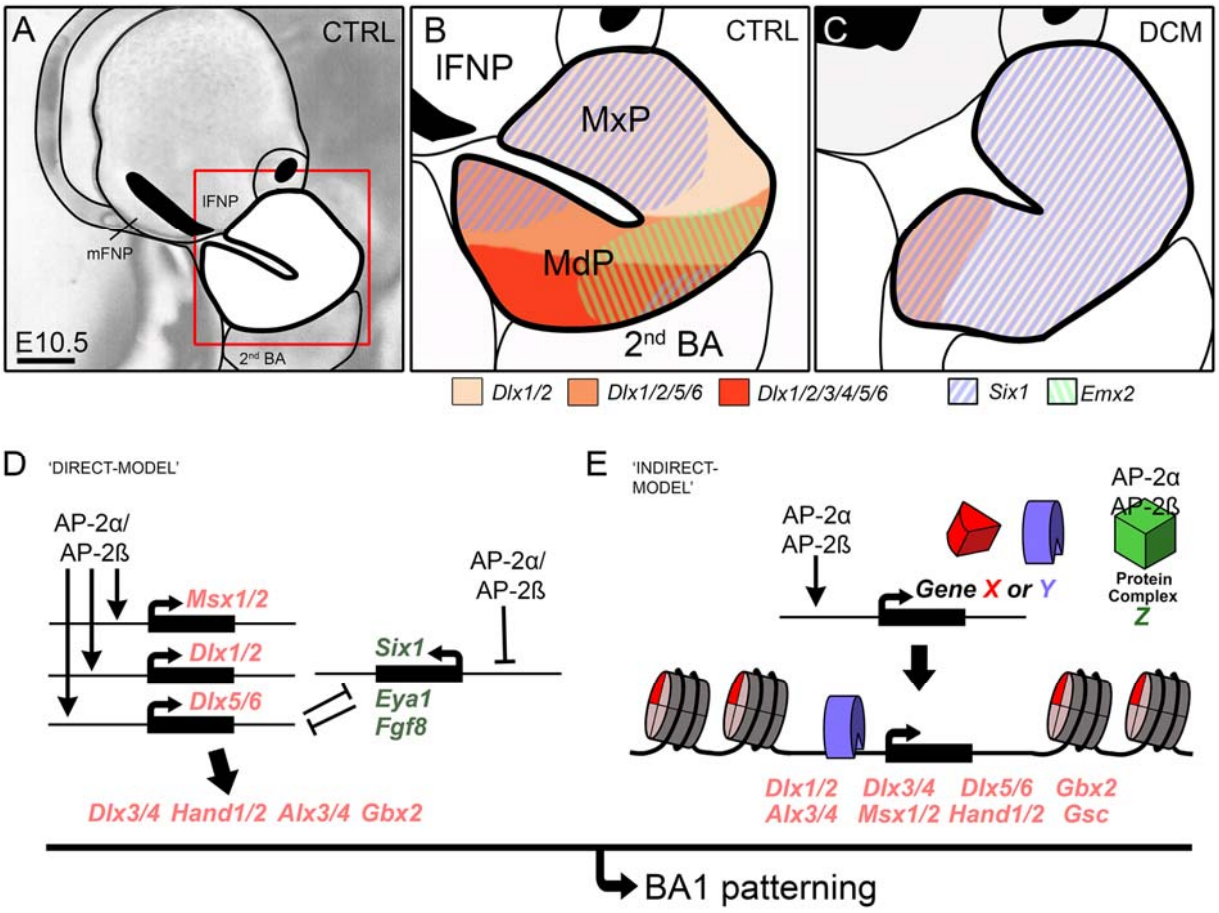

Figure 7 – AP-2α/ß function within BA1 NC. (**A-C**) Schematized lateral views of an E10.5 embryo, focusing on BA1. In (**A**) red square highlights BA1. (**B, C**) Diagrams of the region boxed in (**A**) in both control (**B**) and DCM (**C**) embryo, summarizing gene expression patterns assessed by *in situ* hybridization. (**D-E**) Potential models for how AP-2α/ß cooperatively regulate homeobox gene expression within BA1 NC, either directly (**D**) or indirectly (**E**) (see text for elaboration). Abbreviations: lFNP, lateral frontonasal prominence; MdP, mandibular prominence; mFNP, medial frontonasal prominence; MxP, maxillary prominence. Scale bar ~500μM.

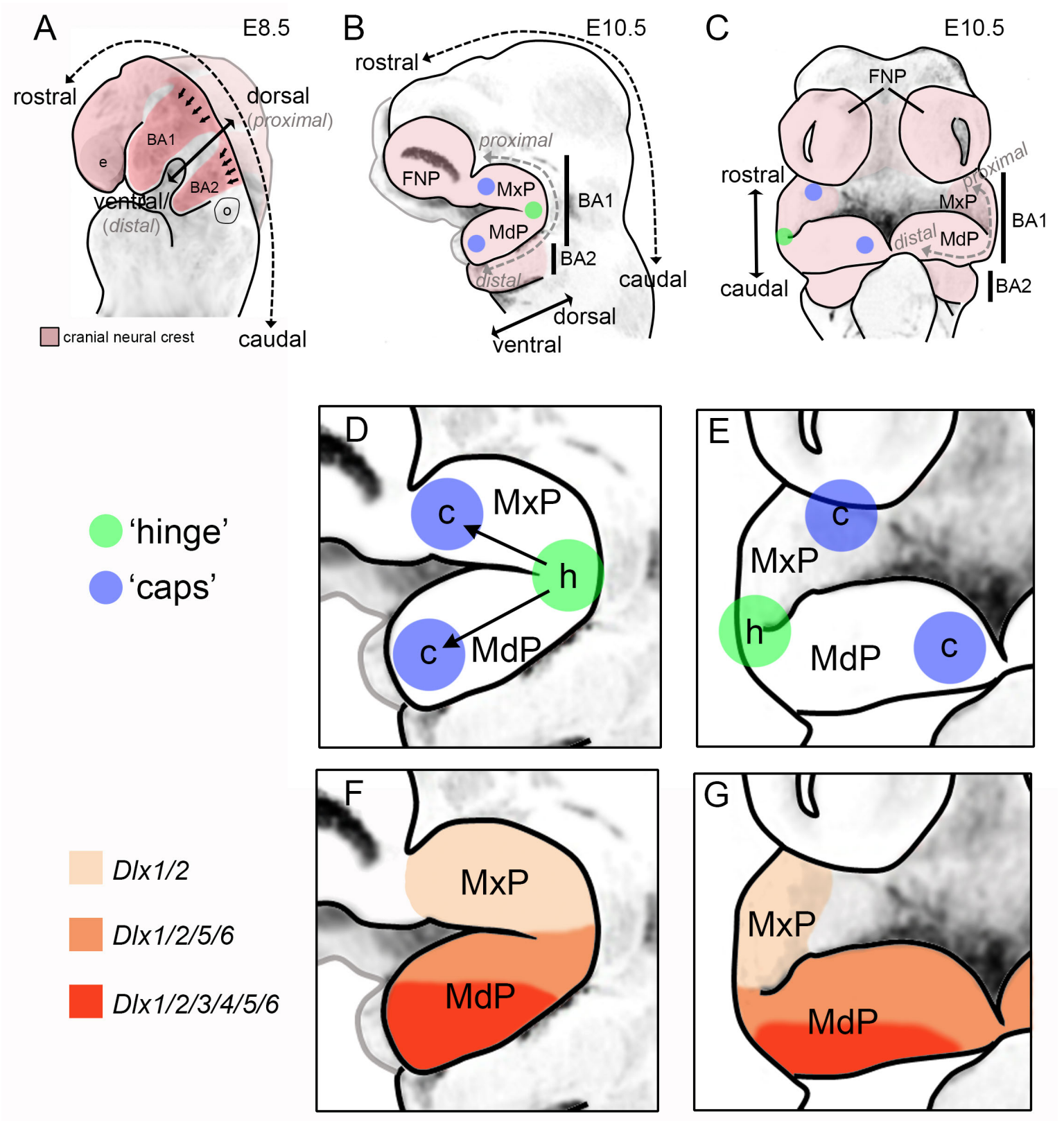
A
E8.5
rostral
dorsal
(proximal)
BA1
e
BA2
ventral/
(distal)
o
cranial neural crest
caudal
B
E10.5
rostral
proximal
FNP
MxP
BA1
MdP
BA2
distal
caudal
dorsal
ventral
C
E10.5
FNP
rostral
proximal
MxP
BA1
distal
MdP
caudal
BA2
'hinge'
'caps'
D
c
MxP
h
c
MdP
E
c
MxP
h
MdP
c
Dlx1/2
Dlx1/2/5/6
Dlx1/2/3/4/5/6
F
MxP
MdP
G
MxP
MdP

Figure S1 – Anatomical locations during mouse craniofacial development. (**A-G**) Dorsolateral (**A**), lateral (**B, D, F**), or ventral (**C, E, G**) schematics of an E8.5 (**A**) or E10.5 (**B-G**) mouse embryo, focusing on craniofacial regions and highlighting key anatomical axes and structures. (**A**) By E8.5, neural crest cells (red shading) that have originated from the dorsal neural tube of hind-, mid-, and forebrain regions are beginning to migrate ventrolaterally into the developing craniofacial structures (note, neural crest cells caudal to branchial arch 2 are not labeled). The dorsal-ventral (proximal-distal) axis of branchial arch 1 is less ambiguous at these earlier developmental stages. (**B, C**) By E10.5, NCCs (pink shading) have ceased migration, and have contributed to the majority of the craniofacial mesenchyme. Additionally, the first branchial arch has become further refined into maxillary (MxP) and mandibular (MdP) prominences – which will form components of the upper and lower jaw, respectively. Note, studies have indicated, at least in avian models, that the MxP may not be derived from NCCs of BA1 (Cerny et al., 2004; Lee et al., 2004). Nevertheless, subdivision of BA1 into these two prominences in mammals somewhat obfuscates anatomical orientations, but traditionally the MxP is referred to as dorsal/proximal and the MdP ventral/distal. BA1 can also be subdivided into the ‘hinge’ (green dot), that is the intersection of the MxP and MdP, and ‘caps’ (blue dots), that is, the regions furthest from the hinge in both the MxP and MdP (Depew and Compagnucci, 2008; Depew et al., 2002; Depew and Simpson, 2006; Depew et al., 2005). We primarily reference these latter terms when discussing BA1. Panels D and E show BA1 and relative positions of the proposed ‘hinge’ and ‘caps’ in more detail, whereas panels F and G highlight the ‘nested Dlx-code’ within the same region. Abbreviations: BA1, branchial arch 1 (i.e. mandibular arch); BA2, branchial arch 2 (i.e. hyoid arch); c, cap; e, eye; FNP, frontonasal prominence; h, hinge; MdP, mandibular prominence; MxP, maxillary prominence; o, otic vesicle.

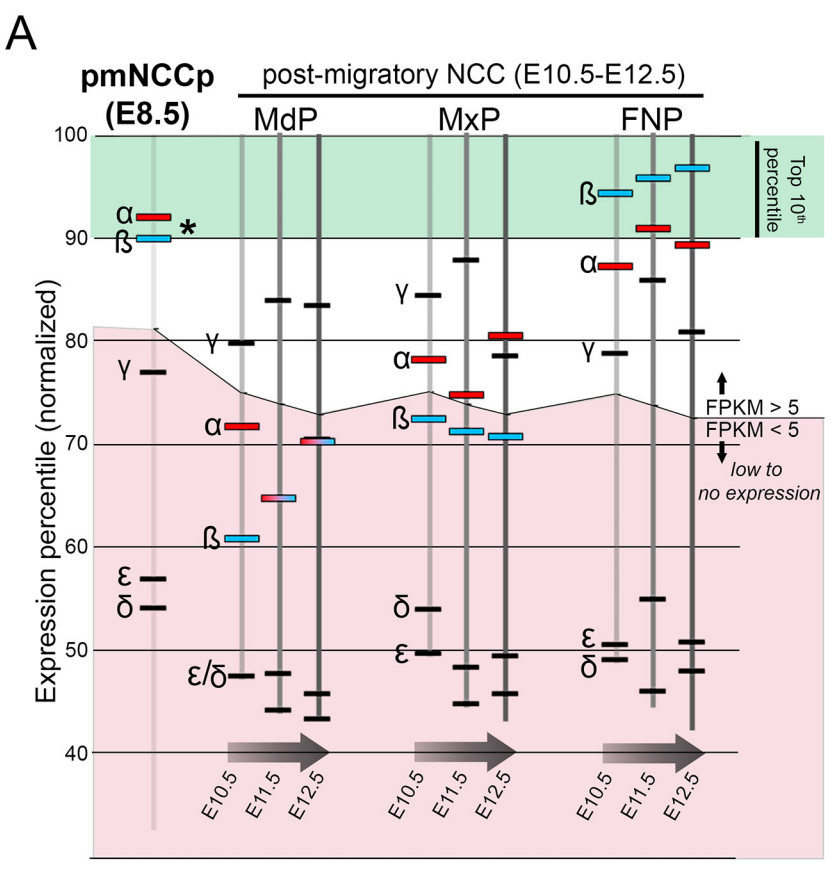

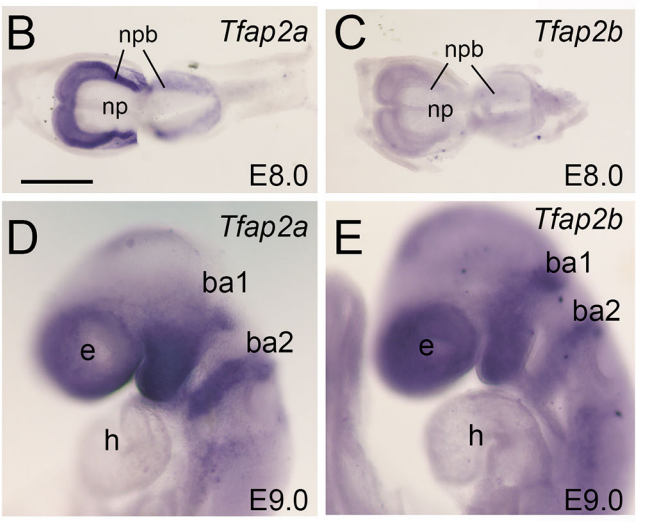

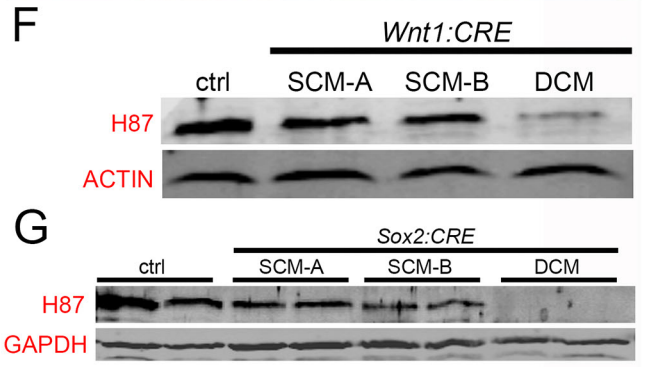

Figure S2 – *Tfap2a* and *Tfap2b* are the most highly expressed paralogs in early mouse cranial NC. (**A**) Chart depicting expression percentile of all genes (based on 'normalized FPKM rank') for E8.5 (Minoux et al., 2017), and E10.5-E12.5 cranial mesenchyme (Hong Li, manuscript in prep, data available at Facebase) – essentially ranking gene expression levels across the entire RNAseq dataset (90-100 on Y-axis, highlighted green, corresponds to the top 10th percentile of expressed genes within a dataset). Ranked position of *Tfap2a* (red bar with label 'α') and *Tfap2b* (blue bar with label 'ß'), as well as other *Tfap2* paralogs (black bars, *Tfap2c* = γ, *Tfap2d* = δ, and *Tfap2e* = ε) are indicated within each dataset. Note, the percentile corresponding to an FPKM of 5 is highlighted in each dataset with genes ranked below this line shown in pink, corresponding to very low or essentially non-expressed genes. (**B-E**) Images of whole-mount *in situ* hybridization of E8.0 dorsal view (**B, C**) or E9.0 lateral view (**D, E**) wild-type embryos, processed with a *Tfap2a* (**B, D**) or *Tfap2b* (**C, E**) antisense riboprobe. (**F**) Collective AP-2α and AP-2ß protein expression levels (as detected by H-87 antibody) in E10.5 facial prominence tissue isolated from the indicated genotypes. ACTIN serves as a loading control. Residual AP-2 immunoreactivity in DCMs represents expression in the ectoderm, which is not targeted by *Wnt1:*CRE. (**G**) Same as in (**F**) with the exception that protein was isolated from E12.5 *Sox2:*CRE embryos of the indicated genotype. GAPDH serves as the loading control. Note, *Sox2:*CRE will target AP-2 expression in both the ectoderm and neural crest derived tissues. Note, for **F** and **G**, each lane corresponds to protein isolated from a single embryo. Abbreviations: ba1, branchial arch 1; ba2, branchial arch 2; FNP, nasal prominence; h, heart; MdP, mandibular prominence; MxP, maxillary prominence; np, neural plate; npb, neural plate border; pmNCCp, premigratory cranial neural crest precursors; Scale bars = 500µM.

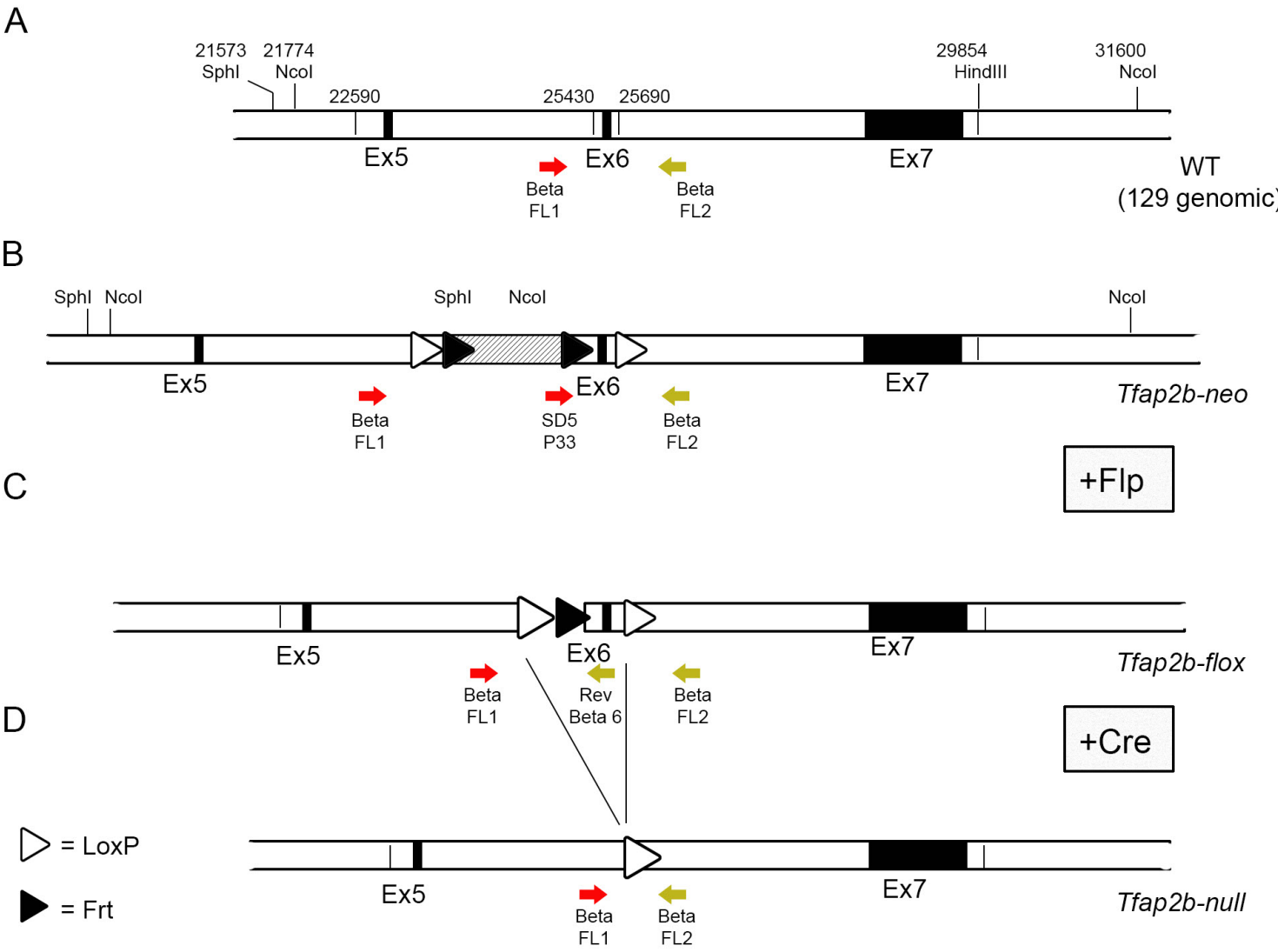

Figure S3 – Schematic of *Tfap2b* alleles generated and utilized in this study. (**A**) Diagram of endogenous *Tfap2b* genomic locus, focused on regions corresponding to exons 5, 6 and 7 (black boxes). Relative genomic positions, including selected restriction sites, are indicated. (**B**) Layout of locus (*Tfap2b-neo*) after targeted homologous recombination, with *neomycin* selection cassette still present (hashed box) and incorporated *LoxP* and *Frt* sites near exon 6. (**C**) Graphic representation of modified *Tfap2b* allele following FLP-mediated recombination resulting in the removal of the *neomycin* cassette and generation of a *Tfap2b* conditional allele (*Tfap2b-flox*). This allele contains *LoxP* recombination sites flanking exon 6 of *Tfap2b*. (**D**) *Tfap2b* locus following CRE-mediated recombination (*Tfap2b*-null). Excision of exon 6 of *Tfap2b* results in a functional null allele in the CRE-recombinase expressing cells/tissues and their derivatives. Colored arrows show positions of primers used for PCR genotyping.

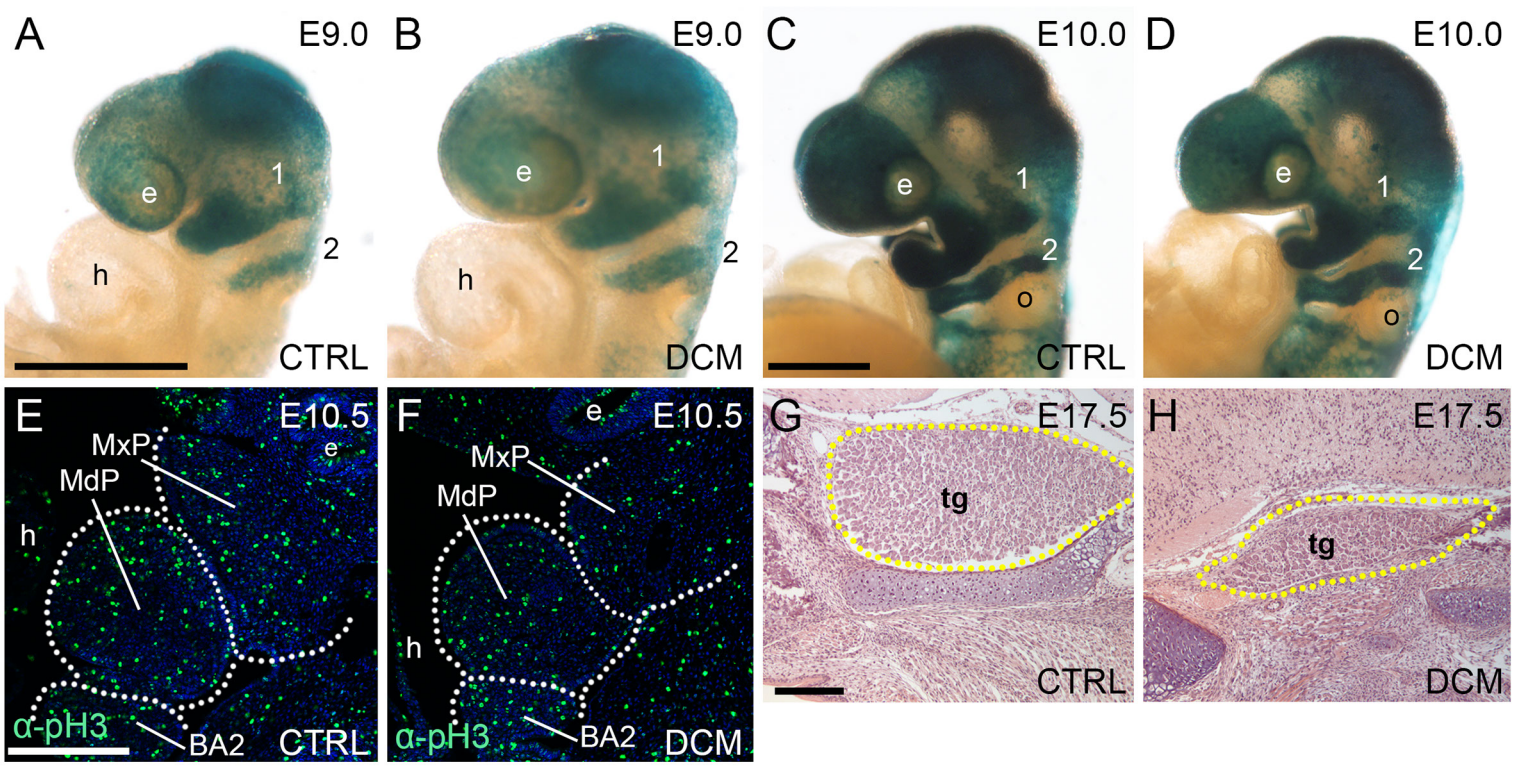

Figure S4 – NC development in *Tfap2a*/*Tfap2b*-*Wnt1*:CRE mutants. (**A-D**) Lateral views of E9.0 (**A, B**) and E10.0 (**C, D**) *Wnt1:*CRE *R26 reporter* embryos, of the indicated genotype processed for ß-galactosidase staining to label NCC lineages. 1 and 2 corresponds to BA1 and BA2 NCC streams, respectively. (**E, F**) Anti-α-phospho-Histone H3 immunofluorescent stained parasagittal paraffin sections through BA1 and BA2 of a control (**E**) or DCM (**F**) E10.5 embryo to label proliferative cells. (**G, H**) H&E stained frontal sections from E17.5 embryos of the indicated genotype, with the trigeminal ganglia outlined by the yellow dashed lines. Abbreviations: BA2, branchial arch 2; e, eye; h, heart; MdP, mandibular prominence; MxP, maxillary prominence; o, otic vesicle; tg, trigeminal ganglion. Scale bars = 500µM.

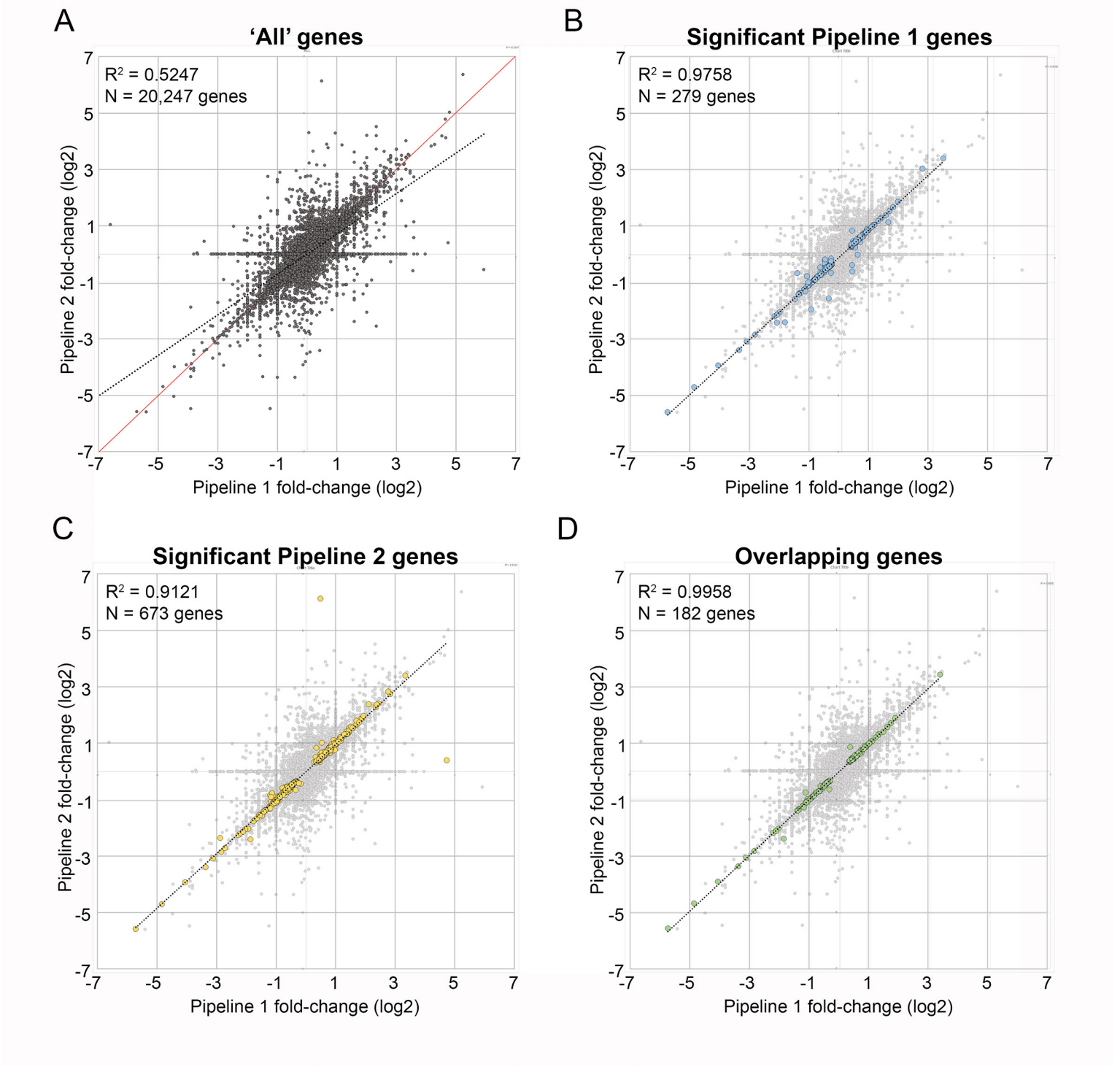

Figure S5 – Comparison of gene expression values between bioinformatic pipelines. (**A-D**) Scatterplots displaying calculated fold-change values (control versus *Tfap2a/Tfap2b-Wnt1*:CRE mutants, log2 scale) between 'Pipeline 1' (X-axis) and 'Pipeline 2' (Y-axis). For **A-D** the calculated R^2-value (correlation coefficient) and number (N) of genes analyzed is reported in the top left corner. For **B-D**, the 'All' gene dataset from panel A is displayed as a light gray graph underneath. **A**) Analysis of all genes. **B**) Analysis of genes only called significant in Pipeline 1 (Class I genes). **C**) Analysis of genes only called significant in Pipeline 2 (Class II genes). **D**) Analysis of overlapping genes between both Class I and II datasets (i.e. Class III genes).

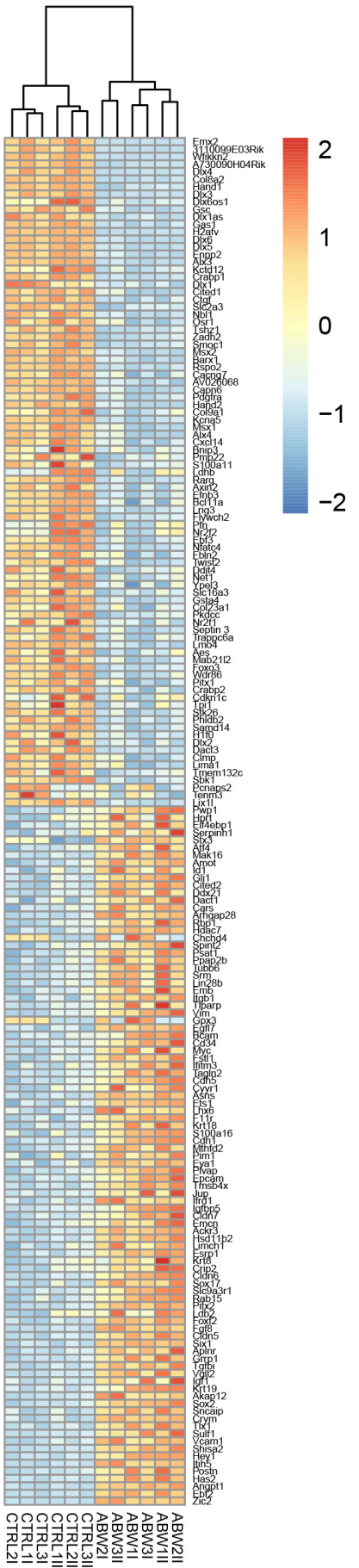
2
1
0
−1
−2
Emx2
9130009E03Rik
Wtkkh2
A730090H04Rik
Dlk4
Col8a2
Hand1
Dlk3
Dlx6os1
Gsc
Dlx1as
Gas7
H2afv
Dlx6
Dlx5
Cmpx2
Alx3
Kctd12
Crabp1
Dlx1
Cited1
Cfdl
Slc2a3
Nbl1
Osr1
Ythdc1
Zadh2
Smoc1
Msx2
Barx1
Rspo2
Cacng7
AV028068
Capn6
Pdgfra
Hand2
Col9a1
Kcna5
Msx1
Alx4
Cxcl14
Bnip3
Tmbp22
S100a11
Ldhb
Rarg
Axin2
Emb3
Bcl11a
Lrig3
Tmwch2
Ptn
Nr2f2
Ebf3
Nfatc4
Cbln2
Twist2
Ddit4
Ndt1
Xpel3
Slc16a3
Gsta4
Col23a1
Pkdcc
Nr2f1
Septin 3
Trappc6a
Lmo4
Aes
Mab21l2
Foxo3
Wdr86
Pitx1
Crabp2
Cdkn1c
Tpt1
Slk26
Phldb2
Samd14
Ttbk1
Dlx2
Dact3
Clmp
Lima1
1700009P17Rik
Tmem132c
Sbk1
Pcnags2
Tenm3
Lix1l
Pwp1
Hpn
Eif4ebp1
Serpinh1
Sfx3
Atf4
Mak16
Amot
Id1
Gli1
Clec14a
Ddx21
Dact1
Cars
Arhgap28
Rbp1
Hdac7
Chchd4
Sbno2
Csat1
Ppap2b
Tubb6
Srrt
Lin28b
Emb
Itgb1
Tjparp
Vim
Gpx3
Epas1
Pecam
Cd34
Myc
Fstl1
Ifitm3
Tagln2
Cdh5
Cyyr1
Kdr
Ets1
Dlx6
F11r
Krt18
S100a16
Cdh1
Mthfd2
Tpm1
Eya1
Flvcr1
Epcam
Tmsb4x
Utp3
Ifrd1
Igfbp5
Cldn7
Emcn
Akr1c18
Hsd11b2
Limch1
Espn1
Krt8
Cnn2
Cldn6
Sox17
Slc9a3r1
Rab15
Ptk2
Ldb2
Foxf2
Eqtn
Cldn5
Six1
Apln
Grrp1
Tgfbi
Vgll2
Igf1
Krt19
Akap12
Sox2
Sncaip
Crym
Tbx1
Sulf1
Vcam1
Shisa2
Hey1
Ephb1
Postn
Has2
Angpt1
Ebf2
Zic2
CTRL2I
CTRL1I
CTRL3I
CTRL1II
CTRL2II
CTRL3II
ABW2I
ABW3II
ABW1I
ABW3I
ABW1II
ABW2II

Figure S6 – Detailed hierarchical clustering of 182 ‘high-confidence’ gene-set in *Tfap2a*/*Tfap2b*-*Wnt1*:CRE mutants versus controls. ABW indicates the DCM samples, whereas CTRL are the controls. 1, 2, 3 indicates the biological replicate, and I and II corresponds to data from pipeline 1 or 2, respectively.

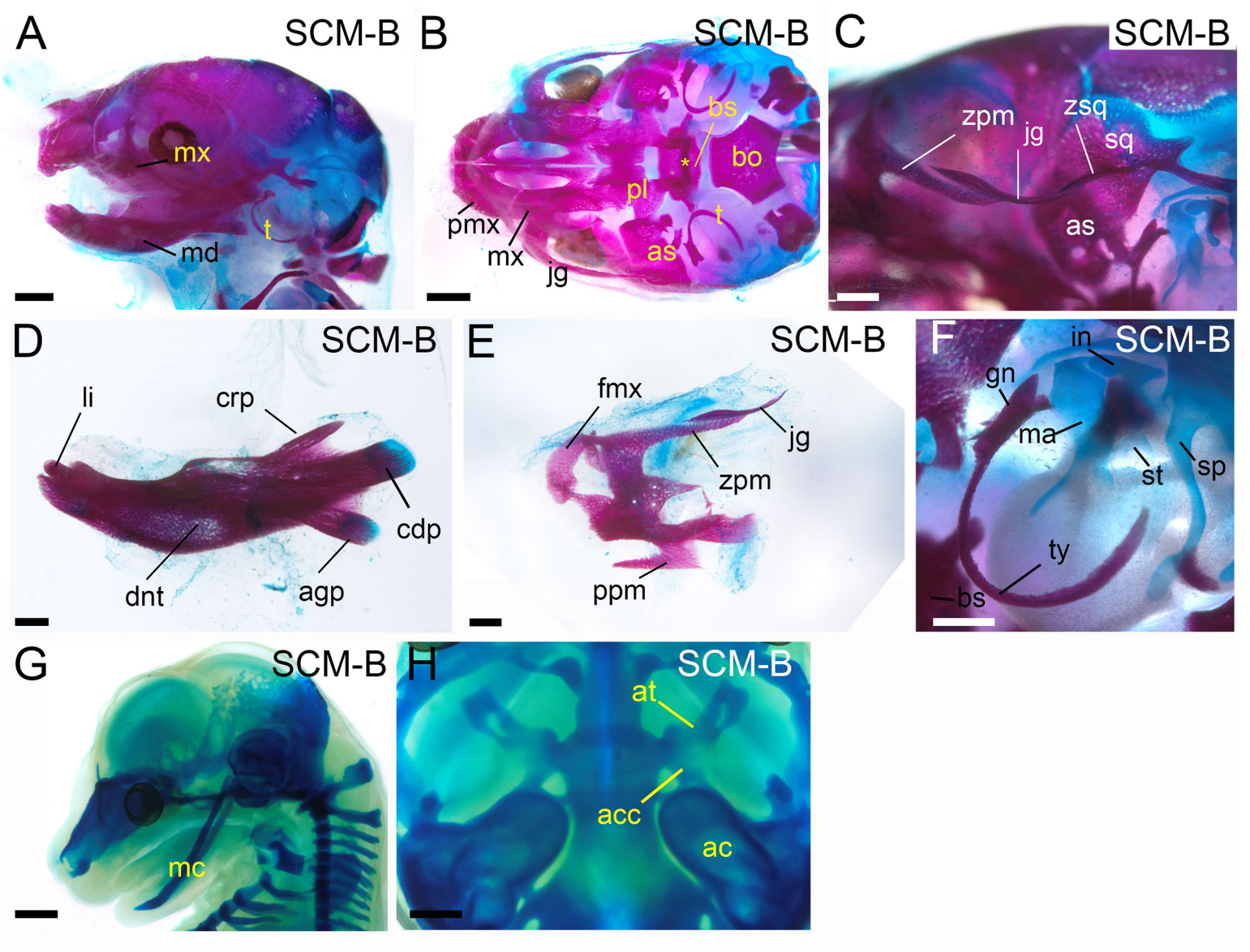

Figure S7 – SCM-B skeletal images. E18.5 skeletal (**A-F**) or E15.5 chondrocranial (**G, H**) preparations. (**A-C**) Whole cranial skeletal preparations in lateral (**A**), ventral (**B**) or ventrolateral (**C**) views, anterior to the left. Note, the mandible has been removed for better visualization in panels B and C, and panel C is a higher magnification image of the zygomatic arch. The asterisk in B highlights the hyoid bone. Mandibular (**D**) or maxillary (**E**) bone shown in isolation, anterior to the left. (**F**) Ventral view, anterior to the upper-left, focusing on the middle ear ossicles. Lateral, anterior left, (**G**) or ventral, anterior up, (**H**) views of the chondrocranium. Compare images to control, SCM-A, and DCM preparations in Figures 5 and 6. Note, SCM-B skeletons resemble controls except for the ~20% that had a cleft secondary palate, and these mutants had palatal process defects typical of this pathology. Abbreviations: ac, auditory capsule; acc, alicochlear commissure; agp, angular process; as, alisphenoid; at, ala temporalis; bo, basioccipital; bs, basisphenoid; cdp, condylar process; crp, coronoid process; dnt, dentary; fmx, frontal process of the maxillary; g, gonial; in, incus; jg, jugal; li, lower incisor; ma, malleus; mc, Meckel's cartilage; md, mandible; mx, maxillary; pl, palatine; pmx, premaxillary; ppm, palatal process of the maxillary; sp, styloid process; sq, squamosal; st, stapes; ty, tympanic; zpm, zygomatic process of the maxillary; zsq, zygomatic process of the squamosal. Scale bars = 1,000 µM (A, B, G), 500µM (C, D, E, F, H).

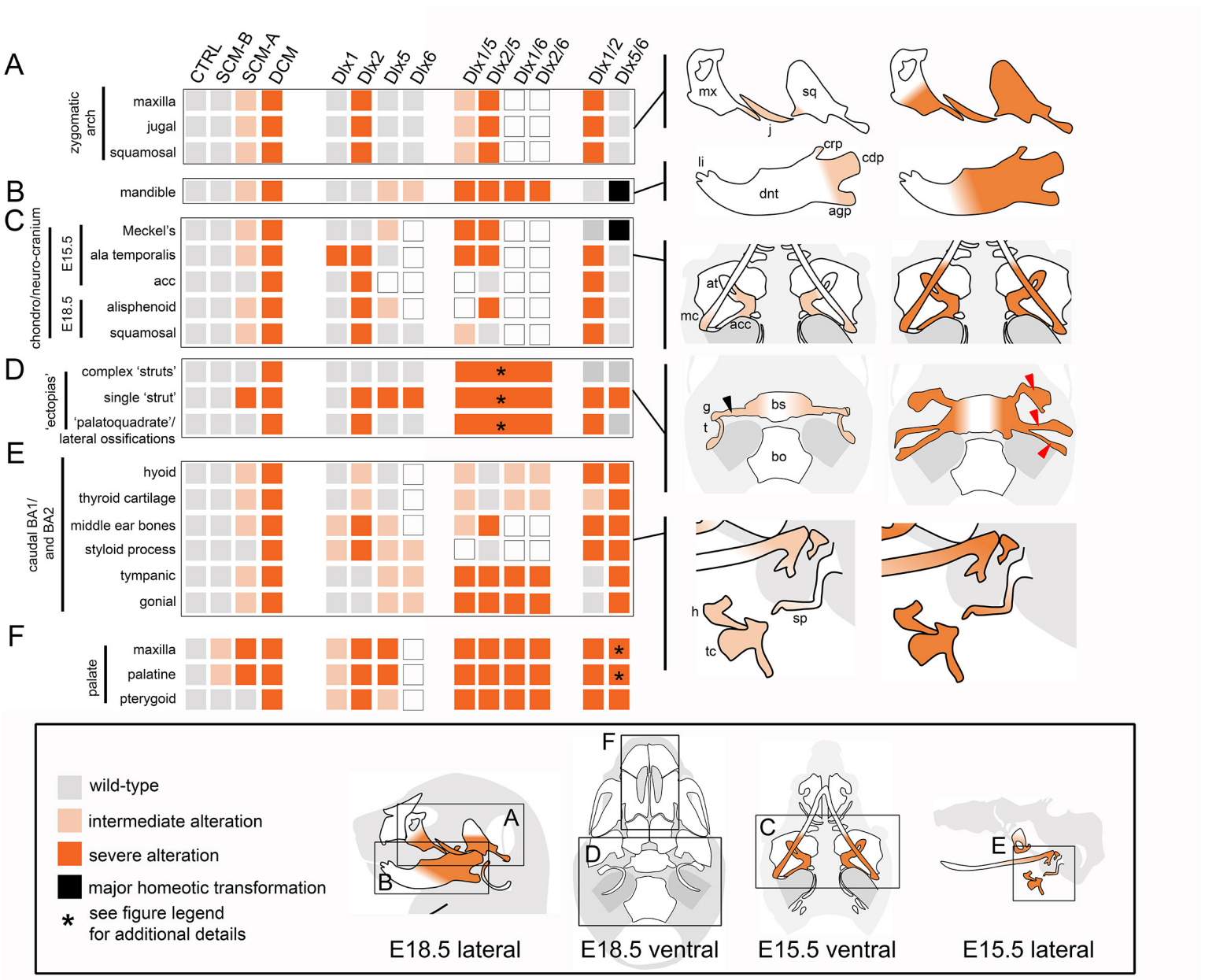

Fig. S8 Summary of overlaps between AP-2α/ß and *Dlx* mutant skeletal phenotypes.

Overview. A heat-map is shown on the left classifying the severity of defects associated with particular components of the craniofacial skeleton at both E15.5 and E18.5 for controls, *Wnt1*:Cre *Tfap2a/b* mutants (based on the images in Figures 5, 6, and S7), and data from the analysis of *Dlx* single and double mutants (1, 2, 5, 6). At the bottom of the figure is shown an overview of the E15.5 and E18.5 skeleton with boxes marking specific regions analyzed in A-F. On the right of the diagram are shown more detailed views of the structures under analysis. These are projected onto a wild-type skeleton, with the exception of the bones of (D) where the first and second columns represent the SCM-A and DCM phenotypes, respectively, and (F) which is not shown. Ectopic struts associated with the cranial base in (D) are shown by arrowheads. In general, grey boxes correspond to relatively wild-type skeletal elements, dark orange boxes represent elements with major developmental defects, whereas light orange represent partial or intermediate defects. Regions where an unshaded box is present represent mouse mutants for which no comment on severity is made. Black boxes indicate major homeotic transformations. Orange color-coding is also used in the schematics to illustrate the severity of the defects. Larger boxes indicate the complexity of *Dlx* allelic combinations that can generate variations of these ectopic skeletal processes. Although several *Dlx* examples are often listed as a reference to the associated defect, such a list is by no means comprehensive. Abbreviations: acc, alicochlear commissure; agp, angular process; at, ala temporalis; bs, basisphenoid; bo, basioccipital; cdp, condylar process; crp, coronoid process; dnt, dentary; g, gonial; h, hyoid; j, jugal; li; lower incisor; mc, Meckel's cartilage; mx, maxillary; sq, squamosal; sp, styloid process; t, tympanic; tc, thyroid cartilage.

(**A**) **Zygomatic arch** (ZGA): Defects in the ZGA range from mild (e.g. loss of the zygomatic process of the squamosal) to severe (more extensive ablations and truncations of the ZGA elements). The appearance of ectopic cartilage/bony elements of unknown lineage (referred to as 'palatoquadrate', discussed more below) are also included in this severe category. For example, SCM-A embryos show a loss of the zygomatic process of the squamosal, similar to [$Dlx1^{-/-};Dlx5^{-/-}$], [$Dlx2^{-/-};Dlx5^{+/-}$], or [$Dlx3^{+/-};Dlx5^{-/-}$] mutants [(Depew et al., 2005), Figure 14E, 13F, and 15F, respectively]. In contrast, DCM embryos display a near ablation of the ZGA (see text),

with an often thickened, truncated zygomatic process of the maxillary bone, as described for example, in *Dlx2*$^{-/-}$*;Dlx5*$^{-/-}$ mutants [(Depew et al., 2005), Figure 11G].

(**B**) **Mandible**: Regions of the mandible most susceptible to loss of AP-2 and Dlx paralogs include the proximal condyles. More mild defects include hypoplastic development of condylar processes, as seen in SCM-A skeletal preparations. Sensitivity of the proximal condyles is also noted in *Dlx5*$^{-/-}$ *and Dlx6*$^{-/-}$ single mutants [(Depew et al., 2005), Figure 7G; (Jeong et al., 2008), Figure 5F, G]. More extreme transformations of the mandible are observed in DCM embryos and are progressively more severe in various *Dlx* allelic combinations [(Jeong et al., 2008), Figure 6G-L; (Depew et al., 2005), Figure 18A-F and Figure 20C, D]. Eventually, in the context of the appropriate *Dlx* paralogs (e.g. *Dlx5*$^{-/-}$*;Dlx6*$^{-/-}$), a threshold is approximated in which the lower-jaw adopts an upper-jaw identity (Beverdam et al., 2002; Depew et al., 2002). Note, such complete transformation is not observed in DCM embryos, although such transformation is often associated with a cleft mandible, which is present in DCM embryos.

(**C**) **Chondro-/Neurocranium**. In respect to the chondrocranial elements, again, intermediate and more severe phenotypes are observed in both AP-2 and *Dlx* mutants. For example, both the upper-jaw ala temporalis and lower-jaw Meckel's cartilage are particularly sensitive to AP-2 and DLX levels. In the context of AP-2 this is observed by mild patterning defects in the ala temporalis of SCM-A embryos and near ablation in DCM embryos. Proximal loss of the ala temporalis was a notable consequence in *Dlx1*$^{-/-}$ [(Qiu et al., 1997), Figure 3B], *Dlx2*$^{-/-}$ [(Qiu et al., 1995), Figure 3B; (Qiu et al., 1997), Figure 2C] and *Dlx1*$^{-/-}$*;Dlx2*$^{-/-}$ [(Qiu et al., 1997), Figure 2D] mutants, with more intermediate defects noted in heterozygous embryos [(Depew et al., 2005), Figure 9F]. Another noted similarly was the loss of the alicochlear commissure in DCM embryos, which was often missing or affected in *Dlx2*$^{-/-}$ [(Qiu et al., 1995), Figure 3B], *Dlx1*$^{-/-}$*;Dlx2*$^{-/-}$ [(Qiu et al., 1997), Figure 2C, D], or more complex compound mutants [e.g. [*Dlx1*$^{+/-}$*;Dlx2*$^{+/-}$*;Dlx3*$^{+/-}$*;Dlx5*$^{+/-}$*;Dlx6*$^{+/-}$], (Depew et al., 2005), Figure 18F]. The lower-jaw, chondrocranial element, Meckel's cartilage, was again intermediately affected in SCM-A embryos (slightly

shorter, with a non-continuous connection with the malleus), whereas in DCM embryos such defects were more severe (see text). Similarly, various *Dlx* mutants display a range of Meckel's cartilage defects. Such defects often impact the proximal end of Meckel's, influencing its association with middle ear structures, such as seen in *Dlx5*$^{-/-}$ mutants [(Depew et al., 2005), Figure 7E). As with the mandible, Meckel's is eventually transformed into its upper-jaw-like counterpart, the ala temporalis in more extreme situations [i.e. *Dlx5*$^{-/-}$*;Dlx6*$^{-/-}$ mutants, (Beverdam et al., 2002; Depew et al., 2002)].

(**D**) **'Ectopias'**: Note, schematics shown in right hand side column 1 and 2 represent ventral views of the cranial base at E18.5 in mutant SCM-A and DCM embryos, respectively. One of the most striking similarities between the AP-2 and Dlx mutants is the appearance of various ectopic structures associated with the cranial base. For example, in SCM-A embryos a single ossified strut (black arrowhead) was observed projecting laterally from the medial basisphenoid, often interacting/fusing with the gonial bone. Several previous reports have identified a highly similar structure in various *Dlx* mutants, including *Dlx2*$^{-/-}$ [(Qiu et al., 1995), Figure 3B, F], *Dlx1*$^{-/-}$*;Dlx2*$^{-/-}$ [(Qiu et al., 1997), Figure 2G, H], *Dlx5*$^{-/-}$ [(Depew et al., 1999), Figure 6D, F, H; (Depew et al., 2005), Figure 19B], *Dlx6*$^{-/-}$ [(Jeong et al., 2008), Figure 6b], and corresponding *Dlx* allelic combinations [e.g. [*Dlx1*$^{-/-}$*;Dlx2*$^{-/-}$*;Dlx5*$^{-/-}$], (Depew et al., 2005), Figure 16B]. More complex ectopic elements (red arrowheads) are noted in DCM embryos, often containing ossified elements with apparent cartilaginous 'joints', a feature again observed in various *Dlx* compound mutants [e.g. *Dlx5*$^{-/-}$*;Dlx6*$^{+/-}$, (Depew et al., 2005), Figure 16C and [*Dlx1*$^{+/-}$*;Dlx2*$^{+/-}$*;Dlx5*$^{-/-}$*;Dlx6*$^{+/-}$] (Depew et al., 2005), Figure 20B]. Also, as briefly mentioned above, loss of the ZGA was often associated with the appearance of ectopic bone and cartilage elements on the lateral side-walls of the cranium, reminiscent of the 'palatoquadrate-like' element discussed in various *Dlx* mutants. Such elements were apparent in DCM embryos, and previously described in, for example, *Dlx2*$^{-/-}$ [(Qiu et al., 1995), 1995, Figure 4B, D], *Dlx1*$^{-/-}$*;Dlx2*$^{-/-}$ [(Qiu et al., 1997), Figure 3E, G], *Dlx2*$^{-/-}$*;Dlx5*$^{-/-}$ [(Depew et al., 2005), Figure 11G], and *Dlx1*$^{-/-}$*;Dlx2*$^{-/-}$*;Dlx5*$^{-/-}$ [(Depew et al.,

2005), Figure 16B] mutants – although variations are noted between genetic models. *Larger boxes indicate the complexity of *Dlx* allelic combinations that can generate variations of these ectopic processes. See references cited for individual details.

(**E**) **Additional BA1 and caudal BA derivatives**: Several other unique features were shared between AP-2 and *Dlx* mutants. In regard to more caudal BA derivatives, the hyoid was often found cleft in SCM-A embryos and fused with the thyroid cartilages. Such features were noted in *Dlx2*$^{-/-}$ [(Depew et al., 2005), Figure 9D], *Dlx1*$^{-/-}$*;Dlx2*$^{-/-}$ [(Depew et al., 2005), Figure 9H], various *Dlx2;Dlx5* compound [(Depew et al., 2005), Figure 11G, I, Figure 12J], *Dlx1*$^{-/-}$*;Dlx2*$^{-/-}$*; Dlx5*$^{-/-}$ [(Depew et al., 2005), Figure 16B], and *Dlx2*$^{-/-}$*Dlx6*$^{-/-}$ [(Jeong et al., 2008), Figure S6L] mutants. More strikingly, the hyoid was fused to the cranial base/pterygoids in DCM embryos. Again, this unusual phenotype was observed in various *Dlx* mutants, notably *Dlx5*$^{-/-}$*;Dlx6*$^{-/-}$ embryos [(Beverdam et al., 2002), Figure 2E]. Additional noted similarities include a variably affected styloid process in SCM-A and DCM embryos, as seen in *Dlx2*$^{-/-}$ [(Qiu et al., 1995), Figure 4B; (Depew et al., 2005), Figure 4E], *Dlx5* $^{-/-}$ [(Acampora et al., 1999), Figure 4B], and *Dlx5*$^{-/-}$*;Dlx6*$^{-/-}$ [(Depew et al., 2002), Figure 3D] mutants. Similarly, the tympanic and gonial bones were variably affected in SCM-A and absent in DCM embryos. Such a continuum was observed in *Dlx* mutants, including hypoplastic formation of these elements in *Dlx6*$^{-/-}$ mutants [(Jeong et al., 2008), Figure 5J], major hypoplasia in *Dlx1*$^{-/-}$*;Dlx6*$^{-/-}$, *Dlx2*$^{-/-}$*;Dlx6*$^{-/-}$ mutants [(Jeong et al., 2008), Figure 6c, d], and complete ablation in *Dlx2*$^{-/-}$*;Dlx5*$^{-/-}$ mutants [(Depew et al., 2005), Figure 11G].

(**F**) **Secondary palatal development**: Although not discussed in detail, several *Dlx* allelic combinations result in clefting of the secondary palate, due to defects in palatal processes of the palatine and maxillary bones – as well as altered pterygoids. Similarly, SCM-A, occasionally SCM-B, and DCM embryos develop overlapping palatal defects.

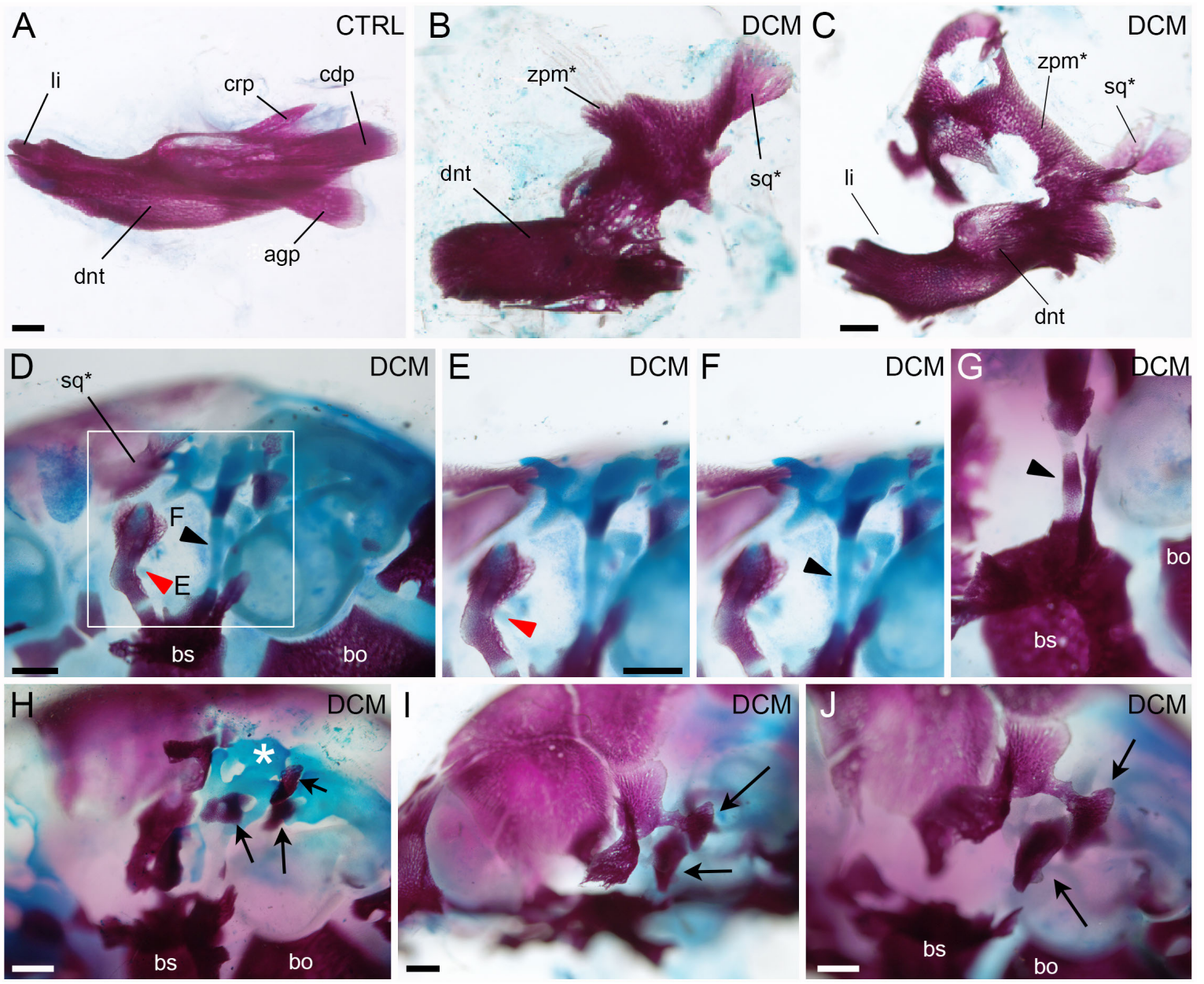

Figure S9 – Additional images of 'Dlx-like' skeletal defects observed in *Tfap2a/Tfap2b-Wnt1*:CRE (DCM) mutants. (**A-J**) Images of E18.5 skeletal preparations of the indicated genotype. (**A-C**) Lateral views (anterior left) of control (**A**) or DCM (**B-C**) mandibles in isolation. Note, the entire maxillary bone is also included in panel **C**, which is fused by its zygomatic process to a modified coronoid process. (**D-J**) Additional ventral views (anterior medial at bottom left) of BA1 hinge-region associated defects detected within the cranial walls and cranial base of DCMs. Various bones (maxillary, palatal, etc) have been removed for better visualization. (**D-G**) highlight ectopic struts (red arrowhead for rostral and black arrowheads for caudal). Panel D is from the same embryo shown in Fig. 6L and panel **E** and **F** are higher magnification images of the boxed area in panel D shot in different focal planes to highlight either the rostral or the caudal strut, respectively. (**H-J**) Show examples of abnormal bone (black arrows) and cartilage elements (white asterisk) with unclear relationship to the normal skeletal derivatives of the cranial base and cranial sidewalls. Comparable control images of the cranial base and side walls are presented in Figs 5 and 6. Abbreviations: agp, angular process; bo, basioccipital; bs, basisphenoid; cdp, condylar process; crp, coronoid process; dnt, dentary; li, lower incisor; sq*, transformed squamosal; zpm* transformed zygomatic process of the maxilla. Scale bars = 500μM.

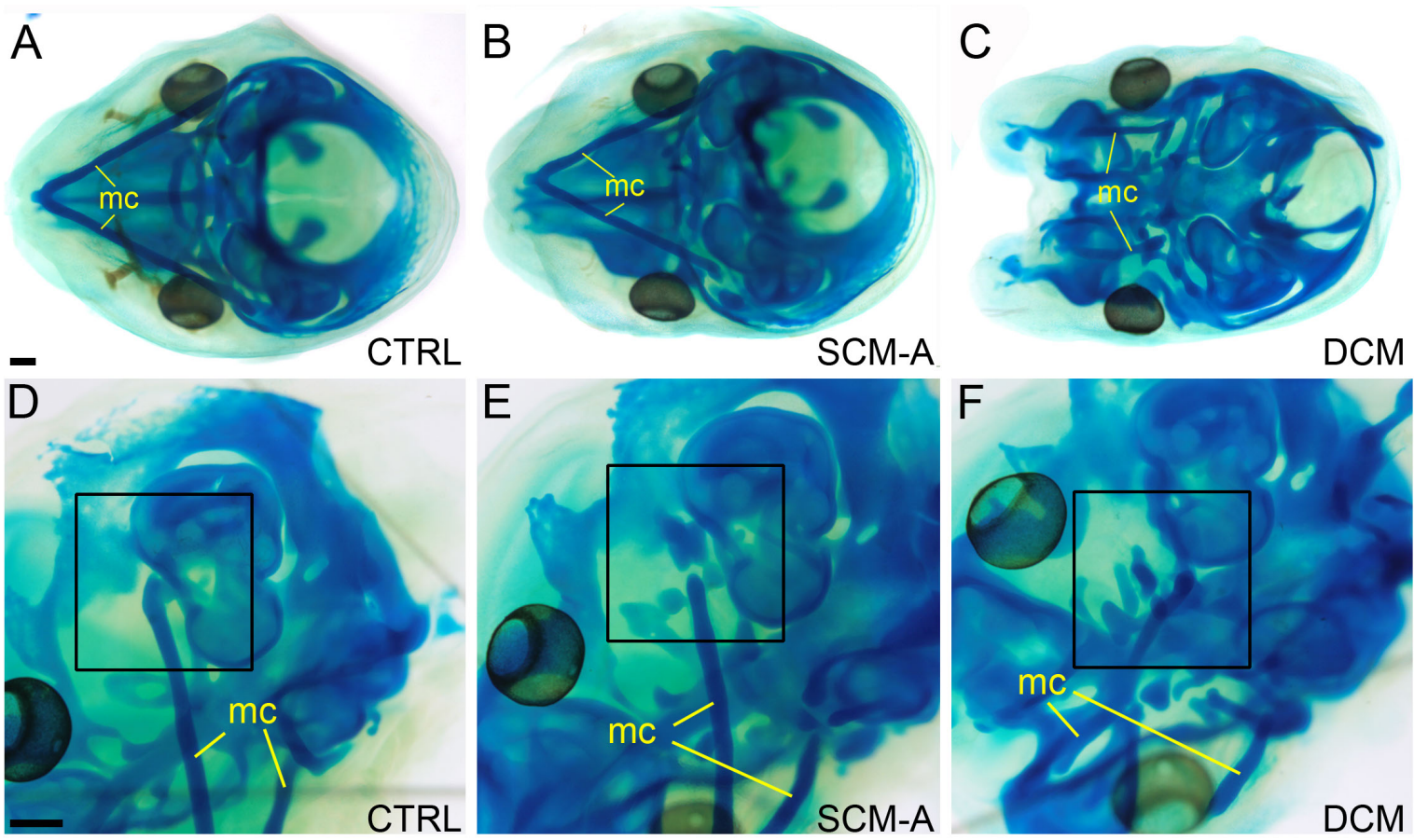

Figure S10 – Additional images of the chondrocranium in *Tfap2a/Tfap2b-Wnt1*:CRE (DCM) and *Tfap2a-Wnt1*:CRE (SCM-A) mutants. (**A-F**) E15.5 cartilage preparations of the indicated genotype shown in either ventral, anterior to the left (**A-C**), or ventrolateral, anterior to the bottom left (**D-F**), views. Boxed regions in D-F highlight the proximal end of Meckel's cartilage. Abbreviations: mc, Meckel's cartilage. Scale bars = 500µM.

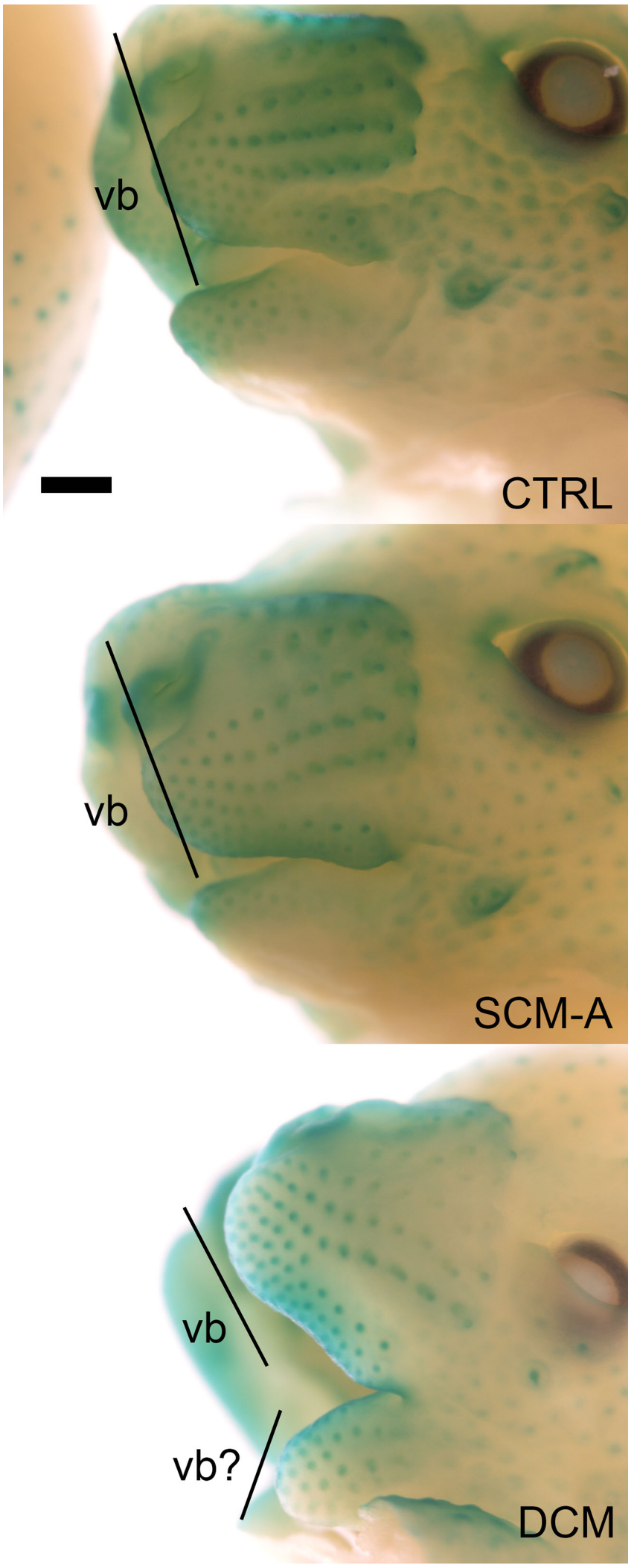
vb
CTRL
vb
SCM-A
vb
vb?
DCM

Figure S11 – Vibrissae-like structures in lower-jaw of *Tfap2a*/*Tfap2b*-*Wnt1*:CRE mutants.

(**A-C**) Lateral views of E14.5 embryos, of the indicated genotype, processed for ß-galactosidase staining. The staining is the result of a *Tfap2a LacZ* knock-in reporter allele (Brewer et al., 2002), highlighting endogenous *Tfap2a* expression – which includes the developing vibrissae (vb). Scale bar = 500µM.

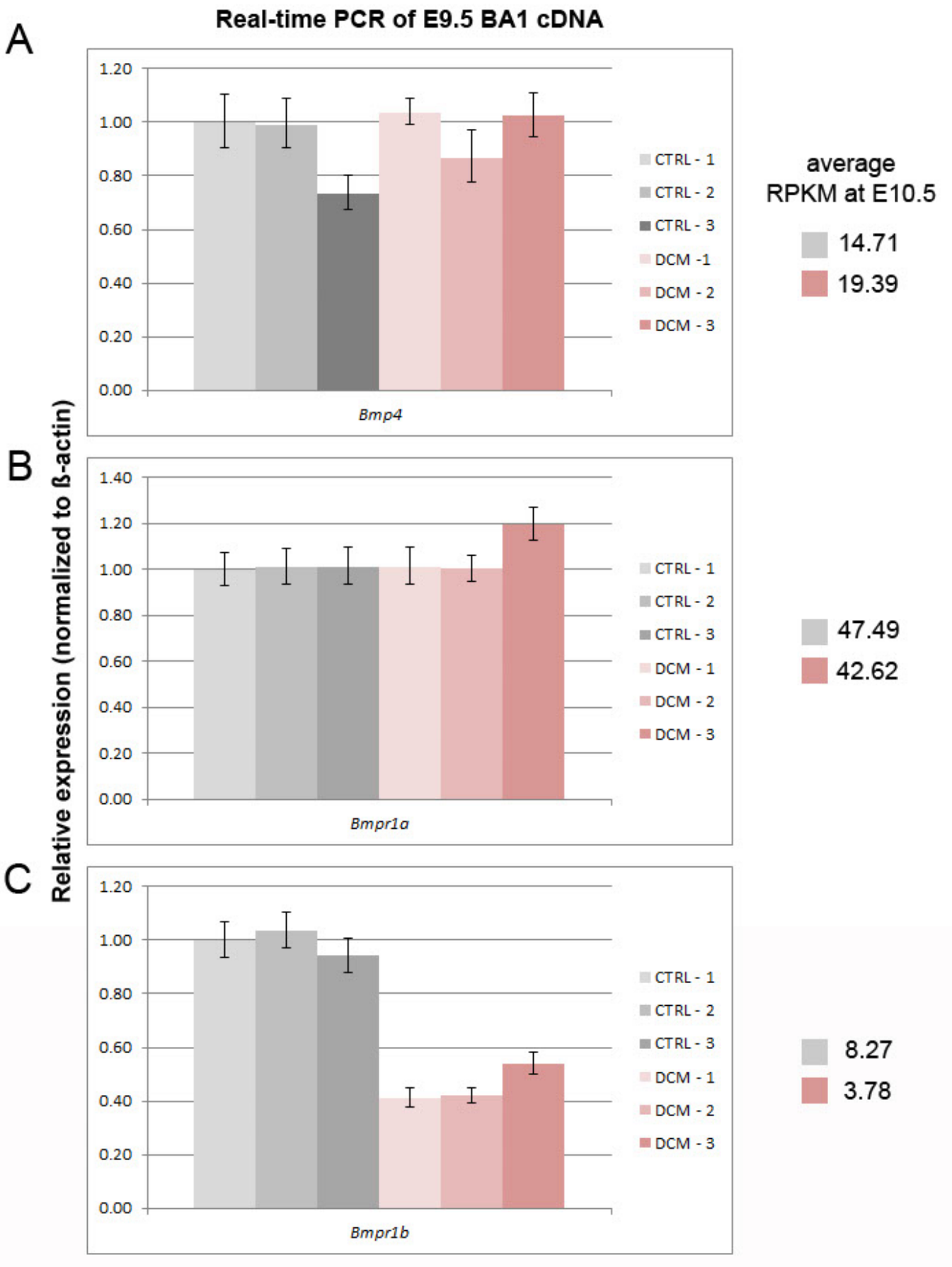

Figure S12. Real-time PCR analysis of BMP-pathway. (**A-C**) Charts summarizing real-time PCR quantification expression levels of *Bmp4* (**A**), *Bmpr1a* (**B**), and *Bmpr1b* (**C**) in E9.5 BA1 cDNA from CTRL and DCM embryos relative to *Actb* (ß-actin). Each bar represents a single embryo, with standard error of technical replicates reported. Values to the right of each chart report the average RPKM value for each gene, based on the E10.5 RNA-seq analysis.

Table S1 – Summary of phenotypes in various AP-2 allelic combinations

Table S1. Genotype and phenotype information for the neural crest *Tfap2a/Tfap2b* gene targeting studies

A. Genotypes derived from mating scheme

Genotype	Description	Abbreviation	CRE
Tfap2a$^{wt/flox}$ *Tfap2b*$^{wt/flox}$	control	ctrl	negative
Tfap2a$^{null/flox}$ *Tfap2b*$^{wt/flox}$	control	ctrl	negative
Tfap2a$^{wt/flox}$ *Tfap2b*$^{null/flox}$	control	ctrl	negative
Tfap2a$^{null/flox}$ *Tfap2b*$^{null/flox}$	control	ctrl	negative
Tfap2a$^{wt/flox}$ *Tfap2b*$^{wt/flox}$ *Wnt1*:CRE	Double conditional heterozygote	DCH	positive
Tfap2a$^{null/flox}$ *Tfap2b*$^{wt/flox}$ *Wnt1*:CRE[ǂ]	Single conditional mutant - *Tfap2a*	SCM-A	positive
Tfap2a$^{wt/flox}$ *Tfap2b*$^{null/flox}$ *Wnt1*:CRE[‡]	Single conditional mutant - *Tfap2b*	SCM-B	positive
Tfap2a$^{null/flox}$ *Tfap2b*$^{null/flox}$ *Wnt1*:CRE*	Double conditional mutant	DCM	positive

[ǂ] ~11% of SCM-A embryos (4 of 38 at E18.5) develop exencephaly, a phenotype that was also noted in ~15% of Tfap2a-Wnt1:CRE mice (Brewer S et al 2004)

[‡] ~22% of SCM-B embryos developed gross cleft secondary palate

* Number of DCM embryos recovered at E18.5, ~4% instead of expected 12.5%, 8 DCMs of 210 total embryos, in comparison to E10.5/E11.5, ~10.5%, 72 DCMs of 695 total embryos, indicates a proportion of embryos die in between these gestational ages. Also, ~50% of embryos (4 of 8 at E18.5) develop exencephaly - for subsequent analysis we concentrated on embryos that lacked exencephaly as this abnormality alone can directly impact craniofacial morphology (Green RM et al 2016)

B. Summary of select craniofacial defects in E18.5 single and double conditional mutant skeletons relative to controls

Genotype (abbreviation)	N	*palate*	*premaxillary*	*mandibular*	*hyoid*	*zygomatic arch*	*squamosal*	*ectopic strut*	*tympanic*
Controls (CTRL)	14	0% (0)	0% (0)	0% (0)	0% (0)	0% (0)	0% (0)	0% (0)	0% (0)
Tfap2a$^{null/flox}$;*Tfap2b*$^{wt/flox}$;*Wnt1CRE (SCM-A)*	18	100% (18)	22% (4)	72%[1] (13)	56%[2] (10)	100%[3] (18)	39%[4] (7)	100%[5] (18)	67%[8] (12)
Tfap2a$^{wt/flox}$;*Tfap2b*$^{null/flox}$;*Wnt1CRE (SCM-B)*	9	22% (2)	0% (0)	0% (0)	0% (0)	0% (0)	0% (0)	0% (0)	0% (0)
Tfap2a$^{null/flox}$;*Tfap2b*$^{null/flox}$;*Wnt1CRE (DCM)*	6	100% (6)	100% (6)	100%[1] (6)	100%[2] (6)	100%[3] (6)	100%[4] (6)	100%[5] (6)	100%[8] (6)

Summary of categories: **palate**, presence of cleft secondary palate; **premaxillary**, presence of midface cleft (split/cleft premaxillary bones, see Figure 5F); **mandibular**, defects found at proximal end of dentary bone (coronoid, condylar, or angular processes); **hyoid**, defects found in hyoid (hypoplastic, 'pinched', cleft); **zygomatic arch** (ZGA), any defects associated with ZGA, including truncated zygomatic processes, missing jugal, etc; **squamosal**, either ectopic foramina in bone and/or hypoplastic/ablated bone; **ectopic strut**, ectopic bony or cartilaginous elements (as described in text); **tympanic**, hypoplastic or missing tympanic bone.

Additional details on phenotypes: [1]Defects in SCM-A skeletons generally corresponded to hypoplastic mandibular processes (see Figure 5N), whereas in DCM skeletons these defects were associated with major loss of the proximal end of the manidble or fusion of lower-jaw to upper-jaw components (see Figure 5O, O'). [2]Defects in SCM-A embryos generally corresponded to small medial 'pinched' or occasional cleft hyoid, with no cranial base fusion (see Figure 6P, S), whereas DCM embryos always had a cleft hyoid found fused to the cranial base (see Figure 6U, X). [3]Defects in SCM-A embryos generally corresponded to shorter zygomatic processes of the maxilla and squamosal (see Figure 5H, K), whereas in DCM embryos these structures were generally ablated (see Figure 5I, L), or more severely truncated (see Figure 5I). [4]A portion of SCM-A skeletons displayed ectopic foramina in the squamosal (see Figure 6H), whereas this structure was either missing or severely malformed in DCM skeletons (see Figure 6I). [5]As described in the text, ectopic struts found in SCM-A and DCM embryos were not identical (compare Figure 6K, L). [8]The tympanic bone, including associated gonial bone, in SCM-A skeletons was hypoplastic (see Figure 6H, K), whereas the bone was completely missing in DCM skeletons (see Figure 6I, L, N).

Table S2 – Class I, Class II, and Class III gene-lists

Click here to Download Table S2

Table S3 – Curated list of genes used for gene set enrichment analysis

Click here to Download Table S3

Table S4 – Information relevant to genotyping primers

ALLELES	PRIMERS	ANNEALING TEMP	PCR PRODUCTS*
Tfap2a-KI (lacZ knock-in)	Alf6/7 (240) : a3KO (200) : iresup (120)	70°C	wt = 500, ki = 300
Tfap2a-null	Alf6/7 (200) : a3KO (240) : Neo3KO (120)	70°C	wt = 500, null = 265
Tfap2a-conditional	Aflox4 : Ascsq	65°C	wt = 496, conditional = 550
Tfap2b-null	Bfl1 : Revbeta6	70°C	wt = 210, conditional = 300‡
Tfap2b-conditional	Bfl1 : Bfl2	70°C	wt = 430, conditional = 550
Wnt1:CRE	Wnt1CRE-F : Wnt1CRE-R	70°C	transgene = ~450
Sox2:CRE	Cre 1 : Cre 3	68°C	transgene = 450
PRIMER SEQUENCES			
Alf6/7	5'-AGG-TGT-AGG-CAG-AAG-TTT-GTC-AGG-GC-3'		
a3KO	5'-CGT-GTG-GCT-GTT-GGG-GTT-GTT-GCT-GAG-GTA-C-3'		
iresup	5'-GCT-AGA-CTA-GTC-TAG-CTA-GAG-CGG-CCC-GGG-3'		
Neo3KO	5'-AAC-GCA-CGG-GTG-TTG-GGT-CGT-TTG-TTC-G-3'		
Aflox4	5'-CCC-AAA-GTG-CCT-GGG-CTG-AAT-TGA-C-3'		
Ascsq	5'-GAA-TCT-AGC-TTG-GAG-GCT-TAT-GTC-3'		
Bfl1	5'-GTC-TGT-TTA-GAA-CAG-CCA-GAG-GCT-GG-3'		
Revbeta6	5'-CCC-GAG-CTA-AGT-GAA-CAG-CTT-CCC-CTG-TAA-GGA-GAG-C-3'		
Bfl2	5'-TCT-GGC-AAG-GCT-CGC-ACT-CAC-AGC-AG-3'		
Wnt1CRE-F	5'-CTC-ATT-GTC-TGT-GGC-CCT-GAC-C-3'		
Wnt1CRE-R	5'-ACG-CCT-GGC-GAT-CCC-TGA-AC-3'		
Cre 1	5'-GCT-GGT-TAG-CAC-CGC-AGG-TGT-AGA-G-3'		
Cre 3	5'-CGC-CAT-CTT-CCA-GCA-GGC-GCA-CC-3'		

*numbers listed for PCR products corresponds to length in basepairs

‡Note, when genotyping *Tfap2b* -null allele, primers were used that did not recognize the deleted allele, but rather indicated if the WT-allele was present (along with generating a conditional-specific PCR product). Embryos in which no WT-allele was present identified those which recieved the paternally derived *Tfap2b* -null allele. This strategy was utilized to prevent false-positives as a result of recombination of the *Tfap2b* -conditional allele.

Numbers in red correspond to the final concentration of primers used, reported in nM. All other primers were used at final concentration of 200nM.

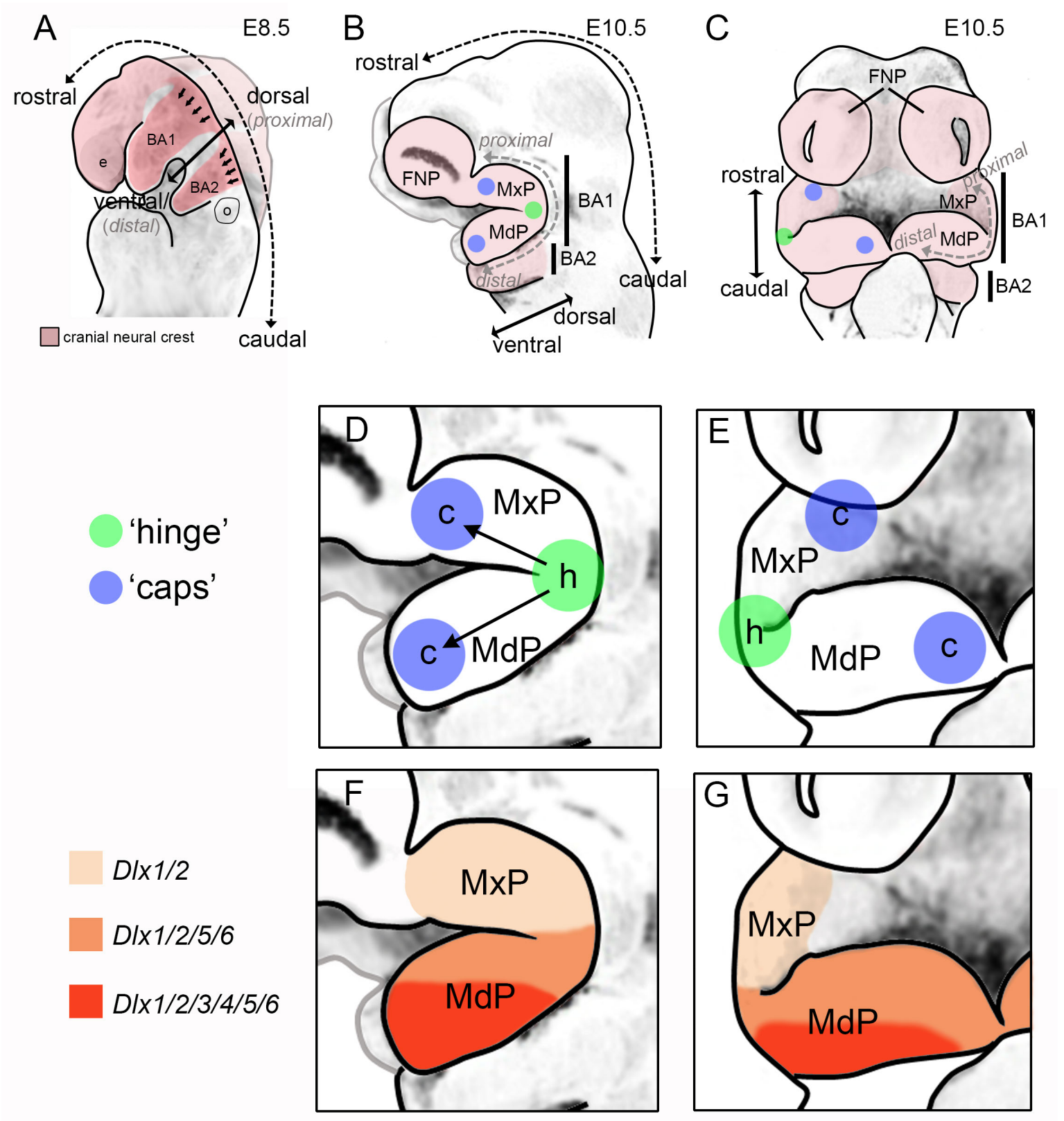
A
E8.5
rostral
dorsal
(proximal)
BA1
e
BA2
ventral/
(distal)
o
cranial neural crest
caudal
B
E10.5
rostral
proximal
FNP
MxP
BA1
MdP
BA2
distal
caudal
dorsal
ventral
C
E10.5
FNP
rostral
proximal
MxP
BA1
distal
MdP
caudal
BA2
'hinge'
'caps'
D
c
MxP
h
c
MdP
E
c
MxP
h
MdP
c
Dlx1/2
Dlx1/2/5/6
Dlx1/2/3/4/5/6
F
MxP
MdP
G
MxP
MdP

Figure S1 – Anatomical locations during mouse craniofacial development. (**A-G**) Dorsolateral (**A**), lateral (**B, D, F**), or ventral (**C, E, G**) schematics of an E8.5 (**A**) or E10.5 (**B-G**) mouse embryo, focusing on craniofacial regions and highlighting key anatomical axes and structures. (**A**) By E8.5, neural crest cells (red shading) that have originated from the dorsal neural tube of hind-, mid-, and forebrain regions are beginning to migrate ventrolaterally into the developing craniofacial structures (note, neural crest cells caudal to branchial arch 2 are not labeled). The dorsal-ventral (proximal-distal) axis of branchial arch 1 is less ambiguous at these earlier developmental stages. (**B, C**) By E10.5, NCCs (pink shading) have ceased migration, and have contributed to the majority of the craniofacial mesenchyme. Additionally, the first branchial arch has become further refined into maxillary (MxP) and mandibular (MdP) prominences – which will form components of the upper and lower jaw, respectively. Note, studies have indicated, at least in avian models, that the MxP may not be derived from NCCs of BA1 (Cerny et al., 2004; Lee et al., 2004). Nevertheless, subdivision of BA1 into these two prominences in mammals somewhat obfuscates anatomical orientations, but traditionally the MxP is referred to as dorsal/proximal and the MdP ventral/distal. BA1 can also be subdivided into the ‘hinge’ (green dot), that is the intersection of the MxP and MdP, and ‘caps’ (blue dots), that is, the regions furthest from the hinge in both the MxP and MdP (Depew and Compagnucci, 2008; Depew et al., 2002; Depew and Simpson, 2006; Depew et al., 2005). We primarily reference these latter terms when discussing BA1. Panels D and E show BA1 and relative positions of the proposed ‘hinge’ and ‘caps’ in more detail, whereas panels F and G highlight the ‘nested Dlx-code’ within the same region. Abbreviations: BA1, branchial arch 1 (i.e. mandibular arch); BA2, branchial arch 2 (i.e. hyoid arch); c, cap; e, eye; FNP, frontonasal prominence; h, hinge; MdP, mandibular prominence; MxP, maxillary prominence; o, otic vesicle.

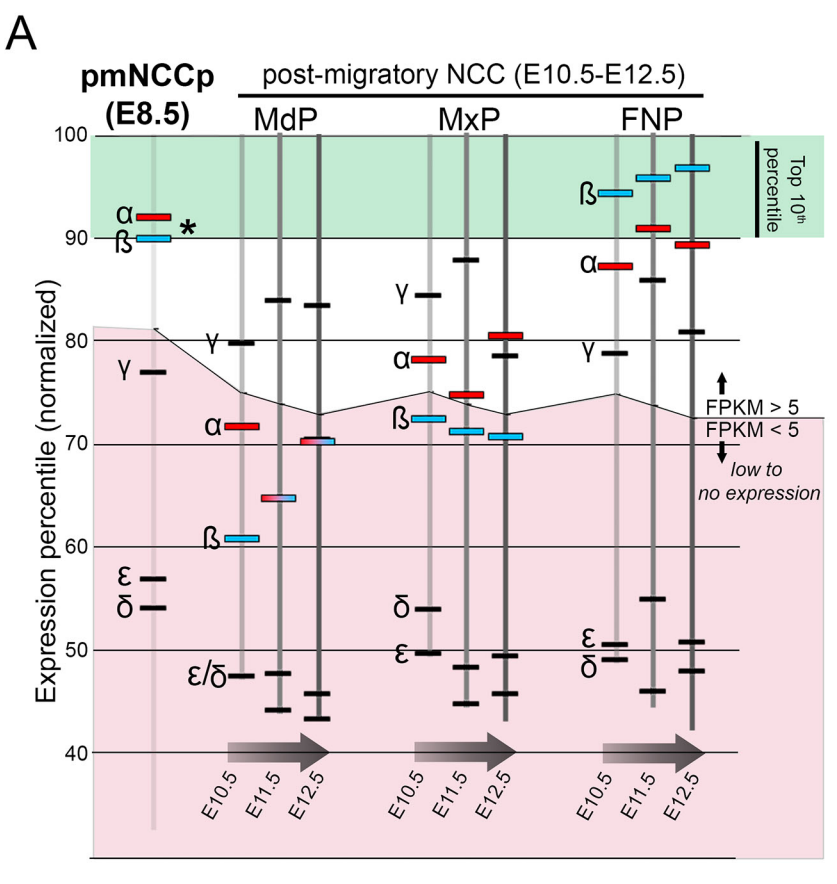

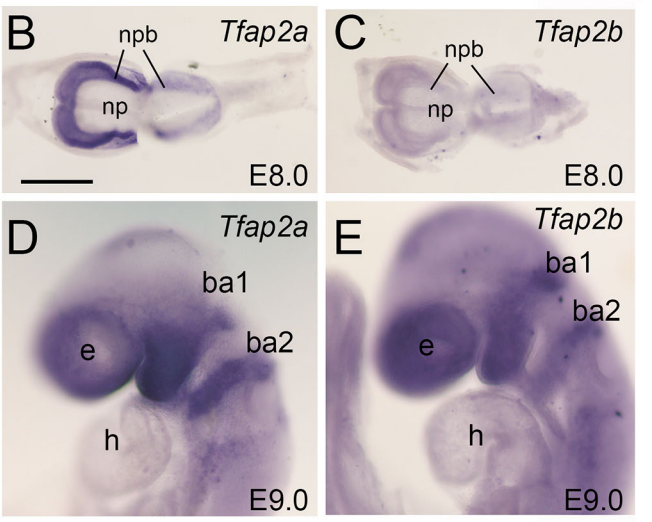

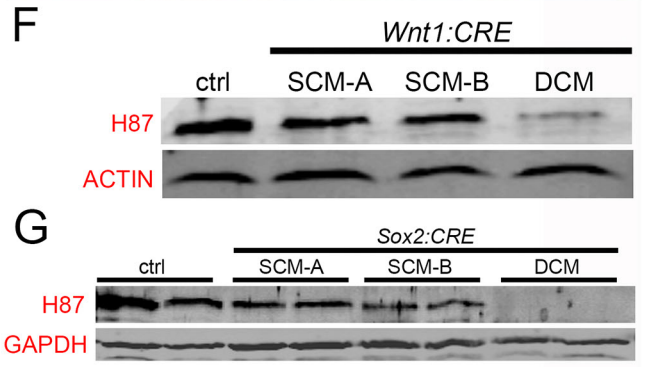

Figure S2 – *Tfap2a* and *Tfap2b* are the most highly expressed paralogs in early mouse cranial NC. (**A**) Chart depicting expression percentile of all genes (based on 'normalized FPKM rank') for E8.5 (Minoux et al., 2017), and E10.5-E12.5 cranial mesenchyme (Hong Li, manuscript in prep, data available at Facebase) – essentially ranking gene expression levels across the entire RNAseq dataset (90-100 on Y-axis, highlighted green, corresponds to the top 10th percentile of expressed genes within a dataset). Ranked position of *Tfap2a* (red bar with label 'α') and *Tfap2b* (blue bar with label 'ß'), as well as other *Tfap2* paralogs (black bars, *Tfap2c* = γ, *Tfap2d* = δ, and *Tfap2e* = ε) are indicated within each dataset. Note, the percentile corresponding to an FPKM of 5 is highlighted in each dataset with genes ranked below this line shown in pink, corresponding to very low or essentially non-expressed genes. (**B-E**) Images of whole-mount *in situ* hybridization of E8.0 dorsal view (**B, C**) or E9.0 lateral view (**D, E**) wild-type embryos, processed with a *Tfap2a* (**B, D**) or *Tfap2b* (**C, E**) antisense riboprobe. (**F**) Collective AP-2α and AP-2ß protein expression levels (as detected by H-87 antibody) in E10.5 facial prominence tissue isolated from the indicated genotypes. ACTIN serves as a loading control. Residual AP-2 immunoreactivity in DCMs represents expression in the ectoderm, which is not targeted by *Wnt1:*CRE. (**G**) Same as in (**F**) with the exception that protein was isolated from E12.5 *Sox2:*CRE embryos of the indicated genotype. GAPDH serves as the loading control. Note, *Sox2:*CRE will target AP-2 expression in both the ectoderm and neural crest derived tissues. Note, for **F** and **G**, each lane corresponds to protein isolated from a single embryo. Abbreviations: ba1, branchial arch 1; ba2, branchial arch 2; FNP, nasal prominence; h, heart; MdP, mandibular prominence; MxP, maxillary prominence; np, neural plate; npb, neural plate border; pmNCCp, premigratory cranial neural crest precursors; Scale bars = 500µM.

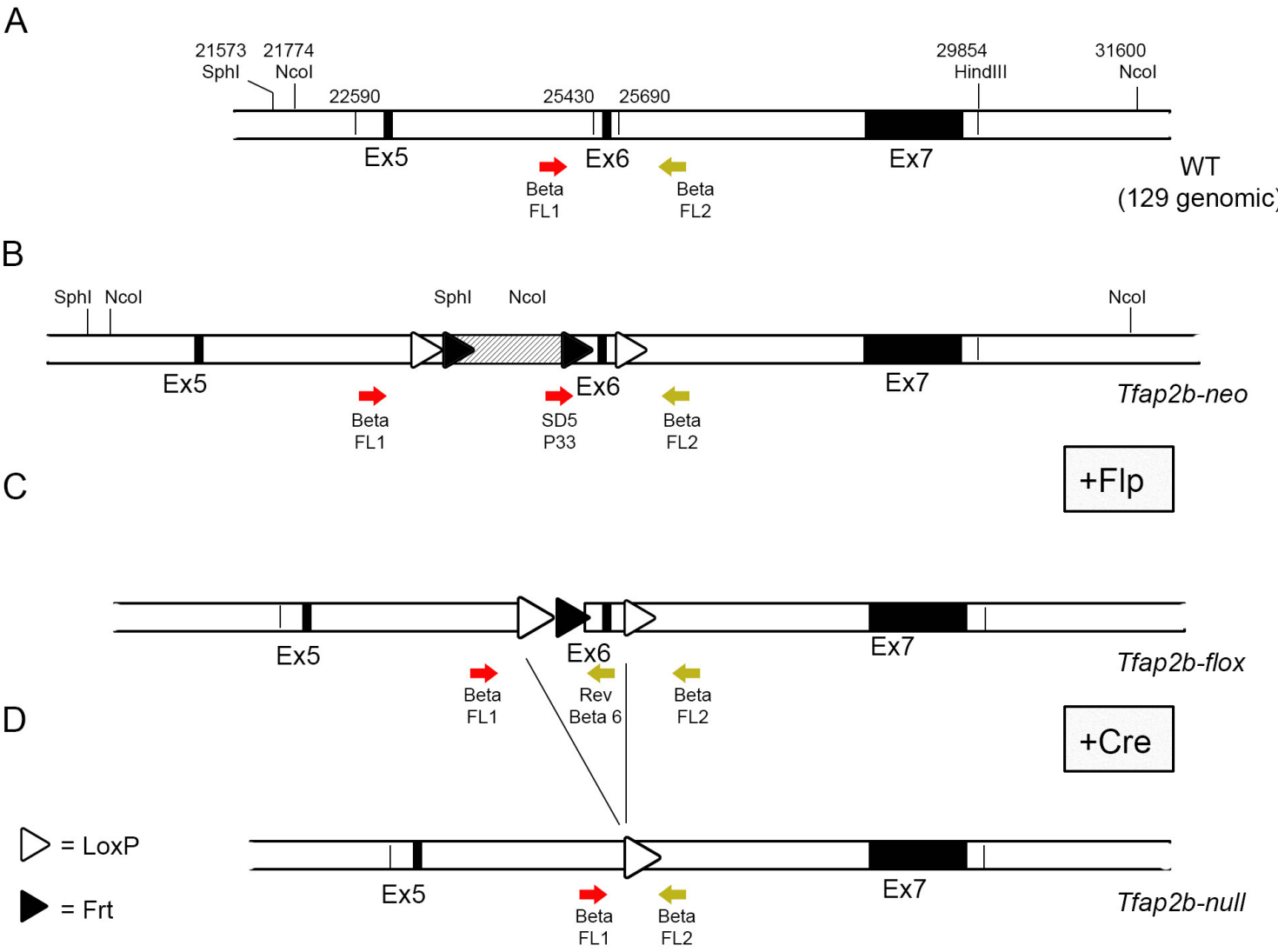

Figure S3 – Schematic of *Tfap2b* alleles generated and utilized in this study. (**A**) Diagram of endogenous *Tfap2b* genomic locus, focused on regions corresponding to exons 5, 6 and 7 (black boxes). Relative genomic positions, including selected restriction sites, are indicated. (**B**) Layout of locus (*Tfap2b-neo*) after targeted homologous recombination, with *neomycin* selection cassette still present (hashed box) and incorporated *LoxP* and *Frt* sites near exon 6. (**C**) Graphic representation of modified *Tfap2b* allele following FLP-mediated recombination resulting in the removal of the *neomycin* cassette and generation of a *Tfap2b* conditional allele (*Tfap2b-flox*). This allele contains *LoxP* recombination sites flanking exon 6 of *Tfap2b*. (**D**) *Tfap2b* locus following CRE-mediated recombination (*Tfap2b*-null). Excision of exon 6 of *Tfap2b* results in a functional null allele in the CRE-recombinase expressing cells/tissues and their derivatives. Colored arrows show positions of primers used for PCR genotyping.

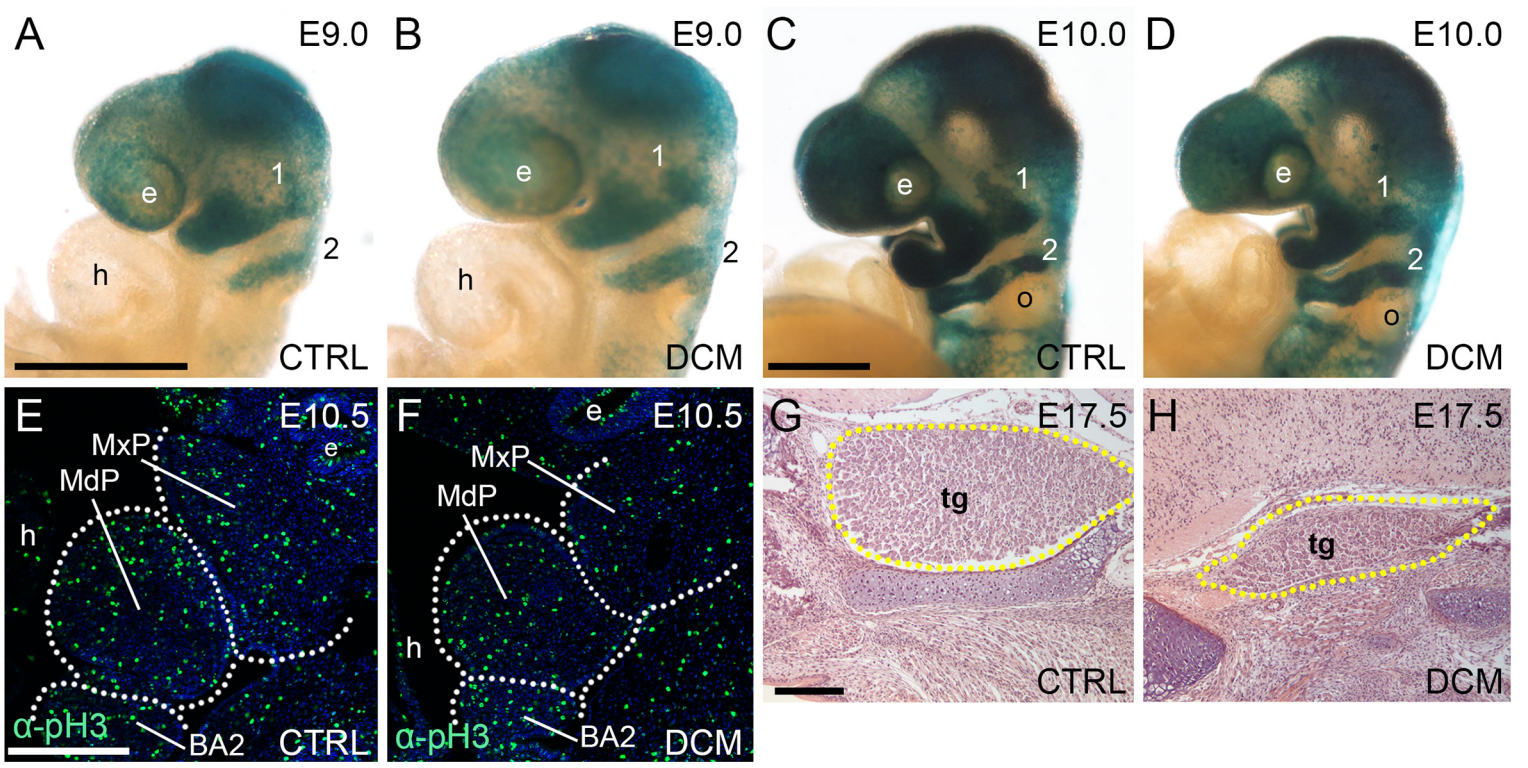

Figure S4 – NC development in *Tfap2a*/*Tfap2b*-*Wnt1*:CRE mutants. (**A-D**) Lateral views of E9.0 (**A, B**) and E10.0 (**C, D**) *Wnt1:*CRE *R26 reporter* embryos, of the indicated genotype processed for ß-galactosidase staining to label NCC lineages. 1 and 2 corresponds to BA1 and BA2 NCC streams, respectively. (**E, F**) Anti-α-phospho-Histone H3 immunofluorescent stained parasagittal paraffin sections through BA1 and BA2 of a control (**E**) or DCM (**F**) E10.5 embryo to label proliferative cells. (**G, H**) H&E stained frontal sections from E17.5 embryos of the indicated genotype, with the trigeminal ganglia outlined by the yellow dashed lines. Abbreviations: BA2, branchial arch 2; e, eye; h, heart; MdP, mandibular prominence; MxP, maxillary prominence; o, otic vesicle; tg, trigeminal ganglion. Scale bars = 500µM.

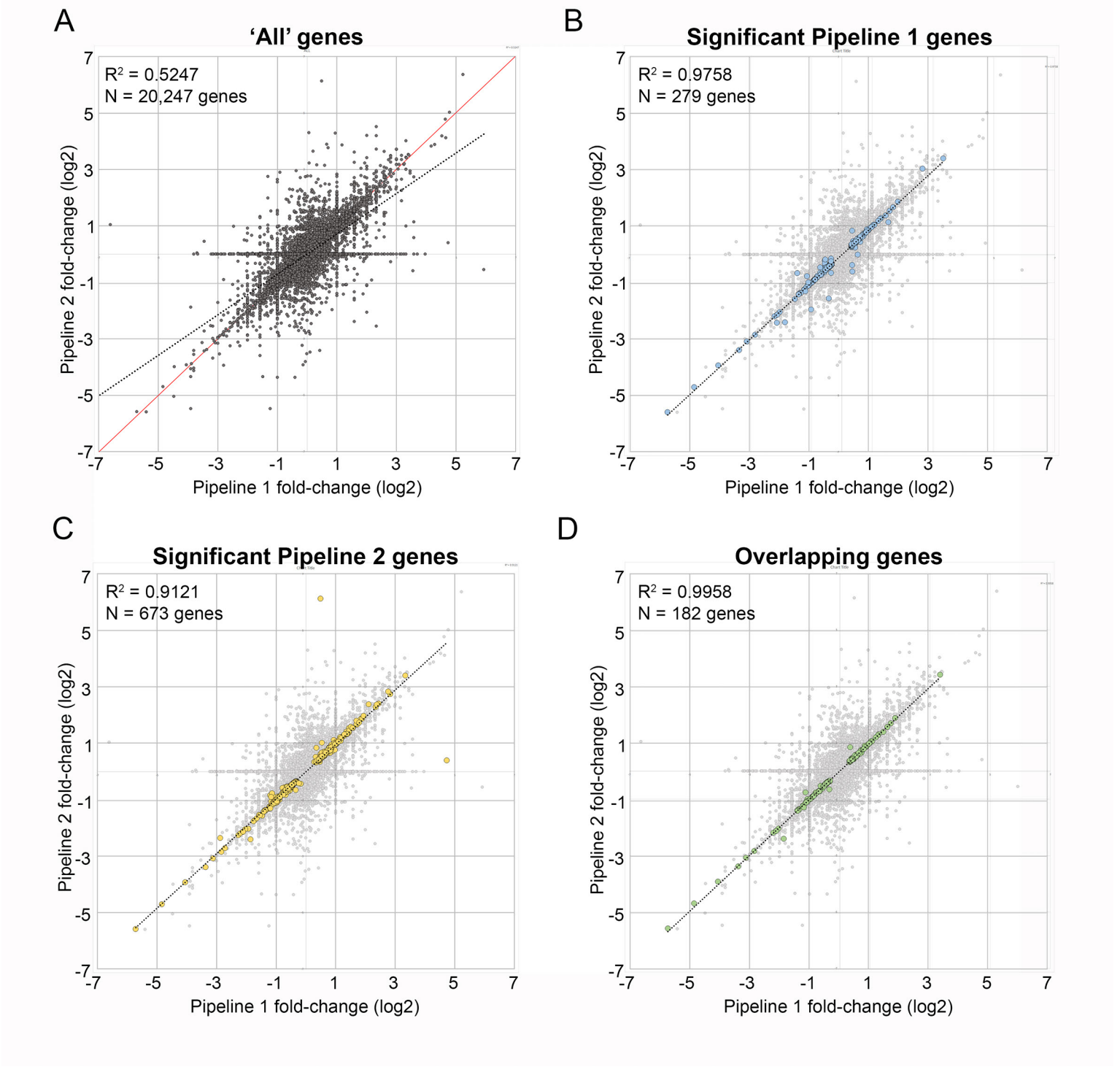

Figure S5 – Comparison of gene expression values between bioinformatic pipelines. (**A-D**) Scatterplots displaying calculated fold-change values (control versus *Tfap2a/Tfap2b-Wnt1*:CRE mutants, log2 scale) between 'Pipeline 1' (X-axis) and 'Pipeline 2' (Y-axis). For **A-D** the calculated R^2-value (correlation coefficient) and number (N) of genes analyzed is reported in the top left corner. For **B-D**, the 'All' gene dataset from panel A is displayed as a light gray graph underneath. **A**) Analysis of all genes. **B**) Analysis of genes only called significant in Pipeline 1 (Class I genes). **C**) Analysis of genes only called significant in Pipeline 2 (Class II genes). **D**) Analysis of overlapping genes between both Class I and II datasets (i.e. Class III genes).

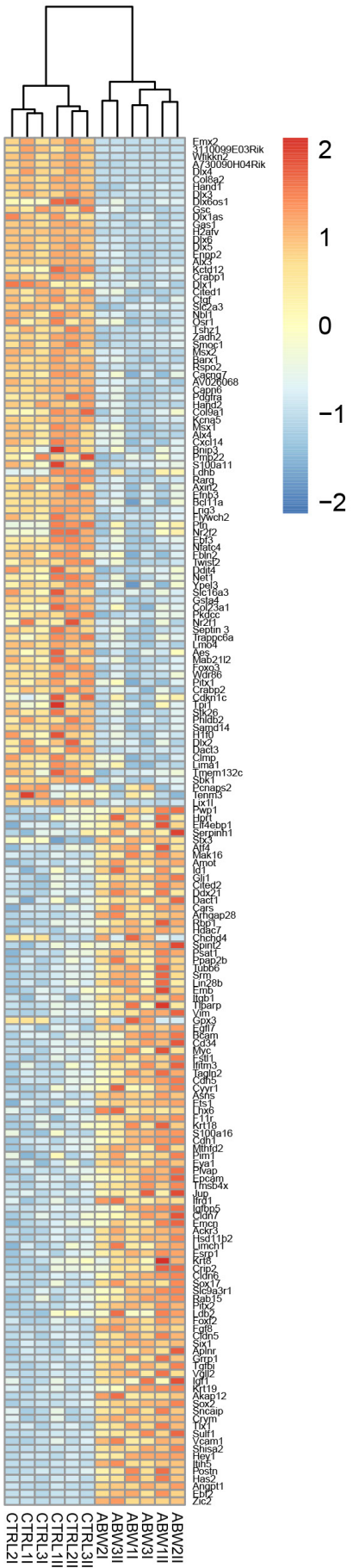
2
1
0
−1
−2
Emx2
9130009E03Rik
Wtkkh2
A730090H04Rik
Dlk4
Col8a2
Hand1
Dlk3
Dlx6os1
Gsc
Dlx1as
Gas7
H2afv
Dlx6
Dlx5
Cmpx2
Alx3
Kctd12
Crabp1
Dlx1
Cited1
Cfdl
Slc2a3
Nbl1
Osr1
Ythdc1
Zadh2
Smoc1
Msx2
Barx1
Rspo2
Cacng7
AV028068
Capn6
Pdgfra
Hand2
Col9a1
Kcna5
Msx1
Alx4
Cxcl14
Bnip3
Tmbp22
S100a11
Ldhb
Rarg
Axin2
Emb3
Bcl11a
Lrig3
Tmwch2
Ptn
Nr2f2
Ebf3
Nfatc4
Cbln2
Twist2
Ddit4
Ndt1
Xpel3
Slc16a3
Gsta4
Col23a1
Pkdcc
Nr2f1
Septin 3
Trappc6a
Lmo4
Aes
Mab21l2
Foxo3
Wdr86
Pitx1
Crabp2
Cdkn1c
Tpt1
Slk26
Phldb2
Samd14
Ttbk1
Dlx2
Dact3
Clmp
Lima1
1700009P17Rik
Tmem132c
Sbk1
Pcnags2
Tenm3
Lix1l
Pwp1
Hpn
Eif4ebp1
Serpinh1
Sfx3
Atf4
Mak16
Amot
Id1
Gli1
Clec14a
Ddx21
Dact1
Cars
Arhgap28
Rbp1
Hdac7
Chchd4
Sbno2
Csat1
Ppap2b
Tubb6
Srrt
Lin28b
Emb
Itgb1
Tjparp
Vim
Gpx3
Epas1
Pecam
Cd34
Myc
Fstl1
Ifitm3
Tagln2
Cdh5
Cyyr1
Kdr
Ets1
Dlx6
F11r
Krt18
S100a16
Cdh1
Mthfd2
Tpm1
Eya1
Flvcr1
Epcam
Tmsb4x
Utp3
Ifrd1
Igfbp5
Cldn7
Emcn
Akr1c18
Hsd11b2
Limch1
Espn1
Krt8
Cnn2
Cldn6
Sox17
Slc9a3r1
Rab15
Ptk2
Ldb2
Foxf2
Eqtn
Cldn5
Six1
Apln
Grrp1
Tgfbi
Vgll2
Igf1
Krt19
Akap12
Sox2
Sncaip
Crym
Tbx1
Sulf1
Vcam1
Shisa2
Hey1
Ephb1
Postn
Has2
Angpt1
Ebf2
Zic2
CTRL2I
CTRL1I
CTRL3I
CTRL1II
CTRL2II
CTRL3II
ABW2I
ABW3II
ABW1I
ABW3I
ABW1II
ABW2II

Figure S6 – Detailed hierarchical clustering of 182 ‘high-confidence’ gene-set in *Tfap2a*/*Tfap2b*-*Wnt1*:CRE mutants versus controls. ABW indicates the DCM samples, whereas CTRL are the controls. 1, 2, 3 indicates the biological replicate, and I and II corresponds to data from pipeline 1 or 2, respectively.

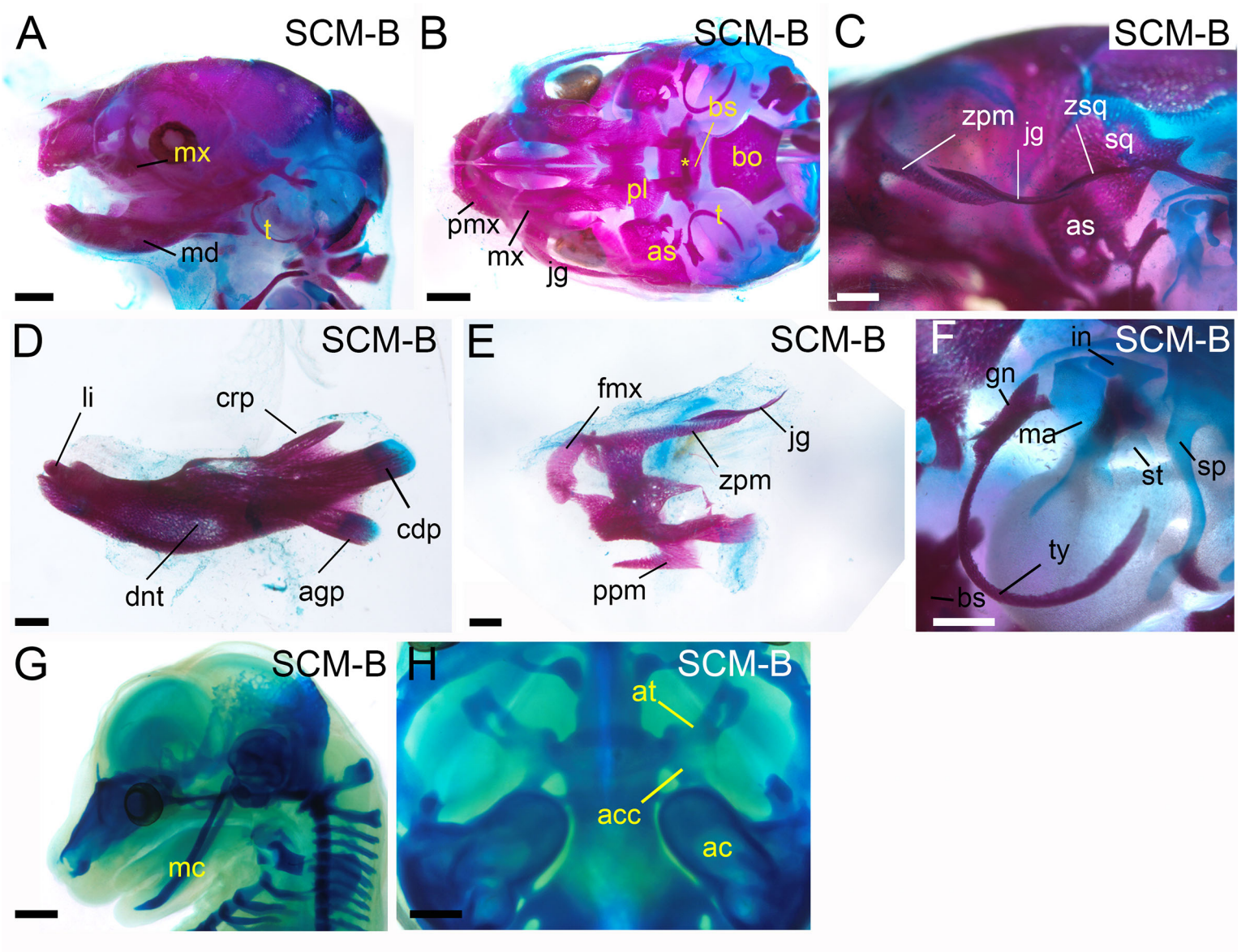

Figure S7 – SCM-B skeletal images. E18.5 skeletal (**A-F**) or E15.5 chondrocranial (**G, H**) preparations. (**A-C**) Whole cranial skeletal preparations in lateral (**A**), ventral (**B**) or ventrolateral (**C**) views, anterior to the left. Note, the mandible has been removed for better visualization in panels B and C, and panel C is a higher magnification image of the zygomatic arch. The asterisk in B highlights the hyoid bone. Mandibular (**D**) or maxillary (**E**) bone shown in isolation, anterior to the left. (**F**) Ventral view, anterior to the upper-left, focusing on the middle ear ossicles. Lateral, anterior left, (**G**) or ventral, anterior up, (**H**) views of the chondrocranium. Compare images to control, SCM-A, and DCM preparations in Figures 5 and 6. Note, SCM-B skeletons resemble controls except for the ~20% that had a cleft secondary palate, and these mutants had palatal process defects typical of this pathology. Abbreviations: ac, auditory capsule; acc, alicochlear commissure; agp, angular process; as, alisphenoid; at, ala temporalis; bo, basioccipital; bs, basisphenoid; cdp, condylar process; crp, coronoid process; dnt, dentary; fmx, frontal process of the maxillary; g, gonial; in, incus; jg, jugal; li, lower incisor; ma, malleus; mc, Meckel's cartilage; md, mandible; mx, maxillary; pl, palatine; pmx, premaxillary; ppm, palatal process of the maxillary; sp, styloid process; sq, squamosal; st, stapes; ty, tympanic; zpm, zygomatic process of the maxillary; zsq, zygomatic process of the squamosal. Scale bars = 1,000 µM (A, B, G), 500µM (C, D, E, F, H).

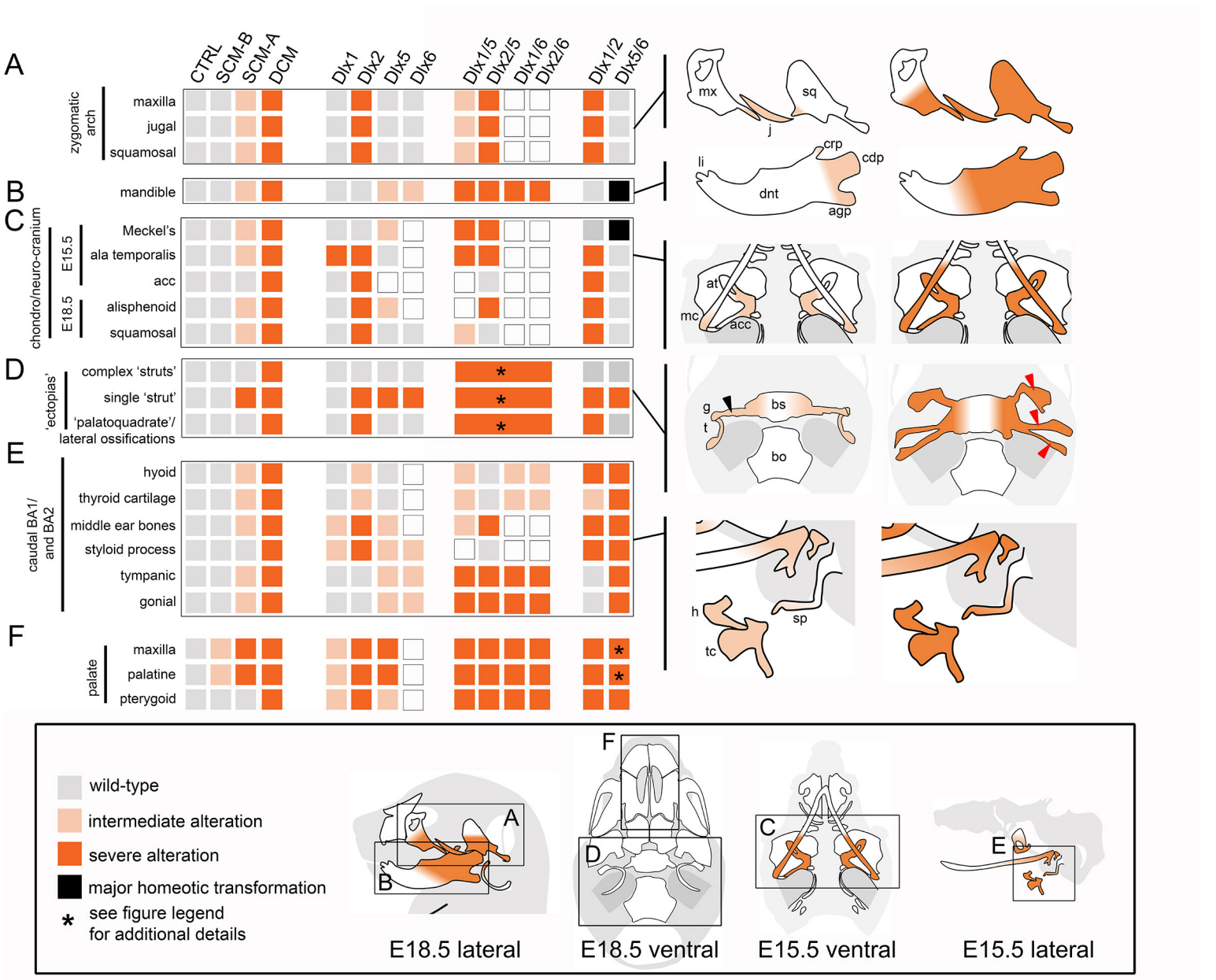

Fig. S8 Summary of overlaps between AP-2α/ß and *Dlx* mutant skeletal phenotypes.

Overview. A heat-map is shown on the left classifying the severity of defects associated with particular components of the craniofacial skeleton at both E15.5 and E18.5 for controls, *Wnt1*:Cre *Tfap2a/b* mutants (based on the images in Figures 5, 6, and S7), and data from the analysis of *Dlx* single and double mutants (1, 2, 5, 6). At the bottom of the figure is shown an overview of the E15.5 and E18.5 skeleton with boxes marking specific regions analyzed in A-F. On the right of the diagram are shown more detailed views of the structures under analysis. These are projected onto a wild-type skeleton, with the exception of the bones of (D) where the first and second columns represent the SCM-A and DCM phenotypes, respectively, and (F) which is not shown. Ectopic struts associated with the cranial base in (D) are shown by arrowheads. In general, grey boxes correspond to relatively wild-type skeletal elements, dark orange boxes represent elements with major developmental defects, whereas light orange represent partial or intermediate defects. Regions where an unshaded box is present represent mouse mutants for which no comment on severity is made. Black boxes indicate major homeotic transformations. Orange color-coding is also used in the schematics to illustrate the severity of the defects. Larger boxes indicate the complexity of *Dlx* allelic combinations that can generate variations of these ectopic skeletal processes. Although several *Dlx* examples are often listed as a reference to the associated defect, such a list is by no means comprehensive. Abbreviations: acc, alicochlear commissure; agp, angular process; at, ala temporalis; bs, basisphenoid; bo, basioccipital; cdp, condylar process; crp, coronoid process; dnt, dentary; g, gonial; h, hyoid; j, jugal; li; lower incisor; mc, Meckel's cartilage; mx, maxillary; sq, squamosal; sp, styloid process; t, tympanic; tc, thyroid cartilage.

(**A**) **Zygomatic arch** (ZGA): Defects in the ZGA range from mild (e.g. loss of the zygomatic process of the squamosal) to severe (more extensive ablations and truncations of the ZGA elements). The appearance of ectopic cartilage/bony elements of unknown lineage (referred to as 'palatoquadrate', discussed more below) are also included in this severe category. For example, SCM-A embryos show a loss of the zygomatic process of the squamosal, similar to [$Dlx1^{-/-};Dlx5^{-/-}$], [$Dlx2^{-/-};Dlx5^{+/-}$], or [$Dlx3^{+/-};Dlx5^{-/-}$] mutants [(Depew et al., 2005), Figure 14E, 13F, and 15F, respectively]. In contrast, DCM embryos display a near ablation of the ZGA (see text),

with an often thickened, truncated zygomatic process of the maxillary bone, as described for example, in *Dlx2*$^{-/-}$*;Dlx5*$^{-/-}$ mutants [(Depew et al., 2005), Figure 11G].

(**B**) **Mandible**: Regions of the mandible most susceptible to loss of AP-2 and Dlx paralogs include the proximal condyles. More mild defects include hypoplastic development of condylar processes, as seen in SCM-A skeletal preparations. Sensitivity of the proximal condyles is also noted in *Dlx5*$^{-/-}$ *and Dlx6*$^{-/-}$ single mutants [(Depew et al., 2005), Figure 7G; (Jeong et al., 2008), Figure 5F, G]. More extreme transformations of the mandible are observed in DCM embryos and are progressively more severe in various *Dlx* allelic combinations [(Jeong et al., 2008), Figure 6G-L; (Depew et al., 2005), Figure 18A-F and Figure 20C, D]. Eventually, in the context of the appropriate *Dlx* paralogs (e.g. *Dlx5*$^{-/-}$*;Dlx6*$^{-/-}$), a threshold is approximated in which the lower-jaw adopts an upper-jaw identity (Beverdam et al., 2002; Depew et al., 2002). Note, such complete transformation is not observed in DCM embryos, although such transformation is often associated with a cleft mandible, which is present in DCM embryos.

(**C**) **Chondro-/Neurocranium**. In respect to the chondrocranial elements, again, intermediate and more severe phenotypes are observed in both AP-2 and *Dlx* mutants. For example, both the upper-jaw ala temporalis and lower-jaw Meckel's cartilage are particularly sensitive to AP-2 and DLX levels. In the context of AP-2 this is observed by mild patterning defects in the ala temporalis of SCM-A embryos and near ablation in DCM embryos. Proximal loss of the ala temporalis was a notable consequence in *Dlx1*$^{-/-}$ [(Qiu et al., 1997), Figure 3B], *Dlx2*$^{-/-}$ [(Qiu et al., 1995), Figure 3B; (Qiu et al., 1997), Figure 2C] and *Dlx1*$^{-/-}$*;Dlx2*$^{-/-}$ [(Qiu et al., 1997), Figure 2D] mutants, with more intermediate defects noted in heterozygous embryos [(Depew et al., 2005), Figure 9F]. Another noted similarly was the loss of the alicochlear commissure in DCM embryos, which was often missing or affected in *Dlx2*$^{-/-}$ [(Qiu et al., 1995), Figure 3B], *Dlx1*$^{-/-}$*;Dlx2*$^{-/-}$ [(Qiu et al., 1997), Figure 2C, D], or more complex compound mutants [e.g. [*Dlx1*$^{+/-}$*;Dlx2*$^{+/-}$*;Dlx3*$^{+/-}$*;Dlx5*$^{+/-}$*;Dlx6*$^{+/-}$], (Depew et al., 2005), Figure 18F]. The lower-jaw, chondrocranial element, Meckel's cartilage, was again intermediately affected in SCM-A embryos (slightly

shorter, with a non-continuous connection with the malleus), whereas in DCM embryos such defects were more severe (see text). Similarly, various *Dlx* mutants display a range of Meckel's cartilage defects. Such defects often impact the proximal end of Meckel's, influencing its association with middle ear structures, such as seen in *Dlx5*$^{-/-}$ mutants [(Depew et al., 2005), Figure 7E). As with the mandible, Meckel's is eventually transformed into its upper-jaw-like counterpart, the ala temporalis in more extreme situations [i.e. *Dlx5*$^{-/-}$*;Dlx6*$^{-/-}$ mutants, (Beverdam et al., 2002; Depew et al., 2002)].

(**D**) **'Ectopias'**: Note, schematics shown in right hand side column 1 and 2 represent ventral views of the cranial base at E18.5 in mutant SCM-A and DCM embryos, respectively. One of the most striking similarities between the AP-2 and Dlx mutants is the appearance of various ectopic structures associated with the cranial base. For example, in SCM-A embryos a single ossified strut (black arrowhead) was observed projecting laterally from the medial basisphenoid, often interacting/fusing with the gonial bone. Several previous reports have identified a highly similar structure in various *Dlx* mutants, including *Dlx2*$^{-/-}$ [(Qiu et al., 1995), Figure 3B, F], *Dlx1*$^{-/-}$*;Dlx2*$^{-/-}$ [(Qiu et al., 1997), Figure 2G, H], *Dlx5*$^{-/-}$ [(Depew et al., 1999), Figure 6D, F, H; (Depew et al., 2005), Figure 19B], *Dlx6*$^{-/-}$ [(Jeong et al., 2008), Figure 6b], and corresponding *Dlx* allelic combinations [e.g. [*Dlx1*$^{-/-}$*;Dlx2*$^{-/-}$*;Dlx5*$^{-/-}$], (Depew et al., 2005), Figure 16B]. More complex ectopic elements (red arrowheads) are noted in DCM embryos, often containing ossified elements with apparent cartilaginous 'joints', a feature again observed in various *Dlx* compound mutants [e.g. *Dlx5*$^{-/-}$*;Dlx6*$^{+/-}$, (Depew et al., 2005), Figure 16C and [*Dlx1*$^{+/-}$*;Dlx2*$^{+/-}$*;Dlx5*$^{-/-}$*;Dlx6*$^{+/-}$] (Depew et al., 2005), Figure 20B]. Also, as briefly mentioned above, loss of the ZGA was often associated with the appearance of ectopic bone and cartilage elements on the lateral side-walls of the cranium, reminiscent of the 'palatoquadrate-like' element discussed in various *Dlx* mutants. Such elements were apparent in DCM embryos, and previously described in, for example, *Dlx2*$^{-/-}$ [(Qiu et al., 1995), 1995, Figure 4B, D], *Dlx1*$^{-/-}$*;Dlx2*$^{-/-}$ [(Qiu et al., 1997), Figure 3E, G], *Dlx2*$^{-/-}$*;Dlx5*$^{-/-}$ [(Depew et al., 2005), Figure 11G], and *Dlx1*$^{-/-}$*;Dlx2*$^{-/-}$*;Dlx5*$^{-/-}$ [(Depew et al.,

2005), Figure 16B] mutants – although variations are noted between genetic models. *Larger boxes indicate the complexity of *Dlx* allelic combinations that can generate variations of these ectopic processes. See references cited for individual details.

(**E**) **Additional BA1 and caudal BA derivatives**: Several other unique features were shared between AP-2 and *Dlx* mutants. In regard to more caudal BA derivatives, the hyoid was often found cleft in SCM-A embryos and fused with the thyroid cartilages. Such features were noted in *Dlx2*$^{-/-}$ [(Depew et al., 2005), Figure 9D], *Dlx1*$^{-/-}$*;Dlx2*$^{-/-}$ [(Depew et al., 2005), Figure 9H], various *Dlx2;Dlx5* compound [(Depew et al., 2005), Figure 11G, I, Figure 12J], *Dlx1*$^{-/-}$*;Dlx2*$^{-/-}$*; Dlx5*$^{-/-}$ [(Depew et al., 2005), Figure 16B], and *Dlx2*$^{-/-}$*Dlx6*$^{-/-}$ [(Jeong et al., 2008), Figure S6L] mutants. More strikingly, the hyoid was fused to the cranial base/pterygoids in DCM embryos. Again, this unusual phenotype was observed in various *Dlx* mutants, notably *Dlx5*$^{-/-}$*;Dlx6*$^{-/-}$ embryos [(Beverdam et al., 2002), Figure 2E]. Additional noted similarities include a variably affected styloid process in SCM-A and DCM embryos, as seen in *Dlx2*$^{-/-}$ [(Qiu et al., 1995), Figure 4B; (Depew et al., 2005), Figure 4E], *Dlx5* $^{-/-}$ [(Acampora et al., 1999), Figure 4B], and *Dlx5*$^{-/-}$*;Dlx6*$^{-/-}$ [(Depew et al., 2002), Figure 3D] mutants. Similarly, the tympanic and gonial bones were variably affected in SCM-A and absent in DCM embryos. Such a continuum was observed in *Dlx* mutants, including hypoplastic formation of these elements in *Dlx6*$^{-/-}$ mutants [(Jeong et al., 2008), Figure 5J], major hypoplasia in *Dlx1*$^{-/-}$*;Dlx6*$^{-/-}$, *Dlx2*$^{-/-}$*;Dlx6*$^{-/-}$ mutants [(Jeong et al., 2008), Figure 6c, d], and complete ablation in *Dlx2*$^{-/-}$*;Dlx5*$^{-/-}$ mutants [(Depew et al., 2005), Figure 11G].

(**F**) **Secondary palatal development**: Although not discussed in detail, several *Dlx* allelic combinations result in clefting of the secondary palate, due to defects in palatal processes of the palatine and maxillary bones – as well as altered pterygoids. Similarly, SCM-A, occasionally SCM-B, and DCM embryos develop overlapping palatal defects.

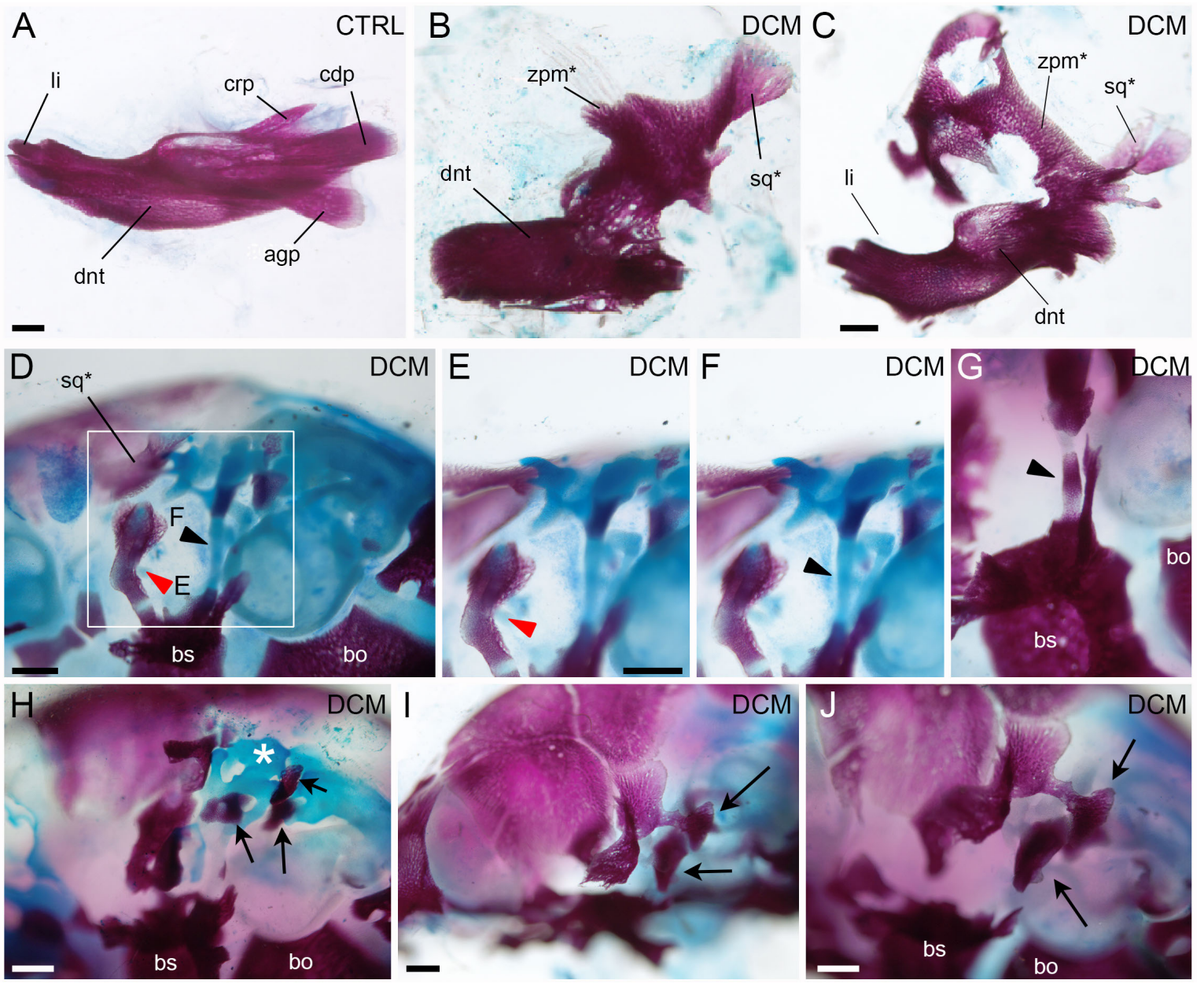

Figure S9 – Additional images of 'Dlx-like' skeletal defects observed in *Tfap2a/Tfap2b-Wnt1*:CRE (DCM) mutants. (**A-J**) Images of E18.5 skeletal preparations of the indicated genotype. (**A-C**) Lateral views (anterior left) of control (**A**) or DCM (**B-C**) mandibles in isolation. Note, the entire maxillary bone is also included in panel **C**, which is fused by its zygomatic process to a modified coronoid process. (**D-J**) Additional ventral views (anterior medial at bottom left) of BA1 hinge-region associated defects detected within the cranial walls and cranial base of DCMs. Various bones (maxillary, palatal, etc) have been removed for better visualization. (**D-G**) highlight ectopic struts (red arrowhead for rostral and black arrowheads for caudal). Panel D is from the same embryo shown in Fig. 6L and panel **E** and **F** are higher magnification images of the boxed area in panel D shot in different focal planes to highlight either the rostral or the caudal strut, respectively. (**H-J**) Show examples of abnormal bone (black arrows) and cartilage elements (white asterisk) with unclear relationship to the normal skeletal derivatives of the cranial base and cranial sidewalls. Comparable control images of the cranial base and side walls are presented in Figs 5 and 6. Abbreviations: agp, angular process; bo, basioccipital; bs, basisphenoid; cdp, condylar process; crp, coronoid process; dnt, dentary; li, lower incisor; sq*, transformed squamosal; zpm* transformed zygomatic process of the maxilla. Scale bars = 500μM.

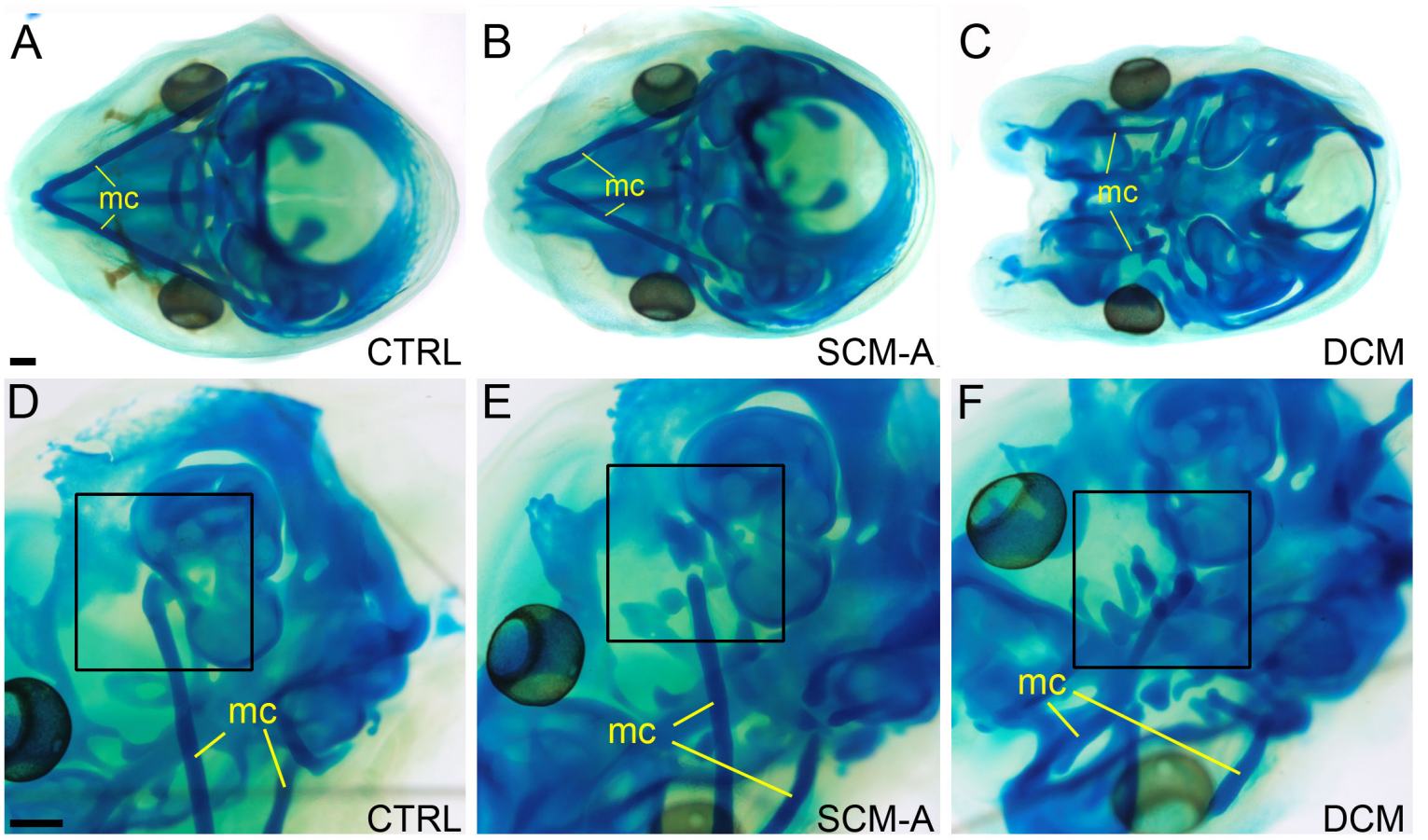

Figure S10 – Additional images of the chondrocranium in *Tfap2a/Tfap2b-Wnt1*:CRE (DCM) and *Tfap2a-Wnt1*:CRE (SCM-A) mutants. (**A-F**) E15.5 cartilage preparations of the indicated genotype shown in either ventral, anterior to the left (**A-C**), or ventrolateral, anterior to the bottom left (**D-F**), views. Boxed regions in D-F highlight the proximal end of Meckel's cartilage. Abbreviations: mc, Meckel's cartilage. Scale bars = 500µM.

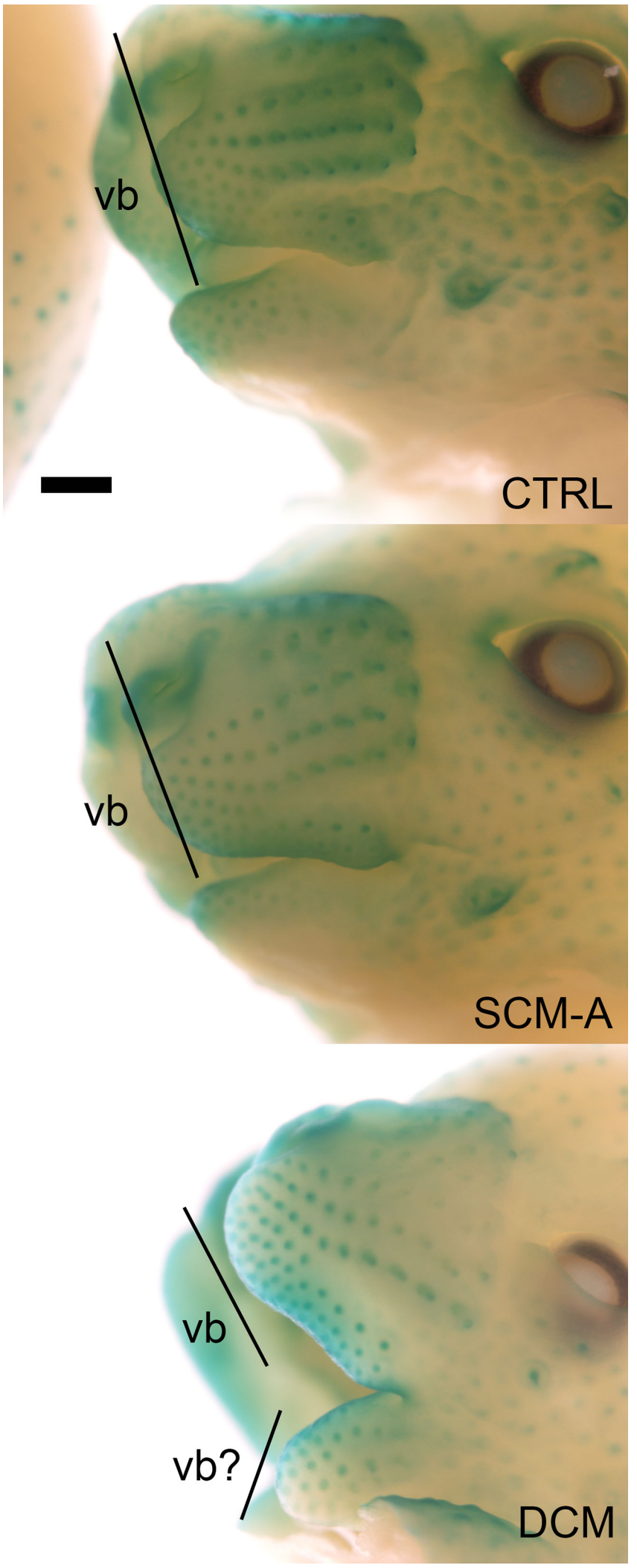
vb
CTRL
vb
SCM-A
vb
vb?
DCM

Figure S11 – Vibrissae-like structures in lower-jaw of *Tfap2a*/*Tfap2b*-*Wnt1*:CRE mutants.

(**A-C**) Lateral views of E14.5 embryos, of the indicated genotype, processed for ß-galactosidase staining. The staining is the result of a *Tfap2a LacZ* knock-in reporter allele (Brewer et al., 2002), highlighting endogenous *Tfap2a* expression – which includes the developing vibrissae (vb). Scale bar = 500µM.

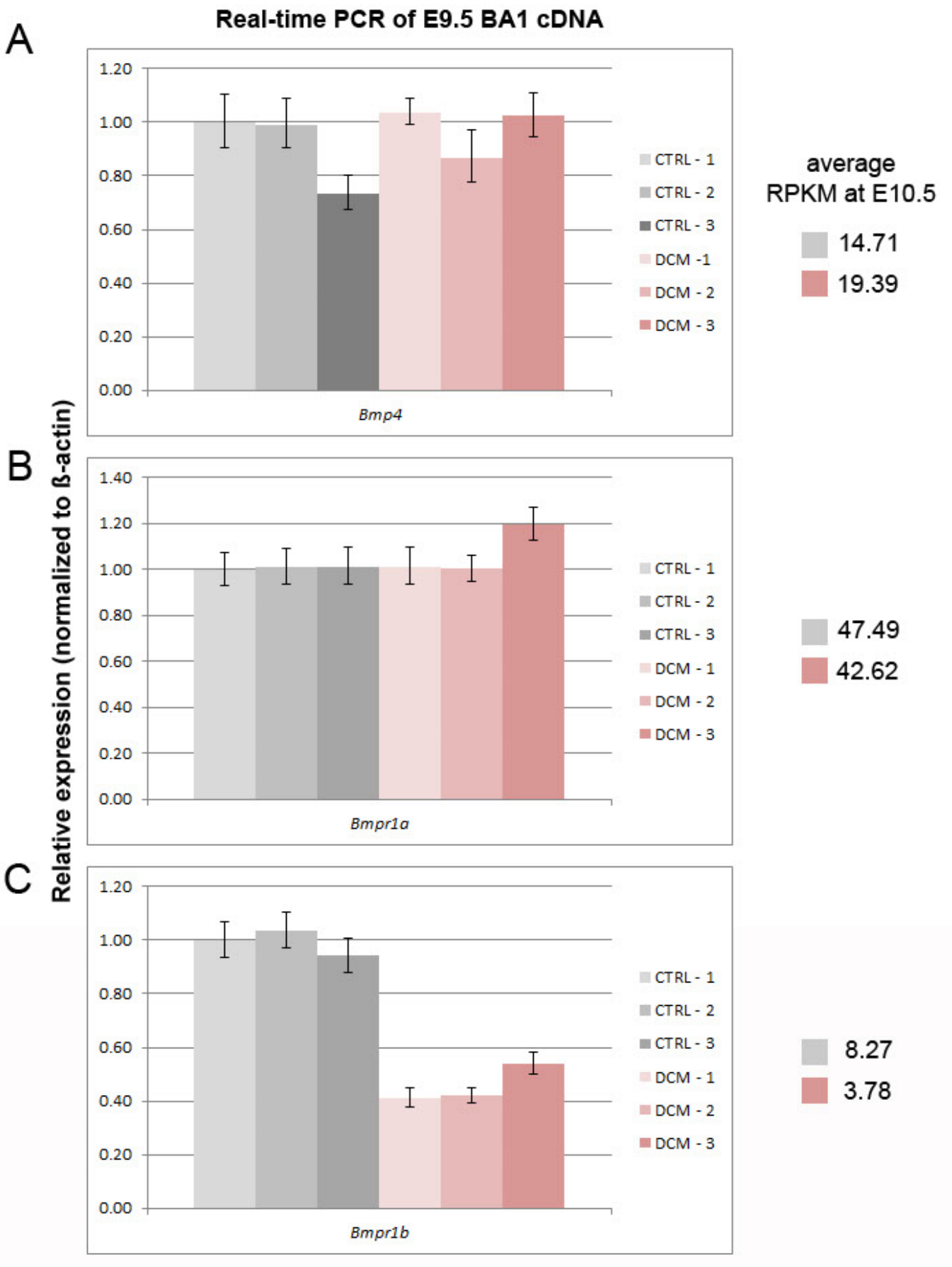

Figure S12. Real-time PCR analysis of BMP-pathway. (**A-C**) Charts summarizing real-time PCR quantification expression levels of *Bmp4* (**A**), *Bmpr1a* (**B**), and *Bmpr1b* (**C**) in E9.5 BA1 cDNA from CTRL and DCM embryos relative to *Actb* (ß-actin). Each bar represents a single embryo, with standard error of technical replicates reported. Values to the right of each chart report the average RPKM value for each gene, based on the E10.5 RNA-seq analysis.

Table S1 – Summary of phenotypes in various AP-2 allelic combinations

Table S1. Genotype and phenotype information for the neural crest *Tfap2a/Tfap2b* gene targeting studies

A. Genotypes derived from mating scheme

Genotype	Description	Abbreviation	CRE
Tfap2a$^{wt/flox}$ *Tfap2b*$^{wt/flox}$	control	ctrl	negative
Tfap2a$^{null/flox}$ *Tfap2b*$^{wt/flox}$	control	ctrl	negative
Tfap2a$^{wt/flox}$ *Tfap2b*$^{null/flox}$	control	ctrl	negative
Tfap2a$^{null/flox}$ *Tfap2b*$^{null/flox}$	control	ctrl	negative
Tfap2a$^{wt/flox}$ *Tfap2b*$^{wt/flox}$ *Wnt1*:CRE	Double conditional heterozygote	DCH	positive
Tfap2a$^{null/flox}$ *Tfap2b*$^{wt/flox}$ *Wnt1*:CRE[ǂ]	Single conditional mutant - *Tfap2a*	SCM-A	positive
Tfap2a$^{wt/flox}$ *Tfap2b*$^{null/flox}$ *Wnt1*:CRE[‡]	Single conditional mutant - *Tfap2b*	SCM-B	positive
Tfap2a$^{null/flox}$ *Tfap2b*$^{null/flox}$ *Wnt1*:CRE*	Double conditional mutant	DCM	positive

[ǂ] ~11% of SCM-A embryos (4 of 38 at E18.5) develop exencephaly, a phenotype that was also noted in ~15% of Tfap2a-Wnt1:CRE mice (Brewer S et al 2004)

[‡] ~22% of SCM-B embryos developed gross cleft secondary palate

* Number of DCM embryos recovered at E18.5, ~4% instead of expected 12.5%, 8 DCMs of 210 total embryos, in comparison to E10.5/E11.5, ~10.5%, 72 DCMs of 695 total embryos, indicates a proportion of embryos die in between these gestational ages. Also, ~50% of embryos (4 of 8 at E18.5) develop exencephaly - for subsequent analysis we concentrated on embryos that lacked exencephaly as this abnormality alone can directly impact craniofacial morphology (Green RM et al 2016)

B. Summary of select craniofacial defects in E18.5 single and double conditional mutant skeletons relative to controls

Genotype (abbreviation)	N	*palate*	*premaxillary*	*mandibular*	*hyoid*	*zygomatic arch*	*squamosal*	*ectopic strut*	*tympanic*
Controls (CTRL)	14	0% (0)	0% (0)	0% (0)	0% (0)	0% (0)	0% (0)	0% (0)	0% (0)
Tfap2a$^{null/flox}$;*Tfap2b*$^{wt/flox}$;*Wnt1CRE (SCM-A)*	18	100% (18)	22% (4)	72%[1] (13)	56%[2] (10)	100%[3] (18)	39%[4] (7)	100%[5] (18)	67%[8] (12)
Tfap2a$^{wt/flox}$;*Tfap2b*$^{null/flox}$;*Wnt1CRE (SCM-B)*	9	22% (2)	0% (0)	0% (0)	0% (0)	0% (0)	0% (0)	0% (0)	0% (0)
Tfap2a$^{null/flox}$;*Tfap2b*$^{null/flox}$;*Wnt1CRE (DCM)*	6	100% (6)	100% (6)	100%[1] (6)	100%[2] (6)	100%[3] (6)	100%[4] (6)	100%[5] (6)	100%[8] (6)

Summary of categories: **palate**, presence of cleft secondary palate; **premaxillary**, presence of midface cleft (split/cleft premaxillary bones, see Figure 5F); **mandibular**, defects found at proximal end of dentary bone (coronoid, condylar, or angular processes); **hyoid**, defects found in hyoid (hypoplastic, 'pinched', cleft); **zygomatic arch** (ZGA), any defects associated with ZGA, including truncated zygomatic processes, missing jugal, etc; **squamosal**, either ectopic foramina in bone and/or hypoplastic/ablated bone; **ectopic strut**, ectopic bony or cartilaginous elements (as described in text); **tympanic**, hypoplastic or missing tympanic bone.

Additional details on phenotypes: [1]Defects in SCM-A skeletons generally corresponded to hypoplastic mandibular processes (see Figure 5N), whereas in DCM skeletons these defects were associated with major loss of the proximal end of the manidble or fusion of lower-jaw to upper-jaw components (see Figure 5O, O'). [2]Defects in SCM-A embryos generally corresponded to small medial 'pinched' or occasional cleft hyoid, with no cranial base fusion (see Figure 6P, S), whereas DCM embryos always had a cleft hyoid found fused to the cranial base (see Figure 6U, X). [3]Defects in SCM-A embryos generally corresponded to shorter zygomatic processes of the maxilla and squamosal (see Figure 5H, K), whereas in DCM embryos these structures were generally ablated (see Figure 5I, L), or more severely truncated (see Figure 5I). [4]A portion of SCM-A skeletons displayed ectopic foramina in the squamosal (see Figure 6H), whereas this structure was either missing or severely malformed in DCM skeletons (see Figure 6I). [5]As described in the text, ectopic struts found in SCM-A and DCM embryos were not identical (compare Figure 6K, L). [8]The tympanic bone, including associated gonial bone, in SCM-A skeletons was hypoplastic (see Figure 6H, K), whereas the bone was completely missing in DCM skeletons (see Figure 6I, L, N).

Table S2 – Class I, Class II, and Class III gene-lists

Click here to Download Table S2

Table S3 – Curated list of genes used for gene set enrichment analysis

Click here to Download Table S3

Table S4 – Information relevant to genotyping primers

ALLELES	PRIMERS	ANNEALING TEMP	PCR PRODUCTS*
Tfap2a-KI (lacZ knock-in)	Alf6/7 (240) : a3KO (200) : iresup (120)	70°C	wt = 500, ki = 300
Tfap2a-null	Alf6/7 (200) : a3KO (240) : Neo3KO (120)	70°C	wt = 500, null = 265
Tfap2a-conditional	Aflox4 : Ascsq	65°C	wt = 496, conditional = 550
Tfap2b-null	Bfl1 : Revbeta6	70°C	wt = 210, conditional = 300‡
Tfap2b-conditional	Bfl1 : Bfl2	70°C	wt = 430, conditional = 550
Wnt1:CRE	Wnt1CRE-F : Wnt1CRE-R	70°C	transgene = ~450
Sox2:CRE	Cre 1 : Cre 3	68°C	transgene = 450
PRIMER SEQUENCES			
Alf6/7	5'-AGG-TGT-AGG-CAG-AAG-TTT-GTC-AGG-GC-3'		
a3KO	5'-CGT-GTG-GCT-GTT-GGG-GTT-GTT-GCT-GAG-GTA-C-3'		
iresup	5'-GCT-AGA-CTA-GTC-TAG-CTA-GAG-CGG-CCC-GGG-3'		
Neo3KO	5'-AAC-GCA-CGG-GTG-TTG-GGT-CGT-TTG-TTC-G-3'		
Aflox4	5'-CCC-AAA-GTG-CCT-GGG-CTG-AAT-TGA-C-3'		
Ascsq	5'-GAA-TCT-AGC-TTG-GAG-GCT-TAT-GTC-3'		
Bfl1	5'-GTC-TGT-TTA-GAA-CAG-CCA-GAG-GCT-GG-3'		
Revbeta6	5'-CCC-GAG-CTA-AGT-GAA-CAG-CTT-CCC-CTG-TAA-GGA-GAG-C-3'		
Bfl2	5'-TCT-GGC-AAG-GCT-CGC-ACT-CAC-AGC-AG-3'		
Wnt1CRE-F	5'-CTC-ATT-GTC-TGT-GGC-CCT-GAC-C-3'		
Wnt1CRE-R	5'-ACG-CCT-GGC-GAT-CCC-TGA-AC-3'		
Cre 1	5'-GCT-GGT-TAG-CAC-CGC-AGG-TGT-AGA-G-3'		
Cre 3	5'-CGC-CAT-CTT-CCA-GCA-GGC-GCA-CC-3'		

*numbers listed for PCR products corresponds to length in basepairs

‡Note, when genotyping *Tfap2b* -null allele, primers were used that did not recognize the deleted allele, but rather indicated if the WT-allele was present (along with generating a conditional-specific PCR product). Embryos in which no WT-allele was present identified those which recieved the paternally derived *Tfap2b* -null allele. This strategy was utilized to prevent false-positives as a result of recombination of the *Tfap2b* -conditional allele.

Numbers in red correspond to the final concentration of primers used, reported in nM. All other primers were used at final concentration of 200nM.

Table S5. Primer sequences

Target	Name	Sequence	Size (bp)	Size+intron*
Six1	Six1-qF	TTAAGAACCGGAGGCAAAGA	154	2191
	Six1-qR	GGGGGTGAGAACTCCTCTTC		
Rspo2	Rspo2-qF	CAGATGCGTTTTTGCCTCTT	158	76547
	Rspo2-qR	CAACCATTGTCCTTCGAACA		
Dlx1	Dlx1-qF	CTACGTCAACTCGGTCAGCA	173	823
	Dlx1-qR	TCTTTTTCCCTTTGCCGTTA		
Dlx2	Dlx2-qF	ATGTCTCCTACTCCGCCAAA	185	600
	Dlx2-qR	GGAGTAGATGGTGCGTGGTT		
Dlx3	Dlx3-qF	CGTTTCCAGAAAGCCCAGTA	168	1678
	Dlx3-qR	ACTGTTGTTGGGGCTGTGTT		
Dlx4	Dlx4-qF	CCATCTCAGCCCTTTCACAG	152	3368
	Dlx4-qR	TGGAGCTGCAGGCTAGAGTAG		
Dlx5	Dlx5-qF	CTGGCCGCTTTACAGAGAAG	220	1257
	Dlx5-qR	CTGGTGACTGTGGCGAGTTA		
Dlx6	Dlx6-qF	ACCATCGCTTTCAGCAGACT	227	1996
	Dlx6-qR	AGAAACGTCCCACACTGGAG		
Bmpr1a	Bmpr1a-qF	GATGATCAGGGAGAAACCACA	162	6526
	Bmpr1a-qR	AACAACAGGGGGCAGTGTAG		
Bmpr1b	Bmpr1b-qF	GCCCATCGAGACTTGAAAAG	176	11272
	Bmpr1b-qR	AAGCTCTCGTCCAGCACTTC		
Bmp4	Bmp4-qF	GGAACCGGGCTTGAGTACC	156	1158
	Bmp4-qR	CACCTCATTCTCTGGGATGC		

*Note, 'Size+intron' corresponds to the predicted genomic size amplified from the primer pair (in basepairs), if the intron is present (i.e., if genomic DNA were present). For all real-time PCR reactions, only the smaller PCR product (Size) was amplified, and absence of the larger product confirmed.